ULTRA-THIN ALUMINUM NITRIDE FILMS FOR FLEXIBLE MEMS SENSORS

by

MD SAJEEB RAYHAN

Presented to the Faculty of the Graduate School of

The University of Texas at Arlington in Partial Fulfillment

of the Requirements

for the Degree of

DOCTOR OF PHILOSOPHY

THE UNIVERSITY OF TEXAS AT ARLINGTON

August 2016

Copyright © by Md Sajeeb Rayhan 2016

All Rights Reserved

Acknowledgements

To begin with, I would like to thank my supervising Professor Donald P. Butler for his relentless support throughout the journey of my PhD. I feel immensely blessed and thankful to him for his patience, guidance and encouragement for the past few years which encouraged me to learn new things each day and taught me one valuable lesson that there is no shortcut in research. He taught me that there will be times when the results might not go in your favor but you have to keep trying your best until you succeed. His suggestions towards every aspect of my research helped me come thus far.

I would like to thank my dissertation committee member Professor Zeynep Celik-Butler for her insightful opinions and ideas she shared with us during our group meetings and outside the meetings. Her suggestions at many aspects have helped me a lot in improving the quality of my research work. I would like to thank my other committee members of my PhD dissertation, Professor Jing-Chih Chiao, Professor Samir Iqbal, Professor Dereje Agonafer, Professor Jonathan Bredow, and Professor Anand J. Puppala for their valuable time and effort in reviewing my research work and making insightful comments.

I would like to also thank Dr. Nader Hozhabri, D. Bueno, and R. Chambers during my work in the cleanroom and outside the cleanroom. I really appreciate their help and patience while working with me. I would like to give special thanks to Dr. M. Ahmed, Dr. I. Mahmud, Dr. Yi Li, Dr. M. Nour, Md S. Mahmood, Sk R. Tousif and my other fellow Nanofab colleagues and friends for their company, help, and useful discussions.

I am eternally grateful to my parents, my sisters, and my wife Afrin Fatema for their invaluable support and prayers. I will always remember their love and contribution in my life.

September 09, 2016

Abstract

ULTRA-THIN ALUMINUM NITRIDE FILMS FOR FLEXIBLE MEMS SENSORS

Md Sajeeb Rayhan, PhD

The University of Texas at Arlington, 2016

Supervising Professor: Donald P. Butler

Microelectromechanical systems (MEMS) sensors using ultrathin aluminum nitride (AlN) film were developed and fabricated using conventional photolithography techniques in the class 100 clean room with a view to integrate them in flexible substrates along with flexible electronics. The MEMS sensors were designed, analytically modeled, fabricated and characterized. Some of the MEMS sensors were only designed and simulated using finite element method (FEM) for the scope of the dissertation. These MEMS sensors can be applied to many applications such as automobile, robotics, biomedical, biometrics, health condition monitoring, GPS tracking devices, smartphones and aircrafts.

MEMS pressure sensors using AlN based piezoelectric film were designed, fabricated and characterized in the form of array of cantilever based structures. A 300 nm thick ultrathin and flexible AlN film with a feature size of ~12 μm which was deposited using DC reactive magnetron sputtering system and sandwiched between two electrodes to induce cantilever shaped structures acted as the sensing element of the cantilever sensors. After fabrication, several cantilevers were chosen for electrical characterization. The pressure sensors were characterized in a probe station system to measure the piezoelectric voltage signals and power spectral densities. With the help of simulation results, numerical modeling was also carried out to find the theoretical output voltage

ranges and sensitivity of the cantilevers. The simple and flexible cantilevers form the basis for future piezoelectric energy harvesters, pressure sensors, fingerprint sensors and accelerometers using ultrathin AlN film those can be integrated on a system-on-chip (SoC) circuit. Initially, the ultrathin AlN films were developed by changing the deposition temperature and Ar/N_2 gas flow ratio and characterized using SEM, XRD and EDX to analyze the quality of the film. Stress analyses were taken into consideration to check the mechanical strength and reliability of the pressure sensors. In addition, bending performance was also analyzed by calculating the radius of curvature (ROC) of the cantilevers. Finally, noise performance was also analyzed.

Ultra-thin AlN based novel flexible MEMS fingerprint sensors were designed using finite element method i.e., CoventorWare® with a view to improve the pixel resolution and, hence, the quality of scanned fingerprint image. Two different sized pixel dimensions were used for the design of three fingerprint sensors; they are: a) FPS725A b) FPS725B, and c) FPS1016. The pixel dimension for FPS725A and FPS725B was 35 µm by 35 µm. The pixel feature was equivalent to an imaging resolution of 725 dot-per-inch (dpi). The other sensor had a pixel size of 25 µm by 25 µm and was equivalent to an imaging resolution of 1016 dpi. In both type of sensors, 200 nm thick, ultrathin AlN film was used as the sensing element. The difference between FPS725A and FPS725B was the location of the sensing element. In FPS725A, AlN film was deposited on top of Al_2O_3 diaphragm while in FPS725B, AlN was located inside the diaphragm. The fabrications process flow will be discussed in details in the fingerprint sensor chapter. In brief, the fingerprint sensors were comprised of array of pixels and each pixel was made of a cavity like structure which was basically an aluminum oxide (Al_2O_3) based structure. Underneath the cavity like structure, there was an adjacent piezoelectric plate or film which was sandwiched between two metal electrodes. The total area of the sensors is

identical and considered to be 15 mm by 15 mm for practical use. Piezoelectric output voltage with respect to various applied finger pressure were calculated using the stress contour found from the simulation results. Finally, piezoelectric response for each sensor for different finger pressure was found from the slope of the piezoelectric voltage versus applied force plot. The average piezoelectric responses are found to be 225.74 V/N, 115.58 V/N, and 125.52 V/N for FPS725A, FPS725B, and FPS1016, respectively. Stress analysis and noise performance of the sensors were studied. For practical use, the CMOS readouts will be taken from the Silicon substrate through the electrical metallization of pure metal electrodes which will be covered in the chapter.

An AlN based piezoelectric z-axis MEMS accelerometer was designed and simulated using CoventorWare®. Modal harmonic analysis was carried out and the simulated resonant frequency was found to be 2.26 kHz. Various loads were applied on top proof mass of the accelerometer ranging from 1g to 10g. Piezoelectric output voltages due to applied loads were calculated. The voltages ranged from 0.00082 V to 0.000082 V. The piezoelectric response or sensitivity was also calculated and found to be 0.000082 V/N. Noise performances was also analyzed and noise equivalent acceleration (NEA) was calculated. Noise equivalent acceleration was found to be 0.253 g/√Hz.

Table of Contents

Acknowledgements iii

Abstract iv

List of Illustrations xii

List of Tables xix

List of Symbols xxi

Chapter 1 1

Introduction 1

1.1 Brief overview of MEMS technology 1

1.2 Importance of piezoelectric materials in MEMS applications 2

1.3 Major applications of piezoelectric MEMS sensors 4

1.3.1 Automobile industry 4

1.3.2 Biometrics 5

1.4 Piezoelectric materials: State of the art 6

1.5 AlN as a promising piezoelectric material in flexible MEMS sensors: state of the art 7

1.6 Contribution made by this dissertation work 9

1.7 Dissertation outline 10

1.8 Summary 13

Chapter 2 14

Theory 14

2.1 Piezoelectric effects 14

Chapter 3 19

Ultra-thin AlN based cantilevers for flexible MEMS sensors 19

3.1 Introduction 19

3.1.1 Background and Motivation 20
3.2 Development of AlN Thin Films 22
3.3 Fabrication 24
3.3.1 Patterning of the photoresist 25
3.3.2. Deposition of Titanium film (bottom electrode) 26
3.3.3. Deposition of AlN film 27
3.3.4. Deposition of Titanium film (Top electrode) 28
3.3.5. Lift Off 28
3.3.6. Ashing 29
3.4 Characterization 30
3.4.2 Characterization Results 33
3.5 Design, Simulation and Modeling 38
3.5.1 Process editor 38
3.5.2. 2D Layout design 38
3.5.3 3D Solid model 38
3.5.4. Meshing and Mechanical Analysis 39
3.5.5. Numerical Modeling 44
3.6 Flexibility and Stress Analysis of the Cantilever 48
3.6.1 Stress analysis of the cantilever 48
3.6.2 AlN as a flexible material 49
3.7 Conclusions 53
3.7.1 Discussions 53
3.7.2 Future work 54
Chapter 4 55
High Resolution AlN based Fingerprint Sensors 55

4.1 Introduction 55
4.1.1 Background and motivation 56
4.2 Design and Simulation 59
4.2.1 725 dpi fingerprint sensor (FPS725A) 59
Process editor 61
2D layout 61
Design process flow 61
Mesh Convergence 62
4.2.2 725 dpi fingerprint sensor (FPS725B) 64
Process editor 65
2D layout 65
Design process flow 66
Mesh Convergence 68
4.2.3 1016 dpi fingerprint sensor (FPS1016) 68
Process editor 68
2D layout 69
Design process flow 69
Mesh Convergence 70
4.3 Results and discussion 70
4.3.1 725 dpi fingerprint sensor (FPS725A) 70
Stress analysis 70
Spring constant 71
Piezoelectric Voltage Response 72
4.4.2 725 dpi fingerprint sensor (FPS725B) 74
Stress analysis 74

Spring constant 75
Piezoelectric Voltage Response 76
4.4.3 1016 dpi fingerprint sensor (FPS1016) 77
Stress analysis 77
Spring constant 77
Piezoelectric Voltage Response 78
4.4 Noise Analysis 80
4.4.1 725 dpi fingerprint sensor (FPS725A) 80
4.4.2 725 dpi fingerprint sensor (FPS725B) 80
Johnson noise 80
Thermo-mechanical noise 82
Loss-tangent/tanδ noise 83
Total noise current 85
4.4.3 1016 dpi fingerprint sensor (FPS1016) 86
Johnson noise 86
Thermo-mechanical noise 87
Loss-tangent/tanδ noise 87
Total noise current 88
4.5 Figures of Merit 89
4.5.1 725 dpi fingerprint sensor (FPS725B) 89
4.5.2 1016 dpi fingerprint sensor (FPS1016) 90
4.5 Conclusions 91
Chapter 5 95
AlN based Piezoelectric MEMS Accelerometer 95
5.1 Introduction 95

5.1.1 Basic concepts 96

5.1.2 Ideal criteria a single/multiaxial (1D to 3D) accelerometer 98

5.1.3 Primary specification parameters for commercially available sensors 98

5.1.4 Piezoelectric accelerometers 99

5.1.5 Background 99

5.2 Design and Simulation 104

5.2.1 Process editor 108

5.2.2 2D layout 108

5.2.3 The Design process flow in 3D solid model 110

5.2.4 Mesh Convergence 112

5.3 Simulation and modeling Results 112

5.3.1 Modal Harmonic Analysis 112

5.3.2 Stress analysis 114

5.3.4 Piezoelectric Response 115

5.4 Noise Analysis 117

5.4.1 Johnson noise 117

5.4.2 Thermo-mechanical noise 118

5.4.3 Loss tangent or tanδ noise 122

5.4.4 Total noise current 124

5.5 Conclusions 125

Chapter 6 128

Conclusions 128

References 132

Biographical Information 145

List of Illustrations

Figure 1.1 MEMS as a microsensor [1] (Reproduced with permission. Copyright © McGraw-Hill) 1

Figure 3.1 X-ray diffraction θ/2θ patterns of AlN thin film (X-ray intensity vs. 2θ) showing the c-axis orientation (002) of the AlN film at an angle of 36.04º........ 24

Figure 3.2 SEM image of the surface morphology of AlN thin film showing the smoothness and good uniformity of the film. 24

Figure 3.3 The confocal image after the pattern of photoresist. The straight mesa structure shows the polyimide layer (after cure). 25

Figure 3.4 SEM image of a fabricated cantilever sensor (Bond pad is not shown). Measured dimensions: length=60 μm, width=12.7 μm, total thickness = 0.7 μm [45] (Reprinted with permission. M. S. Rayhan, D. P. Butler, and Z. Çelik-Butler, "Ultra-thin Film Piezoelectric AlN Cantilevers for Flexible MEMS Sensors," in Proc. 2015 IEEE Sensors Conf., Busan, Korea, Nov 1-4, 2015 © 2015 IEEE) 30

Figure 3.5 Fabrication steps for tri-layer cantilever. (a) Deposition of passivation layer, (b) deposition of contact layer, (c) photolithography of polyimide layer, (d) spin coating of LOR and NR7 1500 PY photoresist (e) patterning of the photoresists, (f) deposition of Ti, (g) deposition of AlN at 300 ^{0}C, (h) deposition of Ti, (i) liftoff of the tri-layer (Ti/AlN/Ti), (j) plasma ashing to remove the polyimide (sacrificial) layer [45] (Reprinted with permission. M. S. Rayhan, D. P. Butler, and Z. Çelik-Butler, "Ultra-thin Film Piezoelectric AlN Cantilevers for Flexible MEMS Sensors," in Proc. 2015 IEEE Sensors Conf., Busan, Korea, Nov 1-4, 2015 © 2015 IEEE)........ 31

Figure 3.6 Block diagram of the set-up for the characterization of AlN cantilevers. [45] (Reprinted with permission. M. S. Rayhan, D. P. Butler, and Z. Çelik-Butler, "Ultra-thin

Film Piezoelectric AlN Cantilevers for Flexible MEMS Sensors", 2015 IEEE Sensors Conf., Busan, Korea, Nov 1-4, 2015 © 2015 IEEE) 32

Figure 3.7 Characterization set-up: (a) physical set up for the characterization (b) a wafer containing cantilevers is under test along with a nanopositioner, load cell and three probes in a micromanipulator probe station. Two probes are used to receive electrical signal from bondpads. Another vertical probe provides the force on the cantilever in the z-direction [45] (Reprinted with permission. M. S. Rayhan, D. P. Butler, and Z. Çelik-Butler, "Ultra-thin Film Piezoelectric AlN Cantilevers for Flexible MEMS Sensors," in Proc. 2015 IEEE Sensors Conf., Busan, Korea, Nov 1-4, 2015 © 2015 IEEE) 33

Figure 3.8 Close-up view of a cantilever that is under stress in the z-direction................ 33

Figure 3.9 Measured gain corrected response of the *Sensor A* operating at a 2.5 Hz loading frequency. [45] (Reprinted with permission. M. S. Rayhan, D. P. Butler, and Z. Çelik-Butler, "Ultra-thin Film Piezoelectric AlN Cantilevers for Flexible MEMS Sensors," in Proc. 2015 IEEE Sensors Conf., Busan, Korea, Nov 1-4, 2015 © 2015 IEEE)................ 35

Figure 3.10 Gain corrected power spectral density of the signal from Figure 3.9 showing the Johnson noise floor. [45] (Reprinted with permission. M. S. Rayhan, D. P. Butler, and Z. Çelik-Butler, "Ultra-thin Film Piezoelectric AlN Cantilevers for Flexible MEMS Sensors," in Proc. 2015 IEEE Sensors Conf., Busan, Korea, Nov 1-4, 2015 © 2015 IEEE)............ 35

Figure 3.11 Measured gain corrected response of the *Sensor B* operating at a 3 Hz loading frequency. 36

Figure 3.12 Gain corrected power spectral density of the signal from Figure 3.11 showing the Johnson noise floor. 36

Figure 3.13 Measured gain corrected response of the *Sensor C* operating at a 3.5 Hz loading frequency. 37

Figure 3.14 Gain corrected power spectral density of the signal from Figure 3.13 showing the Johnson noise floor. 37

Figure 3.15 Step name and thickness of different layers are shown in the process editor. 38

Figure 3.16 2D Layout of the cantilever including bond pad. 39

Figure 3.17 Physical Properties of AlN film mentioned in *material editor.* 40

Figure 3.18 Piezoelectric coefficient matrix and dielectric constants. 40

Figure 3.19 The exaggerated view (in z-direction) of the cantilever with proper labeling. 41

Figure 3.20 Mesher settings 41

Figure 3.21 Meshed model of the cantilever 42

Figure 3.22 (a) and (b) Boundary conditions set up 43

Figure 3.23 CoventorWare® Visualizer results showing (a) displacement (b) Mises stress after mechanical analysis (here, applied load is 0.01 MPa in z direction). 43

Figure 3.24 Circuit model of the AlN cantilevers including external loading. 45

Figure 3.25 Equivalent circuit model for the piezoelectric cantilever. 45

Figure 3.26 Region of the cantilever under consideration for charge calculation due to piezoelectricity. 47

Figure 3.27 Piezoelectric responses from simulation and numerical modeling at different loading frequency (Piezoelectric voltage versus applied force). 48

Figure 3.28 The simulated tensile stresses of the cantilever with respect to different applied load (AlN film thickness=300 nm). 49

Figure 3.29 Simulated stress analyses for Titanium (Ti) films as top and bottom electrodes with respect to various thicknesses of AlN film while keeping the cantilever maximum displacement fixed to 2.23 μm. 51

Figure 3.30 Simulated tensile stress analyses for AlN film with respect to change its thickness while keeping the cantilever maximum displacement fixed to 2.23 µm. 51
Figure 3.31 Simulated compressive stress analysis for AlN film with respect to change its thickness while keeping the cantilever maximum displacement fixed to 2.23 µm. 52
Figure 4.1 Process Editor 61
Figure 4.2 2D layout 61
Figure 4.3 Process flow of the pixel design in preprocessor (a) Si Substrate (b) deposition and pattern of passivation (Si_3N_4) layer (c) deposition and pattern of polyimide layer (d), (e), and (f) deposition and trilayer liftoff of bottom electrode (Ti), piezoelectric (AlN) layer , and top electrode (Ti). 61
Figure 4.4 3D solid meshed model of a pixel of the sensor. Dimension of Al_2O_3 membrane: 35 µm×35 µm; AlN and Ti: 26 µm×26 µm. 62
Figure 4.5 Dimension of the hole is shown. Holes are used to remove the sacrificial layer (i.e., polyimide) and form a cavity like structure. 62
Figure 4.6 Labeled layers of a pixel (partial). 62
Figure 4.7 Simulated maximum Mises stress of Al_2O_3 film with respect to different planer mesh size of Al_2O_3 membrane layer (Mesh convergence study). 63
Figure 4.8 Simulated maximum Mises stress of AlN film with respect to different planer mesh size of Al_2O_3 membrane layer (Mesh convergence study). 64
Figure 4.9 Process Editor 65
Figure 4.10 2D layout including the dimension. Dimension of Al_2O_3 based membrane: 35 µm×35 µm; AlN and Ti: 25 µm×25 µm. 65
Figure 4.11 3D Process flow of the 35 µm×35 µm pixel design in preprocessor (FPS725B) (a) Silicon substrate layer (b) deposition of passivation (Si_3N_4) layer (c) etching of hole in the passivation layer for contact pad (d) lift off of contact pad (e)

deposition and pattern of polyimide layer (f) 1st level of metallization for bottom electrical connection using lift off technique (g) trilayer deposition Ti/AlN/Ti stack and simultaneous lift off pattern (h) deposition of an insulation layer to provide side wall insulation to prevent electrical short between top and bottom electrode (i) etching a window on the insulation layer for electrical connect (j) 2nd level of metallization for top electrical connection (k) deposition of Al_2O_3 all over the area to form the cavity structure (membrane+side walls) (l) top surface planarization and pattern of Al_2O_3 cavity structure including the etching hole to remove the sacrificial polyimide layer. 66

Figure 4.12 (a) top view of the final structure of the pixel (b) bottom view of the final structure of the pixel (c) meshed model of the pixel. 67

Figure 4.13 2D layout including the dimension. Dimension of Al_2O_3 membrane: 25 μm×25 μm; AlN and Ti: 15 μm×15 μm. 69

Figure 4.14 Design of 25 μm×25 μm pixel in preprocessor (FPS1016) (a) top view of the final structure of the pixel (b) bottom view of the final structure of the pixel (c) meshed model of the pixel. 69

Figure 4.15 (a) Displacement contour of a pixel and (b) Mises stress contour in the piezoelectric AlN layer from CoventorWare® simulation. 70

Figure 4.16 Simulation plot of maximum Mises stress of each layer with respect to different loads. 72

Figure 4.17 Simulation plot of spring Constant of the pixel of FPS725A. 72

Figure 4.18 Simulation plot of piezoelectric output voltage of the sensor with respect to different loads mentioned in Table 4.5. 73

Figure 4.19 (a) Simulated displacement contour of a pixel and (b) simulated Mises stress contour of the pixel (bottom view) (c) Mises stress of AlN film from simulation. 74

Figure 4.20 Simulation plot of maximum Mises stress of each layer with respect to different loads. 75

Figure 4.21 Simulation plot of spring Constant of FPS725B 75

Figure 4.22 Simulation plot of piezoelectric output voltage of the sensor with respect to different loads mentioned in Table 4.7 76

Figure 4.23 (a) Simulated displacement contour of a pixel and (b) simulated Mises stress contour of the pixel (bottom view) (c) Mises stress of AlN film. 77

Figure 4.24 Simulation plot of maximum Mises stress of each layer with respect to different loads. 78

Figure 4.25 Simulation spring Constant of the pixel of FPS1016. 78

Figure 4.26 Simulation plot of piezoelectric output voltage of the sensor with respect to different loads mentioned in Table 4.9. 79

Figure 4.27 The equivalent electrical circuit 80

Figure 4.28 Johnson noise current plot from calculation. 81

Figure 4.29 circular displacement contour of the square diaphragm. 82

Figure 4.30 tanδ noise spectra from calculated data. 84

Figure 4.31 Plot from calculated data for total noise current of the pixel of FPS725B 85

Figure 4.32 Johnson noise current spectra from calculated data 86

Figure 4.33 tanδ noise spectra from calculated data 87

Figure 4.34 total noise current spectra from calculated data for the pixel of FPS1016 88

Figure 5.1 Mass-spring-damper system. 96

Figure 5.1 Process Editor 108

Figure 5.2 2D layout (a) full view, (b), (c) and (d) partial view 109

Figure 5.6 (a) zoomed view of an anchor and adjacent layers and (b) Meshed model (partial view). 112

Figure 5.7 Modal harmonic analysis 113

Figure 5.8 Modal frequencies versus displacements from modal harmonic analysis. ... 114

Figure 5.9 Simulated plot of von Mises stress versus acceleration for different materials.
.... 115

Figure 5.10 Visualizer stress contour from CoventorWare®. 116

Figure 5.11 Piezoelectric voltages versus acceleration plot from simulation and modeling.
.... 117

Figure 5.12 Johnson noise current spectra from calculated data 118

Figure 5.13 tanδ noise current spectra of the accelerometer from calculated data 123

Figure 5.14 Total noise current and individual noise currents from calculated data 124

List of Tables

Table 1.1 lists the typical piezoelectric properties of AlN, ZnO and PZT thin films [7]. 8

Table 3.1 Development of the recipe for the deposition of AlN 23

Table 3.2 EDX analysis showing the stoichiometry between Al and N in the AlN film. 23

Table 3.3: spin coating 25

Table 3.4 Deposition parameters of the bottom electrode 26

Table 3.5 Sputtering conditions for the deposition of the AlN thin films 28

Table 3.6 Deposition parameters of the top electrode 28

Table 3.7 Parameters used during the ashing process 29

Table 3.8 Characterization results of the AlN based cantilevers at various frequencies .. 34

Table 3.9 Mask layers dimensions 39

Table 3.10 Simulation and numerical analysis results with applied load 47

Table 3.11 Simulated stress analysis varying AlN film thickness 52

Table 4.1 Mesh conditions for different layers in CoventorWare® 64

Table 4.2 Mesh for different layers 68

Table 4.3 Mesh for different layers 70

Table 4.4 Simulated stress analysis of the sensor (FPS725A) 71

Table 4.5 Simulation and numerical modeling results for piezoelectric Response of the sensor (FPS725A) 73

Table 4.6 Simulated stress analysis of the sensor (FPS725B) 74

Table 4.7 Simulation and modeling results for piezoelectric Response of the 725 dpi (FPS725B) sensor 76

Table 4.8 Simulated stress analysis of the 1016 dpi fingerprint sensor (FPS1016) 77

Table 4.9 Simulation and modeling results of piezoelectric Response of the sensor (FPS1016) 79

Table 4.10 Parameters for calculation of Johnson noise spectra (FPS725B) 81

Table 4.11 Parameters involving the thermo-mechanical noise applying theoretical results for FPS725B (assuming, T=300 K) 83

Table 4.12 parameters and calculation of loss tangent noise for FPS725B (Assuming T=300 K) 84

Table 4.13 Parameters for calculation of Johnson noise spectra (FPS1016) 86

Table 4.14 Parameters involving the thermo-mechanical noise applying theoretical results for FPS1016 (assuming, T=300 K) 87

Table 4.15 parameters and calculation of loss tangent noise for FPS1016 (Assuming T=300 K) 88

Table 4.16 Calculated data of figures of merit for FPS725B 89

Table 4.17 Calculated data of figures of merit for FPS1016 90

Table 5.1 Summary of previous works on piezoelectric MEMS accelerometers 105

Table 5.2 Accelerometers design parameters and their symbols 108

Table 5.3 Parameters for different layers of the accelerometer for mesh convergence . 112

Table 5.4 Modal frequencies from simulation 113

Table 5.5 Simulated stress analysis of the sensor 115

Table 5.6 Calculation of piezoelectric Response of the accelerometer 116

Table 5.7 Calculated parameters for Johnson noise spectra 117

Table 5.8 Calculated results for thermomechanical noise current (assuming ξ=0.707 and T=300 K) 121

Table 5.9 Calculated results of thermo-mechanical noise current (assuming, T=300 K) 122

Table 5.10 parameters and calculation of loss tangent noise current (Assuming T=300 K) 123

List of Symbols

D	C/m^2	Electric flux density
σ	Pa	Normal stress
ε_0	F/m	Permittivity of free space
ε		Relative permittivity
k_B	$m^2\ kg\ s^{-2}\ K^{-1}$	Boltzmann's constant
T	K	Absolute Room temperature
E	V/m	Electric field
f	Hz	Frequency
V	V	Voltage
S		Strain
s	m^2/N	Elastic compliance
d	C/N	Piezoelectric charge constant
e	C/m^2	Stain piezoelectric coefficient
D_3	C/m^2	Electric flux density in (0002) direction
Q_T	C	Total charge
V_{JN}	V	Johnson Noise voltage
C_C	F	Capacitance of cantilever
C_B	F	Capacitance of bondpad
C_A	F	Capacitance of preamplifier
R_C	Ω	Resistance of cantilever
R_B	Ω	Resistance of bond pad
R_A	Ω	Resistance of preamplifier
A_{AlN}	m^2	Area of AlN sensing film

C	F	Capacitance of AlN film
S_{Jv}	V^2/Hz	Johnson noise floor or Johnson voltage power spectral density
ρ	Ω-m	Resistivity
L	M	Length of an resistor
A	m^2	Cross sectional area of an resistor
R	Ω	Resistance of AlN film
R_v	V/N	Piezoelectric voltage response
τ	S	Time constant of parallel RC circuit
i_{JN}	A/√Hz	Johnson noise current
P	Pa/√Hz	Thermal rms noise pressure
t	M	Thickness of Al_2O_3 based diaphragm
r	M	Radius of the approximated circular diaphragm
S_P	V/Pa	Pressure sensitivity
i_{TMN}	A/√Hz	Thermomechanical noise current
D_{air}	N.s/m	Damping coefficient of air damping force
F_d	N	Damping force
v_{TMN}	V/√Hz	Thermomechanical noise equivalent voltage
Q		Mechanical quality factor
f_0	Hz	Resonant frequency
ω_0	Rad/s	Circular resonant frequency
$tan\delta$		Dielectric loss tangent or dissipation factor
$i_{tan\delta}$	A/√Hz	Noise equivalent current due to loss tangent
X_c	Ω	Capacitive reactance
R_{ac}	Ω	AC resistance due to loss tangent

F_{tm}	N/√Hz	Thermomechanical force
b	Nsm^{-1}	Damping coefficient of a mass-spring-damper system
i_n	A/√Hz	Total noise equivalent current
m	Kg	Mass of proof mass
k	N/m	Spring constant of the accelerometer spring
a_{pm}	m/s^{-2}	Acceleration of proof mass
ξ		Damping ratio
σ_v	Pa	Von Mises stress
L_P	M	Length of proof mass of accelerometer
W_P	M	Width of proof mass of accelerometer
L_s	m	Length of spring of the accelerometer
W_s	M	Width of spring of the accelerometer
L_{piezo}	M	Length of piezoelectric layer of the accelerometer
W_{piezo}	M	Width of piezoelectric layer of the accelerometer
L_{top}	M	Length of top electrode of the accelerometer
L_{cp}	m	Length of contact pad of the accelerometer
L_o	m	Length of small square opening
L_{bot}	m	Length of bottom electrode of the accelerometer
W_{top}	M	Width of top electrode of the accelerometer
W_{cp}	M	Width of contact pad of the accelerometer
W_o	M	Width of small square opening of the accelerometer
W_{bot}	M	Width of bottom electrode of the accelerometer
A	G	Applied acceleration
g	ms^{-2}	Acceleration

S_a	V/g	Sensitivity of the accelerometer
a	ms^{-2}	Input acceleration
h_0	M	Thickness of air gap
P_a	Pa	Ambient pressure
μ	Kg/ms	Coefficient of viscosity
a_n	g/√Hz	Minimum detection level
Δf	Hz	Bandwidth of the accelerometer
D_{sfd}	N.s/m	Damping coefficient of damping force due to squeeze film damping
μ_{eff}	Kg/ms	Effective gas viscosity
l_{eff}	M	Effective length of the membrane
w_{eff}	M	Effective width of the membrane
$\beta\left(\frac{w_{eff}}{l_{eff}}\right)$		A function of l_{eff} and w_{eff}
K_n		Knudsen number
ω_c	Rad/s	Angular cutoff frequency
NEF	N/√Hz	Noise equivalent force of cantilever
NEP	Pa/√Hz	Noise equivalent pressure of fingerprint sensor
NEA	g/√Hz	Noise equivalent acceleration of the accelerometer
v_{so}	V	Piezoelectric output voltage of the cantilever sensor
R_F	V/N	Piezoelectric voltage response due to applied force
R_P	V/Pa	Piezoelectric voltage response due to applied pressure

Chapter 1

Introduction

1.1 Brief overview of MEMS technology

Over the past couple of decades, microsystem engineering has paved the way for ultramodern technology and opened the door for new field of technology in front of us which is known as microelectromechanical system or MEMS. Similar to Si IC technology, MEMS techniques can be seen as a modified IC technology which requires design, manufacture, and packaging in Si chip along with monolithic integration of microelectronics on the same chip. Applications of MEMS products range from aerospace to automotive, biotechnology, consumer products, defense, environmental protection and safety, healthcare, and telecommunications which means MEMS technology occupies billion dollars markets in real world and the market is ever growing with the introduction of new applications.

MEMS technology is fundamentally a transduction system which converts a mechanical entity to an electrical entity and vice versa. It relies up on two principle components, a) a sensing element or actuating element and b) a signal transduction unit. The following figure shows a block diagram of how a MEMS works as a sensor.

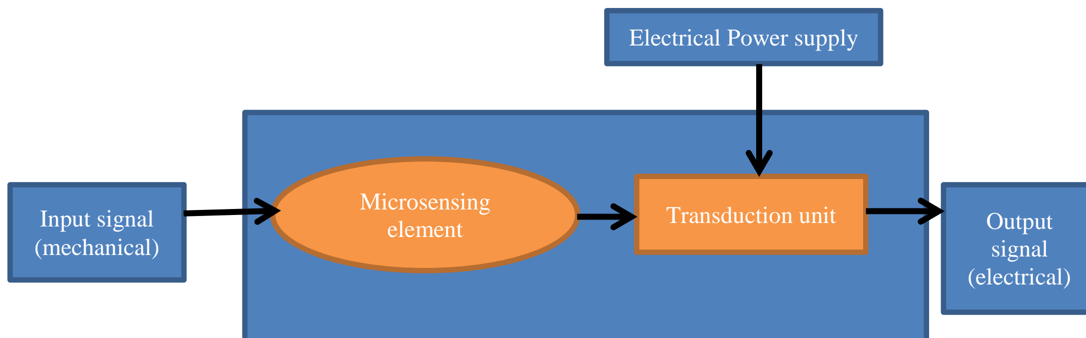

Figure 1.1 MEMS as a microsensor [1] (Reproduced with permission. Copyright © McGraw-Hill)

In this chapter, the discussion will focus solely on microsensors and their applications.

1.2 Importance of piezoelectric materials in MEMS applications

Though the microelectronics is an old technology compared to MEMS, however, the growth of MEMS technology would not have been possible without the thorough and well establishment of microelectronics technology. Well, if there are obvious similarities between these two technologies, there are also significant dissimilarities as well between them, for example, designing and packaging system of MEMS is different than that of microelectronics and IC technology. Materials engineering plays a great role in MEMS to develop new devices or fulfill specific requirements which is a big advantage of MEMS technology.

For the past couple of decades, numerous advancements have been made in micromachined sensors and actuators. As the domain of micromechanical systems (MEMS) advanced an urge for integration of materials apart from silicon and silicon based compounds into micromachined devices has appeared. Hence, to fulfill the need, piezoelectric materials have emerged into the field of micromachined transducers with more possibilities and interest than ever. Piezoelectric materials or films are of high density materials and can be scaled upon miniaturization according to the specification. The scaling feature has brought tremendous interest in these films and their use in various MEMS applications.

- Why piezoelectric materials are important in MEMS applications?

There are various reasons for which piezoelectric materials have become so popular in MEMS sensors applications.

1. Direct transduction mechanism

Piezoelectric materials unlike other materials such as capacitive, magnetic, piezoresistive provide direct transduction mechanism between mechanical to electrical domains and vice versa which gives them upper hand over other mechanisms, especially, in energy harvesting and sensor related application. Due to applied stress (strain), piezoelectric materials produce charge (voltage) by using their inherent property which is known as ‘piezoelectric effect’. The piezoelectric effect is linear and perfectly reversible which enables piezoelectric films or materials to get rid of hysteresis loss.

2. Pull-in effect

While capacitance based sensor applications require external voltage for biasing, piezoelectric material does not. This is a great advantage for sensor applications over other mechanism since it external requires extra space which means more cost towards manufacturing. Also, there is pull in effect for piezoelectric based unlike silicon based sensor applications where biasing is a must.

3. Miniaturization of piezoelectric films based sensors

One of the major features of MEMS sensors is miniaturization of sensing elements as well as the devices. The device sizes can be of from millimeter to nanometer range. Miniaturization is successfully implemented when the characteristics of the original version can be retained in the reduced version. The essence of miniaturization has become important more than ever since microsystems have become more complex and sophisticated where all the system including microelectronics can be integrated on a single chip. The benefits are described briefly as follows:

a) Microsystems are likely to move more quickly than larger counterparts because they will have lower inertia of mass

b) Smaller sized devices tend to experience lesser problems in distortion and vibration than large systems because smaller systems with lower masses have higher natural frequencies than larger equipment.

c) The tiny size of MEMS devices make them viable for applications in medicine and surgery which is impossible to achieve without miniaturization.

d) Another great importance of miniaturization is the application of MEMS devices in satellites and spacecraft engineering to meet the features like high precision and payload size.

As of scaling of MEMS devices, there is no standard laws like Moore's law, however, it is understood that the miniaturization is very important in manufacturing of MEMS devices to minimize the overall cost, reduce the device size and weight as long as the electromechanical coupling is remained consistent and the material properties are unchanged or improved

4. Flexibility in sensor applications

Bulk-materials do not provide flexibility in flexible sensors applications while thin film piezoelectric materials such as AlN provides flexibility upon pressure/force in cantilever or diaphragm based piezoelectric sensors which in turn provides bending to the films. Bending causes stress in the film which causes the piezoelectric materials to produce charge (voltage) due to piezoelectric effect. AlN is a viable solution to other piezoelectric materials in flexible sensors applications.

1.3 Major applications of piezoelectric MEMS sensors

1.3.1 Automobile industry

As the miniaturization of MEMS device continues, they have become increasingly popular in commercial markets. One of the major markets of MEMS devices is automobiles. Over the past two decades, MEMS technology has been vastly

implemented in automobile industry because of its low sizes, low cost, low power consumption. Extensive use of MEMS sensors and actuators are being used today in smart vehicles with multiples functionalities. In automobile industry, pressure sensors, and accelerometers are two big names as far as the MEMS sensors are concerned. These sensors are implemented in automobiles in such a way so that the vehicle can function well in extreme environmental conditions. Use of microacclerometers in air bag deployment to prevent the driver from being injured in a vehicle collision is a great promo of MEMS applications in automobiles. Displacement sensors and pressure sensors in suspension systems, position sensors in antilock braking systems, gyroscope in navigation, displacement sensors and microvalves in seat control, pressure sensors and temperature sensors in vehicle diagnosis and health monitoring are few examples of MEMS applications in automobiles

1.3.2 Biometrics

Biometrics is an important field for MEMS applications and has attracted immense attention in recent past since data security has become a concern nowadays in every aspect of life. Typical security options like PIN, passwords, and optical readers are becoming obsolete in the era of more advanced and reliable MEMS biometric sensors. Integration of nanotechnology and MEMS in the imaging sensors has displayed tremendous improvement in resolution, linearity, responsivity, random noise, uniformity and so on. Different types of MEMS sensors such as capacitive fingerprint sensor, ultrasonic fingerprint sensor, piezoelectric, and piezoresistive fingerprint demonstrate more accurate and sophisticated biometric sensing than typical optical scanners. Therefore, old imagining techniques such as optical scanners which are considered to be bulky, slow and expensive option compared to MEMS based scanners are being successfully replaced by the MEMS biometric sensors (e.g, MEMS fingerprint sensors).

1.4 Piezoelectric materials: State of the art

There are many materials that show piezoelectric properties. But not all the materials can be used in piezoelectric applications due to their weak piezoelectric properties. Though many materials show good piezoelectric behaviors but again due to their incompatibility with technological process or specified growth condition, they are not used for piezoelectric micro or nano device fabrication [2]. However, there are still few materials which are considered to be compatible in micro-processing. Because of their compatibility with micro fabrication, these materials are used in various applications as piezoelectric films such as in acoustic wave devices, wireless communication, MEMS sensors, MEMS actuators and so on [3,4,5]. However, the investigated piezoelectric materials that have grown attention over the years are lead zirconate titanate (PZT), lithium niobate (LiNbO3), zinc oxide (ZnO) and aluminum nitride (AlN) [3,4,6]. Although, in recent times there is a worldwide movement to make products lead-free, so the notion involving lead is perhaps diminishing the interest in lead titanates.

Typically, most piezoelectric materials are made of nitrides and oxides of metals and semiconductors and act like inert materials. Temperature is a vital factor while depositing the piezoelectric material to form sensors or actuators. Generally, the deposition temperature ranges from 200 ºC to 800 ºC [7]. However, good piezoelectric properties can be achieved by having good stoichiometry and morphology of the materials. To achieve these, the piezoelectric materials need proper seed layers as well as proper control of the nucleation, growth, and crystallization processes. In spite of having such challenges, low cost and high quality deposition processes of different piezoelectric materials, for example, AlN film deposition using DC sputtering process, ZnO thin film deposition using RF magnetron sputtering and lead zirconate titanate (PZT)

films deposition using chemical solution deposition (sol-gel) have enabled to integrate these materials into microsensors successfully.

In 1998, E. Kalvesten *et al.* [8] made a surface micromachined pressure sensor for blood pressure measurements that had been commercialized for the first time. By using a polysilicon surface micromachining process, a silicon chip with the dimensions of (100 x 150 x 1300) μm^3 and a polysilicon diaphragm area of (10^3 x 10^3) μm^2 had been fabricated.

In their paper, Vladimír Kutiš *et al.* [9] examined the modeling and simulation of piezoelectric MEMS pressure sensor which was AlGaN/GaN based circular high electron mobility transistor (C-HEMT) structure. They showed how the influence of the residual stress plays an important role in correct modeling of MEMS piezoelectric pressure sensor. Wei Zhou *et al.* [10] did analytical modeling of a piezoelectric multi-layer cantilever and they used the cantilever as a MEMS chemical sensor. In their experiment, selectively coated micro-cantilevers were developed for highly sensitive chemical sensor applications. M. Baù *et al.* [11] discussed the use of piezoelectric thick films based on lead zirconate titanate (PZT) deposited by screen printing and direct writing techniques on different substrates, including alumina, steel and silicon, for sensors. Resonant sensors with contactless interrogation by means of a gated technique were experimentally demonstrated on humidity and temperature sensing.

1.5 AlN as a promising piezoelectric material in flexible MEMS sensors: state of the art

According to Friedel Gerfers *et al.* [12], AlN films, as far as the piezoelectric materials are concerned, have been rather less investigated than PZT and ZnO films because of its smaller piezoelectric constant. However, its temperature/humidity stability [13], higher signal-to-noise ratio [14] and the compatibility with CMOS processing are making it more popular in the field of nanotechnology [15]. Moreover, AlN is a large band

gap material (6 eV) with a large resistivity. On the contrary, ZnO is a semiconductor and a piezoelectric material with a band gap of 3eV that holds the intrinsic risk of increased conductivity because of off-stoichiometry. This low DC resistivity due to high conductivity turns into a high dielectric loss at low frequencies, which is especially harmful for sensor and actuators operating at frequencies lower than 10 kHz [14]. Due to these reasons AlN has the upper hand over ZnO which means AlN is better suited for deflection devices (especially for sensors), while ZnO is better suited for longitudinal bulk acoustic wave generation as it yields larger coupling coefficients for longitudinal BAW generation.

Between PZT and AlN, PZT displays a dielectric constant which is 100 times higher than AlN. Moreover, its (PZT) piezoelectric coefficients are almost 10 times higher than that of AlN. But, for a given strain, PZT produces almost 10 times lower electric field than AlN which makes AlN more suitable for sensor applications than PZT. So, for sensor applications where output parameter is voltage AlN is more suitable than PZT whereas for energy harvesting applications, PZT can be suitable because PZT produces more energy than AlN due to its high electromechanical coupling.

Table 1.1 lists the typical piezoelectric properties of AlN, ZnO and PZT thin films [7].

Property	Units	AlN	ZnO	PZT thin film
Density	g/cm^{-3}	3.26	5.68	7.5-7.6
k_t^2	%	6.5	9	7-15
Q_m @2 GHz		2490	1770	
$k_t^2 Q_m$ @2 GHz		160	160	
$e_{31,f}$	C/m^{-2}	-1.05	-1.0	-8 to 12
$d_{33,f}$	pm/V	3.9	5.9	60-130

AlN thin film has been used in a wide range of piezoelectric applications, from the in-vitro biosensors, the pressure sensors to the actuators of precision components which are capable of simulating realistic locomotion [16]. Because of its magnificent properties like piezoelectricity, AlN has been applied in surface acoustic wave (SAW) devices and

bulk acoustic wave (BAW) devices. Other important applications of surface-micromachined piezoelectric sensors with AlN based films have been reported [17,18, 19, 20].

1.6 Contribution made by this dissertation work

Throughout the dissertation chapters, total three projects will be discussed that are based on AlN thin films. As of the first, cantilever based pressure sensors, there are not many literatures review on flexible cantilever based applications with AlN films and most of the techniques those were reported involve bulk-micromachining techniques. The aim of the first project is to achieve an ultrathin (i.e., 300 nm thick) AlN film along with very small feature size i.e., ~12 μm which is extremely flexible, highly responsive, compatible for CMOS integration and can be of use for many MEMS sensors, especially, for flexible MEMS sensors based application either on rigid substrate or flexible substrate. With the successful analysis of the piezoelectric AlN ultra-thin film in tri-layer cantilever sensors, the work is further extended in making of ultrahigh resolution fingerprint sensors with high sensitivity and high g piezoelectric accelerometer that do not require any power source at all. Both the sensors, fingerprint sensors and accelerometer, are supposed to operate in extremely harsh environments with a reasonable sensitivity.

AlN based piezoelectric fingerprint sensors are investigated in the second project. Pixel size and material selection are the two most important things in designing a piezoelectric fingerprint sensor. The advantage of AlN film based fingerprint sensor is that it does not require any additional power source as capacitive sensors and because of the flexibility and CMOS compatibility of AlN film, it is very suitable for flexible fingerprint sensors application. Manufacturing wise, AlN provides great option to reduce the manufacturing cost since sputtering of AlN thin film is very simple and convenient.

An ultrathin AlN based surface-micromachined accelerometer for high-g base acceleration is designed. For design, resonant frequency is the primary parameter of interest. Previous state-of-art shows that MEMS accelerometers used different techniques such as bulk-micromachining technique, SOI and surface micromachining technique. For example, commercially available accelerometer such as 480g z-axis accelerometer manufactured by NXP is the state-of-the art in this field while they use capacitive change for sensitivity measurement. AlN ultrathin film patterned on suspension beam or spring provides great flexibility and stability for the designed accelerometer. The accelerometer is designed for airbag front and side detection mainly in automobiles and satellite aircrafts applications.

1.7 Dissertation outline

The content of the dissertation is divided into six chapters. A detailed literature review is presented in each subsequent chapter. The first chapter introduces general information regarding MEMS devices and various applications of MEMS technology. Advantages of miniaturization of MEMS devices are presented. The integration of MEMS and microelectronics are discussed. Some of the previous work on AlN films is briefly reviewed. A brief review of the state of the art in materials selection is discussed. The purpose of the material selection for the scope of the dissertation is also described.

Chapter 2 presents the basic theory of piezoelectric effects, i.e., direct and converse effect, with constituent equations. The matrix formation of stress and piezoelectric coefficients are shown. The modified version of constituent equation is finally presented.

Chapter 3 has several sections. In the section 3.1, more detailed and thorough study of previous works have been introduced. In the following section, the development of the recipe of AlN film and the characterization with XRD, SEM, and EDX are

demonstrated. In section 3.3, the detailed fabrication process flow of the AlN based cantilever is described. For the fabrication of the cantilevers, starting with the cleaning of the wafer to removing sacrificial layer is thoroughly discussed step by step. More emphasis is given on the steps like deposition of AlN film by using developed recipe, deposition of Titanium (Ti) for top and bottom electrodes. In section 3.4, electrical characterization of the AlN cantilevers sensors are discussed. The block diagram and the real characterization images are shown in this section. Then, the characterization results of several cantilevers are described. Signal spectrum and Johnson noise spectral density are discussed. In section 3.5, the finite element method (FEM) based design and simulations are discussed. The design and simulation are carried with CoventorWare® software. Mesh analysis, mechanical analysis, and stress analysis are mainly discussed in this section. Then, electrical equivalent model of the cantilever sensor is presented and the theoretical analysis for calculating piezoelectric voltage and response is discussed. Also, the flexibility of the AlN based cantilever sensor is discussed and some other literature review is demonstrated. Finally, in section 3.6, discussion and conclusion is addressed regarding my work and some other related works done by the others.

Chapter 4 introduces novel design of high resolution and highly flexible fingerprint sensors. The chapter is divided into several sections. Section 4.1 discusses about the background and state of the art regarding fingerprint sensors. It also discusses the improvement that is to be made in this dissertation. There are three different fingerprint sensor designs that are going to be covered in this chapter and these are 1) 725 dpi fingerprint sensor with AlN film on top the diaphragm 2) 725 dpi fingerprint sensor with AlN underneath the diaphragm, and 3) 1016 dpi fingerprint sensor with AlN film underneath the diaphragm. Section 4.1 gives a little introduction of the sensors. In the following section, design and simulation of the fingerprint sensors are mainly discussed.

Mesh convergence study is done for each design and the 3D fabrication process flows of the sensors are discussed step by step. Dimension of the each device layers and naming of each layers are discussed at the beginning of the section. Simulation results that include stress analysis, spring constant and voltage response for each type of sensor are discussed and presented in tabular and pictorial form in section 4.3. In the following section, noise analysis is presented. Three different types of noise which includes Johnson noise current, thermo mechanical noise current and loss tangent noise current are discussed and compared for each type of sensors. Total noise current and noise equivalent pressure are also calculated in this section. Finally, in section 4.5, overall summary of this chapter is presented.

Chapter 5 describes about a novel design, simulation and modeling of an AlN based piezoelectric MEMS accelerometer. In section 5.1, different types of accelerometers and their applications are briefly discussed. A basic concept of mass spring damper system is discussed and ideal criteria and features of an accelerometer are discussed as well. Later, summary of some previous works on piezoelectric accelerometers are presented in a tabular form. In section 4.2, design and simulation of the accelerometer are thoroughly demonstrated. Design and 3D fabrication steps are discussed in step by step. Design parameters are optimized to achieve the desired resonant frequency and flexibility. Mesh convergence study is also discussed at the end of this section. In section 4.3, modal harmonic analysis, stress analysis and piezoelectric response for various range of acceleration are presented in this section. All the results are demonstrated in tabular and pictorial form. In the next section, noise analysis is analyzed theoretically. Johnson noise, noise due to squeeze film damping, and loss tangent noise due to ac resistance are discussed and compared. Minimum detectable acceleration is calculated for thermomechanical noise. After that, total noise equivalent

current and total noise equivalent noise are presented. Total noise equivalent acceleration is also calculated and presented in this section. Finally, in section 4.5, all the works discussed in the chapter are summarized.

Chapter 6 summarizes the body of this dissertation and presents an insight toward the topic of the dissertation for future work.

1.8 Summary

Flexible MEMS sensors are becoming a power source of sensors market as they provide great potential toward the smart skin technology and many other flexible substrate based applications. Flexible MEMS sensors can be easily integrated with microelectronics and can be placed together on a single chip without hampering their performance. Ultrathin AlN film provides flexibility, CMOS compatibility, improved sensitivity which helps enhance the performance of flexible sensors in many extreme environmental conditions. This research focuses on investigating the performance of ultrathin AlN film using MEMS surface-micromachining technique in various sensors based applications such as cantilever based pressure sensors, fingerprint sensors and z-axis accelerometers. Since, piezoelectricity is the nature of AlN film, therefore, AlN based sensors also does not require additional power source for any applications. Piezoelectricity, responsivity, and mechanical stability are given priorities as the primary investigation areas in this entire dissertation.

Chapter 2

Theory

2.1 Piezoelectric effects

Piezoelectric materials possess the ability to convert a mechanical input to an electrical output and vice versa. According to literatures [7], the linear or direct piezoelectric effect is seen as the generation of charge or voltage in response to applied mechanical stress or strain. On the contrary, the reversible or converse piezoelectric effect is seen as the generation of mechanical strain or stress in response to applied electric field. Some piezoelectric transducers can be configured as actuators when the device is designed in a way so that it becomes compatible to produce mechanical strain or stress by using the converse piezoelectric effect. On the other hand, some transducers can be configured as sensors when the design of the device is optimized for the production of an electric signal by using direct piezoelectric effect [7].

Usually, the crystalline piezoelectric material consists of atoms that share electron density in the form of ionic and covalent bonds. Due to this sharing, electron density mismatch is observed in the crystal; therefore electric dipoles are formed throughout the crystal. To understand better about piezoelectric effects, it needs to be explained in details with the concept of crystal structure. Most of the crystals have the structure where the atoms are distributed symmetrically. Thus those crystals remain electrically neutral since the sum of the individual dipoles between all of the atoms is zero, although, ferroelectric crystal experiences a nonzero dipole sum at equilibrium state. Once the mechanical stress is applied, the generated strain produces small amount of changes in the bond length between the atoms which results in a shift in the positions or directions of the individual dipoles. Though, the sum of the dipoles in some crystals remains zero even under the applied stress, however, in many crystals they

show a non-zero sum of the dipoles under stress which means the crystal symmetry in the latter is disturbed by the stress, subsequently resulting in a non-zero dipole sum and a strong sign of piezoelectric effect [16]. The piezoelectric effect can be demonstrated using equations which describe the electrical and structural operation of material. The components of the electric displacement field vector or electric flux density D_i can be expressed as:

$$D_i = \varepsilon_o \varepsilon_{ij} E_j \ldots\ldots \qquad (2.1)$$

Where, ε_o is considered as the permittivity of free space, ε_{ij} denotes the elements of the relative permittivity tensor and E_j are the components of the applied electric field vector. On the other hand, the mechanical strain tensor can be expressed using Hooke's law:

$$S_{ij} = s_{ijkl} \sigma_{kl} \ldots\ldots.. \qquad (2.2)$$

Where, s_{ijkl} denotes the elements of the elastic compliance tensor or inverse of stiffness tensor c (i.e., $s=c^{-1}$) and σ_{kl} denotes the elements of the stress tensor.

So, the constituent equations that can describe the piezoelectric effects showing the relationship between electrical and mechanical variables are the following [7]:

$$D_i = d_{ijk} \sigma_{jk} + \varepsilon_o \varepsilon_{ij}^{\sigma} E_j \quad \text{…(for piezoelectric effect)} \qquad (2.3)$$

$$S_{ij} = s_{ijkl}^{E} \sigma_{kl} + d_{kij} E_k \quad \text{…(for converse piezoelectric effect)} \qquad (2.4)$$

In an alternative manner,

$$\{D\} = [d]\{\sigma\} + [\varepsilon^{\sigma}]\{E\} \quad \text{…(for piezoelectric effect)} \qquad (2.5)$$

$$\{S\} = [s^{E}]\{\sigma\} + [d^{t}]\{E\} \quad \text{…(for converse piezoelectric effect)} \qquad (2.6)$$

Where, d_{ijk} denotes the components of the piezoelectric (strain) coefficient tensor that determines the piezoelectric properties of the material, the superscript E in the equation (2.4) and (2.6) indicates a zero or constant electric field while the superscript σ

indicates a zero or constant stress field, and the superscript t indicates the transposition of a tensor [16].

Stress matrix σ_{kl}, however, has total nine components which includes 6 shear stresses ($\sigma_{32,}\ \sigma_{23}, \sigma_{31}, \sigma_{13}, \sigma_{21}, \sigma_{12}$) and 3 normal stresses ($\sigma_{11}, \sigma_{22}, \sigma_{33}$) (i.e., notation 11, 22, 33 indicates the normal stress, and rest of the notation for stress symbols indicates the shear stress). The piezoelectric coefficient matrix basically depends on the crystal system and the class of the piezoelectric material. For AlN, it belongs to the hexagonal crystal system with a class of 6mm [21]. Therefore, the coupled equations of strain-charge form [Equation (2.5) and (2.6)] can be then written as:

$$\begin{bmatrix} \mathrm{D}_1 \\ \mathrm{D}_2 \\ \mathrm{D}_3 \end{bmatrix} = \begin{bmatrix} 0 & 0 & 0 & 0 & \mathrm{d}_{15} & 0 \\ 0 & 0 & 0 & \mathrm{d}_{24} & 0 & 0 \\ \mathrm{d}_{31} & \mathrm{d}_{32} & \mathrm{d}_{33} & 0 & 0 & 0 \end{bmatrix} \begin{bmatrix} \sigma_1 \\ \sigma_2 \\ \sigma_3 \\ \sigma_4 \\ \sigma_5 \\ \sigma_6 \end{bmatrix} + \begin{bmatrix} \varepsilon_{11} & 0 & 0 \\ 0 & \varepsilon_{22} & 0 \\ 0 & 0 & \varepsilon_{33} \end{bmatrix} \begin{bmatrix} \mathrm{E}_1 \\ \mathrm{E}_2 \\ \mathrm{E}_2 \end{bmatrix}; \text{ and}$$

$$\begin{bmatrix} S_1 \\ S_2 \\ S_3 \\ S_4 \\ S_5 \\ S_6 \end{bmatrix} = \begin{bmatrix} s_{11}^E & s_{12}^E & s_{13}^E & 0 & 0 & 0 \\ s_{21}^E & s_{22}^E & s_{23}^E & 0 & 0 & 0 \\ s_{31}^E & s_{32}^E & s_{33}^E & 0 & 0 & 0 \\ 0 & 0 & 0 & s_{44}^E & 0 & 0 \\ 0 & 0 & 0 & 0 & s_{55}^E & 0 \\ 0 & 0 & 0 & 0 & 0 & s_{66}^E = 2(s_{11}^E - s_{22}^E) \end{bmatrix} \begin{bmatrix} \sigma_1 \\ \sigma_2 \\ \sigma_3 \\ \sigma_4 \\ \sigma_5 \\ \sigma_6 \end{bmatrix} + \begin{bmatrix} 0 & 0 & d_{31} \\ 0 & 0 & d_{32} \\ 0 & 0 & d_{33} \\ 0 & d_{24} & 0 \\ d_{15} & 0 & 0 \\ 0 & 0 & 0 \end{bmatrix} \begin{bmatrix} E_1 \\ E_2 \\ E_3 \end{bmatrix}$$

Where, the notations for stress are replaced by the following format. $\sigma_{11}, \sigma_{22}, \sigma_{33}, \sigma_{32,}\ \sigma_{23}, \sigma_{31}, \sigma_{13}, \sigma_{21}, \sigma_{12}$ can be rewritten as $\sigma_1, \sigma_2, \sigma_3, \sigma_{4,}\ \sigma_4, \sigma_5, \sigma_5, \sigma_6, \sigma_6$.

Another way to look into the piezoelectric theory is to apply normal strain in the constituent equation for direct piezoelectric effect instead of stress. Equation (2.3) can be rewritten with the strain component instead of stresses.

$$D_m = e_{mn} S_n + \varepsilon_0 \varepsilon_{mp}^S E_p \tag{2.7}$$

Where *D, S, E, e*, and *ε* are denoted as the electric flux density or electrical displacement, mechanical strain, electric field, strain piezoelectric coefficient, and

permittivity of the piezoelectric material whereas, ε_0= the permittivity of the free space = 8.854×10^{-12} F/m and ε_{mp}^S is denoted as the permittivity of the material at constant strain. The subscripts in the Equation (2.7) $m = 1,2,3; p = 1,2,3,$ and $n = 1,2,3, \ldots.,6$ describes the direction to which the physical properties are involved. The subscripts in e_{mn} represents the charge collected due to piezoelectricity in the plane perpendicular to m direction due to the applied strain in the n direction. Since AlN belongs to the group of 3 mm [21], the piezoelectric coefficient matrix e_{mn} can be represented into the following form (Equation 2.8).

$$e = \begin{pmatrix} 0 & 0 & 0 & 0 & e_{15} & 0 \\ 0 & 0 & 0 & e_{15} & 0 & 0 \\ e_{31} & e_{31} & e_{33} & 0 & 0 & 0 \end{pmatrix} \tag{2.8}$$

Since, aluminum nitride shows piezoelectricity in c-axis or (0002) direction, the electrical displacement or electric flux density D_3 is hence calculated. Being a vector field, D_3 is defined as the free and bound charge collected across the piezoelectric material. The expression for D_3 can be expressed as the following:

$$D_3 = \frac{Q_T}{A_{AlN}} \tag{2.9}$$

Or,

$$Q_T = \oiint_{x=0,y=0}^{x=w,y=l} D_3 . dxdy \tag{2.10}$$

Where Q_T and A_{AlN} are the total charge and total area of the sensing element, respectively. Q_T for a cantilever beam, for example, is basically the integration of electrical displacement D_3 over the whole area of the sensing element. In Equation (2.10), *w* and *l* are the width and length of the sensing element. Equation (2.9) can be rewritten in a different way using equation (2.7), provided that there are no external electric fields [22]:

$$D_3 = e_{31}(S_1 + S_2) + e_{33}S_3 \tag{2.11}$$

Where S_1, S_2 and S_3 are the normal strains in the rectangular coordinate system (i.e., x, y and z direction) and the electrical displacement D_3 in any point is therefore the sum of all the normal strains multiplied by their corresponding piezoelectric constants. Since e_{31} and e_{32} are equal, therefore, only e_{31} was used in Equation (2.11). So, using Equation (2.10) and (2.11), Q_T can be calculated.

Finally, the capacitance of the AlN thin film is calculated and the static piezoelectric output voltage due to loading is calculated using the following equation.

$$V = Q_T/C \tag{2.12}$$

In literatures, the values of different piezoelectric coefficients have been already mentioned. Those values will later be used in modeling the parameters (e.g., piezoelectric response) for the piezoelectric cantilevers, piezoelectric fingerprint sensors, and piezoelectric accelerometers as part of the piezoelectric voltage response modeling.

Chapter 3

Ultra-thin AlN based cantilevers for flexible MEMS sensors

3.1 Introduction

Aluminum nitride, in recent years, has become a great source of interest to many researchers due to its excellent mechanical and piezoelectric properties. Many studies over the past several years show that AlN shows multiple number of excellent characteristics that include its wide energy band gap (6.2 eV), high electrical resistance, good thermal conductivity (260 $Wm^{-1}K^{-1}$), high breakdown voltage, good chemical stability, high melting point (2400 °C), low acoustic impedance, good acoustic velocity (6,000 m/s), good signal to noise ratio, low deposition temperature (below 400 °C) and good electromechanical coupling [23],[24],[25]. These strong properties of AlN films has made it a very popular material in many important applications of electroacoustic devices such as bulk acoustic wave (BAW) and surface acoustic wave (SAW) devices [26],[27],[28]. On top of that, it has also gained interest in MEMS applications such as in MEMS force sensors, pressure sensors, chemical sensors, micro-actuators, accelerometers, fingerprint sensors, piezocapacitiors and piezoelectric energy harvesters due to its good piezoelectric properties [29],[30],[31]. Though MEMS sensors have been fabricated on rigid Silicon substrate for a long time, it appears that they can be also fabricated on flexible substrates and flexible electronics along with microsensors can be easily integrated on flexible substrates which enable the applications of wearable or skin-attachable electronic devices known as smart-skin or electronic-skin for robotics [32], and biomedical applications that includes prosthetic devices [33], body-motion signals [34], pH measurement [35] to name a few.

In our study, ultra-thin (≤300 nm) AlN cantilevers have been developed to yield high flexibility and high piezoelectric response. Low deposition temperature (i.e., 300 ºC)

was used while sputtering the AlN film. The low deposition temperature of AlN film allows for CMOS compatibility and monolithic integration of a variety of AlN based piezoelectric MEMS sensors. The flexible cantilever structure allows the investigation of the piezoelectric and mechanical properties of AlN and forms the basis for future force/pressure sensors, accelerometers, and fingerprint sensors. The characterization of multiple cantilevers was performed to measure the response of the AlN. For characterization, forces were applied with a nanopositioner and a probe to displace the cantilevers at different frequencies and measure the direct piezoelectric response as rms voltage with a signal analyzer, the applied load was monitored simultaneously with a load cell. The voltage responses and the average Johnson noise floor of the power spectral density of the cantilevers were measured. CoventorWare® simulations were used to model the mechanical stress and displacement of the cantilevers. A mathematical calculation was done to verify the experimental results with its calculated counterpart. Noise performance of the cantilevers was also analyzed and noise equivalent force (NEF) was calculated. As the demand of the flexible sensors are growing for wearable and implantable devices, the investigation of the properties of the ultrathin AlN films for flexible MEMS sensors will certainly open the door for the state-of-the-art technology and carry us a long way by enriching the research in the field of MEMS and nanotechnology.

3.1.1 Background and Motivation

In the era of 1960s, it was noticed [36] that monolithic silicon was able to show excellent mechanical properties and found to be compatible in transducer and actuator development. Later, silicon based microelectronics technology became very popular in manufacturing simple and microscale mechanical structures. With further scaling down, Si based technology unlocked the door of more complex MEMS devices and micro-opto-electromechanical systems (MOEMS) devices. Over the past decades, the advancement

in silicon technology has been measured by different aspects such as scaling effect, (i.e., scaling down without the loss of functionality), fast response, and low cost due to batch fabrication possibility. Improvement in features like sensitivity, accuracy, efficiency, reliability, and repeatability also have given the Si technology an upper hand over other technologies in micro device fabrication [37, 38, 39].

As far as the microstructure development is concerned, the researchers were more interested in development of new fabrication technology at the beginning rather than in micro-structure metrology or analysis of their long-term stability and failure mechanisms [40]. However, the tradition has been changed in recent years and special consideration has been given in studying microsystems reliability and developing metrological techniques for MEMS devices [41,42]. In addition to that, investigation in finding new materials that could meet the requirements for MEMS devices in terms of fabrication process, sensitivity, CMOS compatibility, work efficiency, and cost effectiveness have been going on now for years. Among the investigated materials for MEMS technology, piezoelectric materials have been found to be materials of high energy density. Also, they do not lose their properties upon miniaturization. As a matter of fact, piezoelectric thin films have gained an ever-growing interest for MEMS based research and applications in recent years [7]. The initial motivation of my PhD work came from the ever increasing popularity of piezoelectric thin films. To further narrow it down, it was aluminum nitride thin film which kept my attention since it was less investigated among the piezoelectric materials. There are many piezoelectric materials which have been studied so far. Among those, Zinc oxide (ZnO), lead zirconium titanate (PZT), Aluminum nitride (AlN) and Lithium niobate ($LiNbO_3$) have caught researcher's attention. AlN have been found to have smaller piezoelectric constants compared to lead zirconium titanate (PZT) but possess similar values if compared to zinc oxide (ZnO) films [43].

However, AlN offers the many advantages that were discussed earlier in the beginning. AlN offers compatibility with CMOS processing, which makes it more suitable for many applications in the field of nanotechnology [14]. In their paper, Wei Zhou *et al.* [10] described an analytical modeling of a piezoelectric multilayer cantilever with ZnO which was applied as a MEMS chemical sensor. To some extent similar but ultrathin AlN based piezoelectric cantilever sensors have been fabricated as part of my dissertation work.

In this chapter, novel modeling, fabrication and characterization of AlN based cantilever like pressure sensors will be discussed. The aim of this work was to investigate piezoelectric properties of ultra-thin (300 nm) AlN films with small feature size (~12 μm) for higher responsivity and flexibility. Another goal of this work was to use low deposition temperature (i.e., 300 ºC) that would enable AlN film to have the CMOS and flexible substrate compatibility.

3.2 Development of AlN Thin Films

The quality of AlN film was measured by different types of characterization. Using X-ray diffraction (XRD) technology the crystal orientation of AlN film was measured. θ/2θ patterns were used to assess the orientation of the film. The c-axis preferred orientation was found at (002) direction. Sanz-Hervas *et al.* [44] discussed that AlN films should have a good texture (002) or XRD peak in order to display good piezoelectric properties. With the change in film thickness there is a change in d_{33} piezoelectric coefficient too. They also reported that in some instances, AlN films with near epitaxial crystal quality (i.e., good (002) texture and rocking curve (rc) FWHM of around 1º) rather show negligible piezoelectric response while AlN films with ordinary crystallinity (i.e., weak (002) texture and rc FWHM of around 8º) provide a very good piezoelectric response.

In the experiments, the quality of AlN film have been observed by using several compositions of Ar and N_2 while sputtering AlN thin film on a bare silicon wafer. Also,

different temperatures were used for the sputtering of AlN while keeping the ratio of Ar and N_2 unchanged. The following Table 3.1 shows the parameters that were varied to develop a good quality film of AlN.

Table 3.1 Development of the recipe for the deposition of AlN

Combination No.	Temperatures	Ar to N_2 ratio (in percentage)
1	275 ºC	50%-50%
2		33.33%-66.67%
3		40%-60%
4		71.43% - 28.57%
5	300 ºC	83.33 % - 16.67%
6		76.93 % - 23.07%
7		71.42 % - 28.58%
8	400 ºC	83.33 % - 16.67%
9		76.93 % - 23.07%
10		71.42 % and 28.57%

Among the combinations, number 5 shows the best quality in terms of surface morphology, c-axis orientation and atomic percentage ratio between Al and N_2. Figure 3.1 shows the XRD peak pattern of AlN at c-axis or (002) orientation which is basically at 36.04º. The EDX characterization (Table 3.2) was also done to observe the stoichiometry of the AlN thin film. It shows the atomic percentage ratio maintains 1:1 ratio between aluminum and nitrogen. Figure 3.2 shows the surface morphology or texture of AlN. The surface looks smooth and uniform throughout the film.

Table 3.2 EDX analysis showing the stoichiometry between Al and N in the AlN film.

Element	Wt%	At%
N	33.63	49.40
Al	65.46	49.93
Si	00.91	00.67

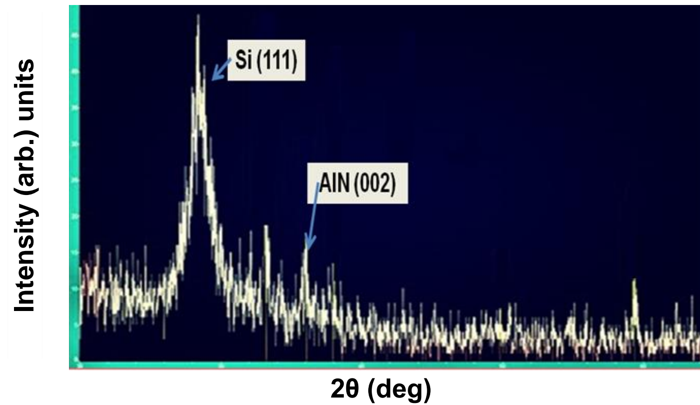

Figure 3.1 X-ray diffraction θ/2θ patterns of AlN thin film (X-ray intensity vs. 2θ) showing the c-axis orientation (002) of the AlN film at an angle of 36.04º.

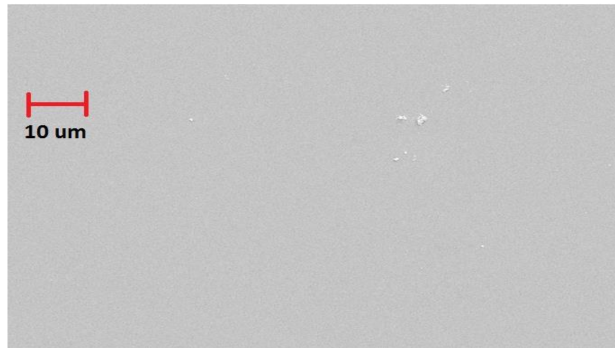

Figure 3.2 SEM image of the surface morphology of AlN thin film showing the smoothness and good uniformity of the film.

3.3 Fabrication

There were several steps in the fabrication process for the array of cantilevers. A 4 in. diameter silicon wafer was used as the substrate. After the standard cleaning process of the wafer, microfabrication was done in a class 100 clean-room. Initially, a passivation layer of Si_3N_4 was deposited followed by a ground contact layer of Ti. Both layers were sputtered by rf magnetron sputtering. The thickness measured for both layers are 0.2 μm each. After that, a sacrificial layer of polyimide was patterned using the

standard lithography process. However, the details of the fabrication steps are discussed below.

3.3.1 Patterning of the photoresist

Spin coating: Once the polyimide (HD 4104) was patterned with standard photolithography and cured in the oven, the wafer was spin coated with a lift off resist (LOR 15B) and negative photo resist (NR-7 1500PY), respectively. Initially, LOR 15B was spin coated over Ti contact layer. The following table gives a description of this step.

Table 3.3: spin coating

Photoresist	Spinning for 10 sec at	Spinning for 40 sec at	Soft baked on hotplate at 170 °C for
LOR 15B	500 rpm with ramp at 100 rpm/s	2500 rpm with ramp at 850 rpm/s	5 minutes

Then NR7-1500PY was also spin coated on top LOR15B and then soft baked. It was done following the same recipe used in the Table 3.2.

Exposure: After the spin coating, the wafer was exposed on OAI mask aligner. Hard contact mode was used between the wafer and mask. The exposure energy used was 220 mJ/cm^2 at a power of 20 mW/cm^2. Therefore, the time required for the exposure

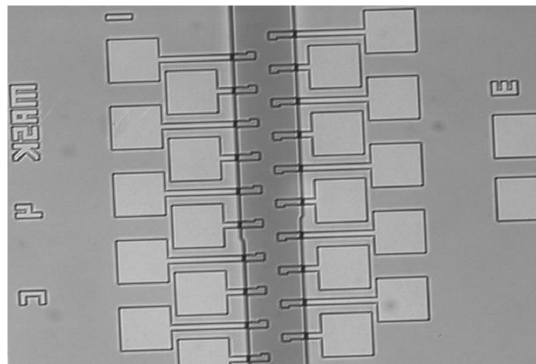

Figure 3.3 The confocal image after the pattern of photoresist. The straight mesa structure shows the polyimide layer (after cure).

was 11 seconds. The exposure wavelength of the UV lamp was i-line (365 nm). After the exposure, post exposure bake (PEB) was done for 2 minutes at 120 ºC.

Development: The wafer was then developed with Resist Developer RD6 for 70 seconds. After that, post development bake (PDB) was done for 2 minutes at 120 ºC. Then, the thickness of the patterned photo resist (LOR+NR7 1500PY) was measured. Average thickness found for the photo resist was 2.77 µm.

3.3.2. Deposition of Titanium film (bottom electrode)

The first layer of the Ti/AlN/Ti tri-layer stack was Ti layer which was also considered as bottom electrode. It was deposited by RF sputtering technique with the Homebuilt Sputter system. The sputtering process was done for 15 minutes at room temperature. The Ti target, of 99.999% purity, was kept cool during the entire time of the deposition with water on the backside. The RF (forward) power used in the process was 150 W. The reflected power showed in the reading display was 0 W all the time. Ar gas was used to create plasma inside the chamber and the flow rate maintained for Ar was 50 sccm. Besides, to create the plasma, pressure was increased up to 35 sccm initially. After the plasma formed, the pressure was reduced down to 7.3 mTorr. To avoid any unwanted particles from the target, it was cleaned with pre sputtering for 2-3 minutes keeping the shutter closed. After that, the shutter was opened and sputtering was carried

Table 3.4 Deposition parameters of the bottom electrode

Parameters	Values
Target	Ti
Material deposited	Ti
Chamber base pressure	1.5×10^{-6} Torr
Time to reach the base pressure	10 hours
Chamber pressure for deposition	7.3 mTorr
Distance between target and wafer	3.5 "
RF power	150 W
Reflected power	0 W
DC bias voltage	318 V
Ar gas flow rate	50 sccm
Deposition time	15 minutes

on for 15 minutes before it was stopped. The expected thickness for Ti was approximately 213.3 nm at a deposition rate 2.37 Angstrom/sec. The deposition of the Ti thin films was achieved according to the parameters shown in Table 3.4.

3.3.3. Deposition of AlN film

The AlN film was deposited on bottom electrode (i.e., Titanium) by a AJA sputtering machine. Sputtering was performed by DC magnetron sputtering at 300 ºC (i.e. 573K) for 2.5 hours long. The chamber pressure during the deposition is kept 3.5 mTorr. 30% of the maximum power (500 W) was used as forward power while the reflected power measured was 0 W. Meanwhile the Al target, of 99.999% purity, was cooled with water on the backside and it was put on gun#3 inside the chamber. There were four basic steps for the entire sputtering process. These were: 1) Al target spark, 2) pre-sputter, 3) AlN deposition, 4) wafer cooling down. The first step was actually required to initiate plasma into the chamber. The second step which is pre-sputter was important for two reasons. Firstly, it was the step when the temperature ramps up from room temperature (i.e. 23 ºC) to 300 ºC and secondly, since, the shutter was closed, it allowed the surface of the target to be cleaned before AlN was deposited. It took 10 minutes for the temperature to rise to 300 ºC from the room temperature. After that, the shutter was opened and the reactive sputtering started to act. During this step the N_2 and Ar flow rate were kept 10 sccm and 50 sccm, respectively. The last step was all about wafer cooling. It was programmed in the computer such a way so that the temperature was reduced down to less than 50 ºC. The expected thickness for AlN was approximately 300 nm at 0.35 angstrom/sec. The deposition of the AlN thin films was accomplished according to the parameters shown in Table 3.5.

Table 3.5 Sputtering conditions for the deposition of the AlN thin films

Parameters	Values
Target	Al
Material deposited	AlN
Load lock pressure	3.4×10^{-6} Torr
Chamber pressure	1.1×10^{-7} Torr
Process temperature	300 ºC
pressure during deposition	3.5 mTorr
Ar flow rate	50 sccm
N_2 flow rate	10 sccm
DC magnetron power	150 W
Deposition time	150 minutes

3.3.4. Deposition of Titanium film (Top electrode)

This was the final layer before liftoff. To create the layer of top electrode, Ti was deposited using the same sputtering technique as it was done for the bottom electrode. But the parameters used here were slightly different from the one used while deposition

Table 3.6 Deposition parameters of the top electrode

Parameters	Values
Target	Ti
Material deposited	Ti
Chamber base pressure	$<2\times10^{-5}$ Torr
Time to reach the base pressure	3 hours
Chamber pressure for deposition	7.4 mTorr
Distance between target and wafer	3.5"
RF power	150 W
Reflected power	0 W
DC bias voltage	315 V
Ar gas flow rate	50 sccm
Deposition time	15 minutes

of Ti for bottom electrode. The parameters used for the deposition of Ti are shown in Table 3.6.

3.3.5. Lift Off

After depositing the final layer of the Ti/AlN/Ti tri-layer, the wafer was immersed into 1165 stripper solution for the lift off process. Since the lift off process was really slow,

it was kept in the solution for long time (i.e., 162 hours). Meanwhile, the solution with wafer was put onto the ultrasonic cleaner to accelerate the lift off process. It was observed that there was no significant change in the lift off without the ultrasonic cleaner. After trying the ultrasonic cleaner, it was observed that the liftoff started working. Approximately 3 hours of agitation was done in the ultrasonic cleaner during this liftoff process.

3.3.6. Ashing

After the lift off process, the wafer was observed carefully under Confocal and Nomraski microscope. It was observed that there were some good portions as well as bad portions. The following picture shows the picture of cantilever before ashing. After making sure that we would have a significant numbers of good cantilevers, the wafer was put into the Diner Asher until the polyimide (sacrificial) layer was completely removed off. O_2 gas was used to create plasma during the removal of polyimide layer. The whole process of ashing was done applying the following parameters in the Table 3.7. Figure 3.4 and Figure 3.5 show SEM image of a cantilever and step by step fabrication process, respectively. In the next sub-chapter, the characterization of the cantilevers will be discussed in details.

Table 3.7 Parameters used during the ashing process

Parameters	Values
Gas used	O_2
Chamber pressure	0.8 mbar
Forward power	150 W
Reflected power	0 W
Process temperature	23 ^{o}C
Ashing time	84.8 hours

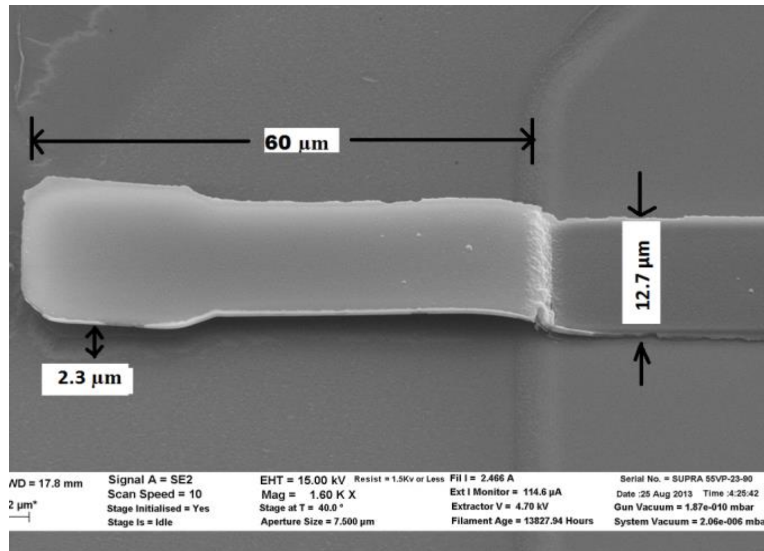

Figure 3.4 SEM image of a fabricated cantilever sensor (Bond pad is not shown). Measured dimensions: length=60 μm, width=12.7 μm, total thickness = 0.7 μm [45] (Reprinted with permission. M. S. Rayhan, D. P. Butler, and Z. Çelik-Butler, "Ultra-thin Film Piezoelectric AlN Cantilevers for Flexible MEMS Sensors," in Proc. 2015 IEEE Sensors Conf., Busan, Korea, Nov 1-4, 2015 © 2015 IEEE)

3.4 Characterization

3.4.1 Characterization of the cantilevers

After the fabrication of the AlN cantilever, the wafers consisting arrays of the AlN cantilevers were characterized with a load cell. Only good cantilevers were tested and bad cantilevers were marked to be discarded. The technique for the characterization was to induce an electric potential across the titanium electrodes due to mechanical deformation due to the piezoelectric effect. Figure 3.6 shows the block diagram of the experimental set-up. After placing the wafer on the xyz stage of the Micromanipulator probe station, the vacuum pump was turned on. A rectified square wave signal with a low

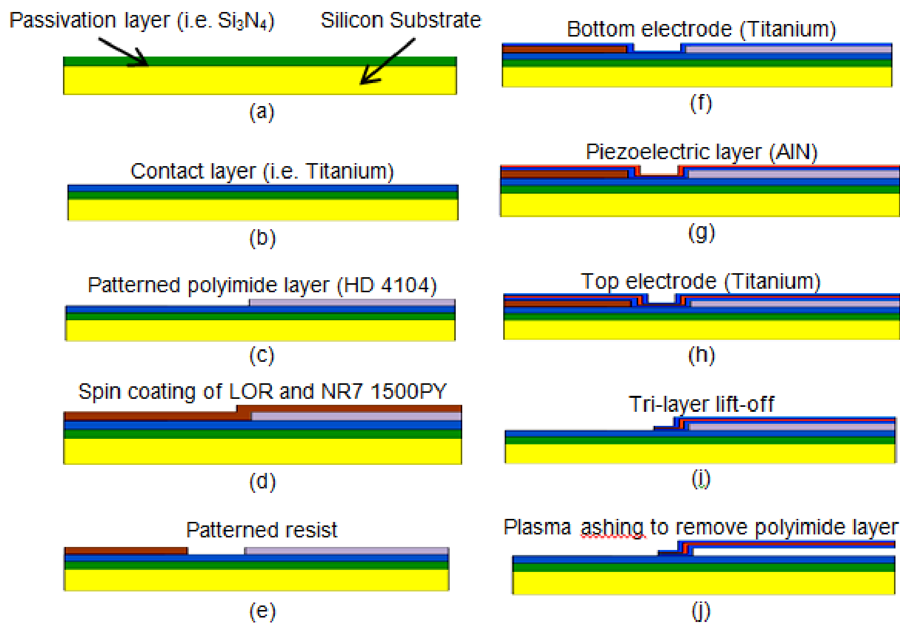

Figure 3.5 Fabrication steps for tri-layer cantilever. (a) Deposition of passivation layer, (b) deposition of contact layer, (c) photolithography of polyimide layer, (d) spin coating of LOR and NR7 1500 PY photoresist (e) pattering of the photoresists, (f) deposition of Ti, (g) deposition of AlN at 300 ^{0}C, (h) deposition of Ti, (i) liftoff of the tri-layer (Ti/AlN/Ti), (j) plasma ashing to remove the polyimide (sacrificial) layer [45] (Reprinted with permission. M. S. Rayhan, D. P. Butler, and Z. Çelik-Butler, "Ultra-thin Film Piezoelectric AlN Cantilevers for Flexible MEMS Sensors," in Proc. 2015 IEEE Sensors Conf., Busan, Korea, Nov 1-4, 2015 © 2015 IEEE)

frequency and amplitude (e.g., 3 Hz) was applied to E-665 CR controller for the characterization of the cantilevers. A corresponding signal was fed to the nanopostioner which was connected to a GS0-10 load-cell. The probe moves in z-direction (Figure 3.6) and hence applies force on top of the cantilever tip. A corresponding force reading was shown on DPM-3 load cell meter. The unit of force was shown in 'grams'. The piezoelectric cantilever experiences electric potential across the electrodes due to the

mechanical strain and piezoelectric properties of the AlN. The response across the electrodes was detected using two probes to connect the SR560 low noise preamplifier. Then the amplified signal was measured with an Agilent 35670A dynamic signal analyzer. The RMS voltage responses and corresponding power spectral densities were analyzed for several cantilevers. The graphs for the gain corrected output voltages and power spectral densities are shown in the results section. Figure 3.7 and Figure 3.8 show the set-up for the characterization of the cantilevers also.

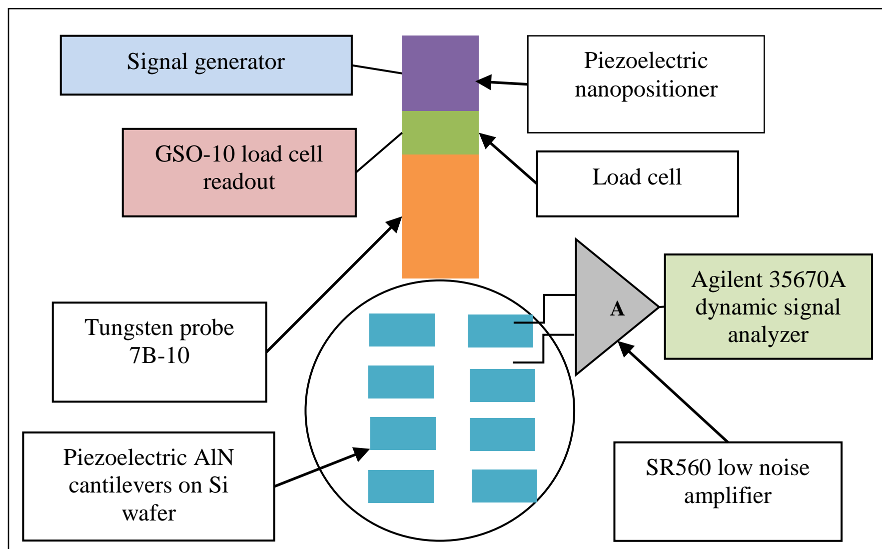

Figure 3.6 Block diagram of the set-up for the characterization of AlN cantilevers. [45] (Reprinted with permission. M. S. Rayhan, D. P. Butler, and Z. Çelik-Butler, “Ultra-thin Film Piezoelectric AlN Cantilevers for Flexible MEMS Sensors”, 2015 IEEE Sensors Conf., Busan, Korea, Nov 1-4, 2015 © 2015 IEEE)

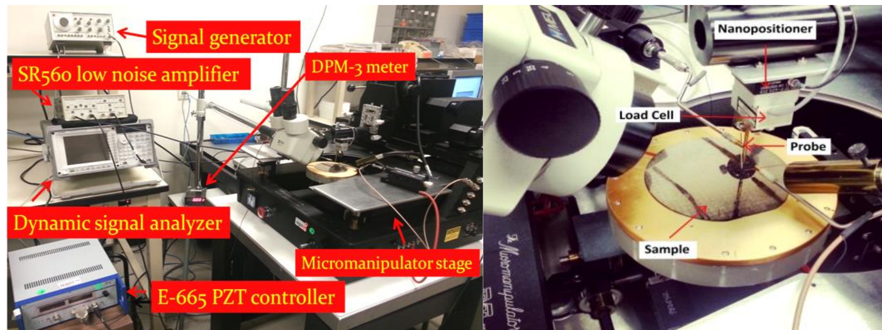

Figure 3.7 Characterization set-up: (a) physical set up for the characterization (b) a wafer containing cantilevers is under test along with a nanopositioner, load cell and three probes in a micromanipulator probe station. Two probes are used to receive electrical signal from bondpads. Another vertical probe provides the force on the cantilever in the z-direction [45] (Reprinted with permission. M. S. Rayhan, D. P. Butler, and Z. Çelik-Butler, "Ultra-thin Film Piezoelectric AlN Cantilevers for Flexible MEMS Sensors," in Proc. 2015 IEEE Sensors Conf., Busan, Korea, Nov 1-4, 2015 © 2015 IEEE)

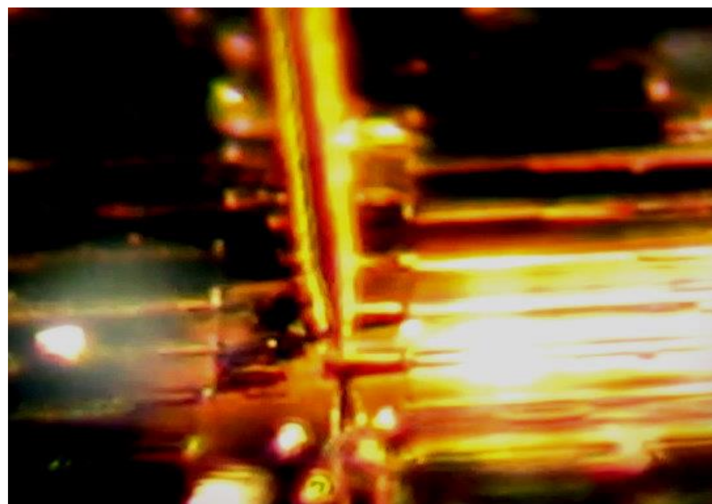

Figure 3.8 Close-up view of a cantilever that is under stress in the z-direction.

3.4.2 Characterization Results

Several cantilevers were characterized. In this section, the gain corrected peak output voltage response and corresponding power spectral density of three cantilever

sensors (*Sensor A*, *Sensor B*, and *Sensor C*) operated at different frequencies are shown. *Sensor A* was characterized using the above approach discussed earlier. The gain corrected output voltage (Figure 3.9) and the corresponding power spectral density (Figure 3.10) measured for *Sensor A* at an operating frequency of 2.5 Hz were 4.48×10^{-4} V and 2.14×10^{-6} V^2/Hz, respectively. The Johnson noise floor was measured to be 6.9×10^{-8} V^2/Hz for *Sensor A*. Similarly, *Sensor B* and *Sensor C* were also characterized. The gain corrected output voltage (Figure 3.11) and the corresponding power spectral density (Figure 3.12) measured for *Sensor B* at an operating frequency of 3 Hz were 4.18×10^{-5} V and 7.24×10^{-9} V^2/Hz, respectively. The Johnson noise floor was measured to be 7.23×10^{-12} V^2/Hz for *Sensor B*. Finally, the gain corrected output voltage (Figure 3.13) and the corresponding power spectral density (Figure 3.14) measured for *Sensor C* at an operating frequency of 3.5 Hz were 3.69×10^{-5} V and 5.70×10^{-9} V^2/Hz, respectively. The Johnson noise floor was measured to be 4.26×10^{-11} V^2/Hz for *Sensor C*. The following table will show the characterization results for several characterized cantilevers.

Table 3.8 Characterization results of the AlN based cantilevers at various frequencies

Cantilever Sensor	Operating frequency for input signal at the signal generator (Hz)	Output voltage (V)	Johnson noise floor (V^2/Hz)
Sensor A	2.5	4.48×10^{-4}	6.90×10^{-8}
Sensor B	3.0	4.18×10^{-5}	7.23×10^{-12}
Sensor C	3.5	3.69×10^{-5}	4.26×10^{-11}
Sensor D	2.5	8.17×10^{-6}	1.52×10^{-11}
Sensor E	3.5	1.95×10^{-5}	4.07×10^{-11}
Sensor F	3.0	5.66×10^{-6}	2.28×10^{-12}
Sensor G	4.0	1.12×10^{-5}	4.34×10^{-13}
Sensor H	3.0	2.58×10^{-4}	1.43×10^{-8}
Sensor I	2.5	3.37×10^{-5}	2.21×10^{-10}

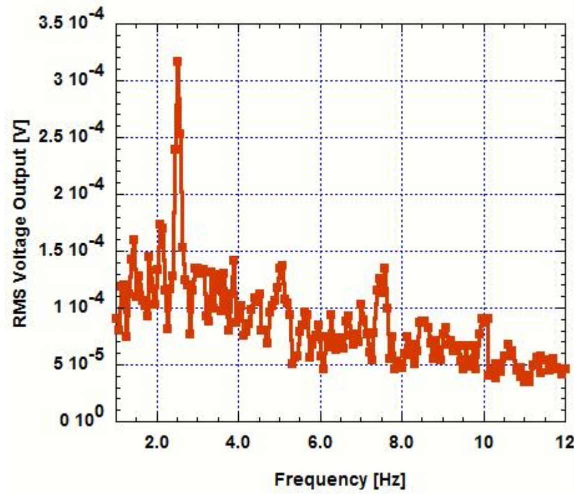

Figure 3.9 Measured gain corrected response of the *Sensor A* operating at a 2.5 Hz loading frequency. [45] (Reprinted with permission. M. S. Rayhan, D. P. Butler, and Z. Çelik-Butler, "Ultra-thin Film Piezoelectric AlN Cantilevers for Flexible MEMS Sensors," in Proc. 2015 IEEE Sensors Conf., Busan, Korea, Nov 1-4, 2015 © 2015 IEEE)

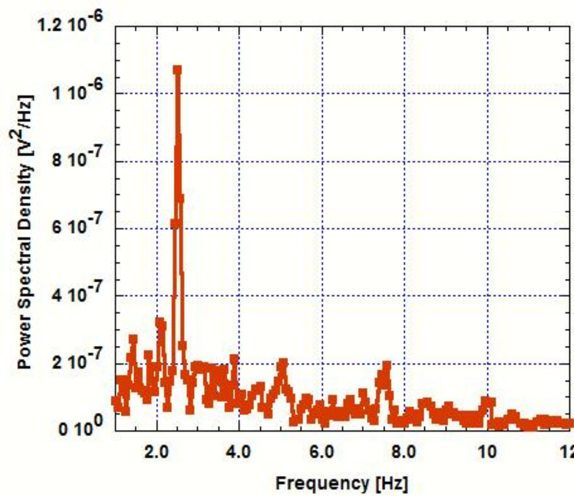

Figure 3.10 Gain corrected power spectral density of the signal from Figure 3.9 showing the Johnson noise floor. [45] (Reprinted with permission. M. S. Rayhan, D. P. Butler, and Z. Çelik-Butler, "Ultra-thin Film Piezoelectric AlN Cantilevers for Flexible MEMS Sensors," in Proc. 2015 IEEE Sensors Conf., Busan, Korea, Nov 1-4, 2015 © 2015 IEEE)

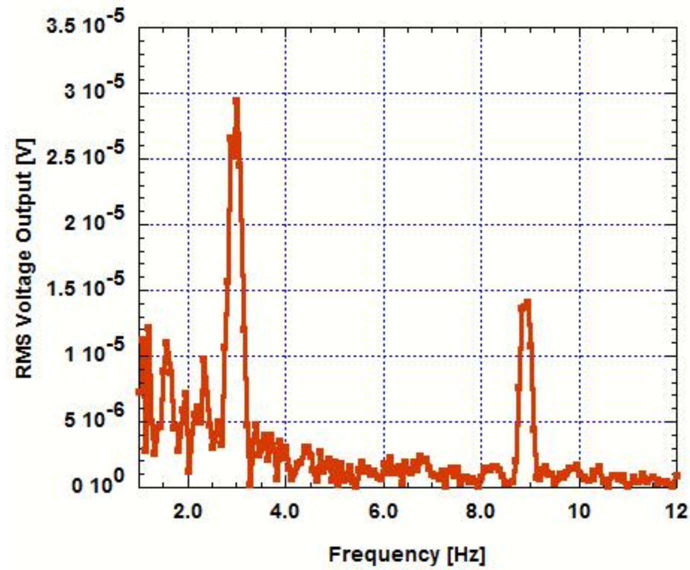

Figure 3.11 Measured gain corrected response of the *Sensor B* operating at a 3 Hz loading frequency.

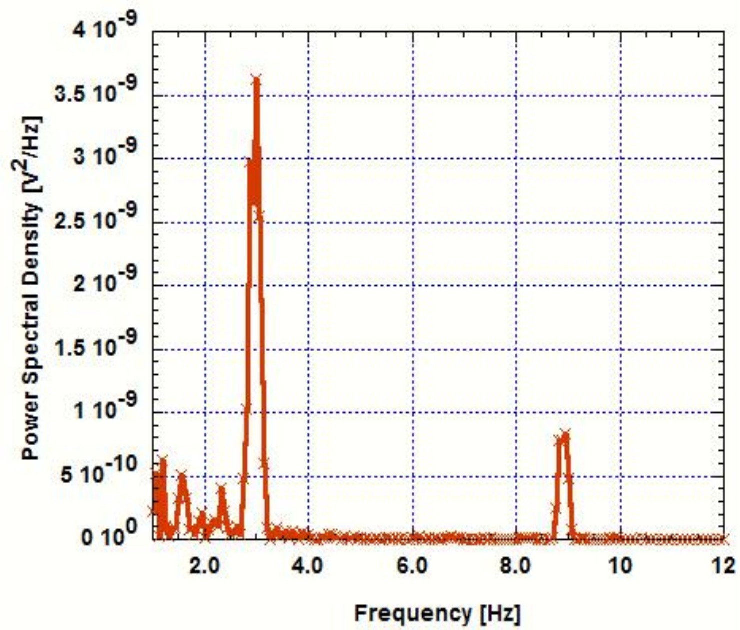

Figure 3.12 Gain corrected power spectral density of the signal from Figure 3.11 showing the Johnson noise floor.

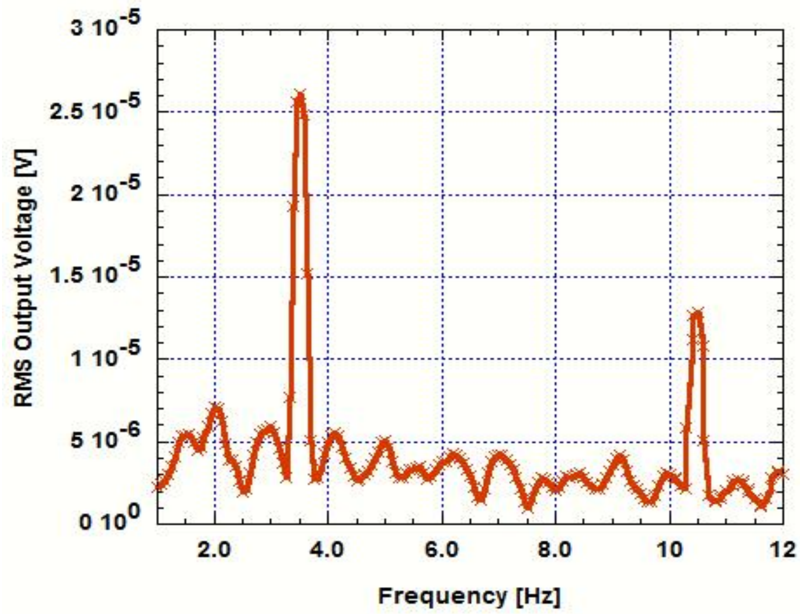

Figure 3.13 Measured gain corrected response of the *Sensor C* operating at a 3.5 Hz loading frequency.

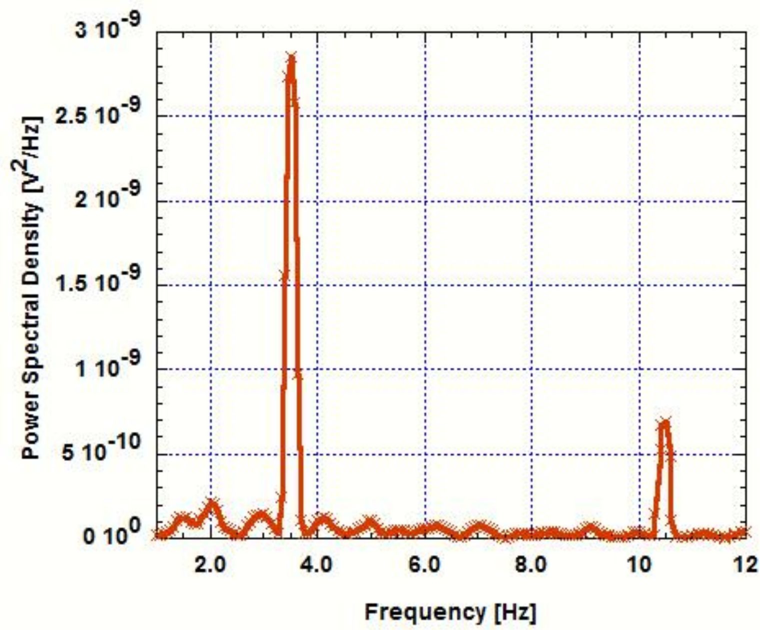

Figure 3.14 Gain corrected power spectral density of the signal from Figure 3.13 showing the Johnson noise floor.

3.5 Design, Simulation and Modeling

After the characterization, the cantilever parameters were also modeled using CoventorWare®.

3.5.1 Process editor

To start with the cantilever design, all the layers name and fabrication steps were mentioned using *process editor* in CoventorWare®. The following figure shows the layer name and corresponding thickness of the layer. A patch layer of a negligible thickness was created close to tip of the free end of the cantilever in order to apply a load on that area. All the units mentioned were in micrometer in this step.

Process Editor - [C:/Coventor/Design_Files/Bhargav/Design_Files/sajeeb_aln_cantilever/Devices/aln_cantilver_sajeeb.proc]

File Edit View Tools Windows Help

umber	Step Name	Layer Name	Material Name	Thickness	Mask Name	Photoresist	Depth	Mask Offset	Sidewall Angle
0	Substrate	Substrate	SILICON_100	50	GND				
1	Stack Material	Nitride	SI3N4	0.2					
2	Stack Material	Titanium_layer	TITANIUM	0.2					
3	Stack Material	Sacrifice	POLYIMIDE	2.3					
4	Straight Cut				anchor	-		0	0
5	Conformal Shell	bottom_electrode	TITANIUM	0.2					
6	Conformal Shell	piezoelectric_layer	AlN	0.3					
7	Conformal Shell	top_electrode	TITANIUM	0.2					
8	Straight Cut				bottom_electrode	+		0	0
9	Straight Cut				piezoelectric_layer	+		0	0
10	Straight Cut				top_electrode	+		0	0
11	Delete		POLYIMIDE						
12	Stack Material	square_patch	ALUMINUM	0.005					
13	Straight Cut				patch	+		0	0

Figure 3.15 Step name and thickness of different layers are shown in the process editor.

3.5.2. 2D Layout design

Next the masks for different layers were designed using *layout editor* in CoventorWare®. The dimensions of the mask layers are given in Table 3.9. Figure 3.16 shows the 2D layout the cantilever.

3.5.3 3D Solid model

After creating the 2D model, 3D solid model was created in CoventorWare® using preprocessor. The properties of different materials (e.g., Ti, AlN, Si_3N_4 etc.) were

defined in the library. The properties of AlN material for simulation are shown in Figure 3.17 and 3.18. The 3D solid model of the cantilever is shown next with an exaggerated view in the z-direction (Figure 3.19).

Table 3.9 Mask layers dimensions

Layer name	Dimension	
	Length	Width
GND (substrate)	300 µm	300 µm
Anchor (square shape)	90 µm	90 µm
Anchor (rectangular shape)	50 µm	13 µm
Bottom electrode (suspended)	60 µm	13 µm
AlN layer (suspended)	60 µm	13 µm
Top electrode (suspended)	60 µm	13 µm
Load patch	10 µm	10 µm

Figure 3.16 2D Layout of the cantilever including bond pad.

3.5.4. Meshing and Mechanical Analysis

The cantilever was then meshed with different types of meshing options until the meshed results had converged. For the simulation, finally ‘extruded bricks’ mesh type was chosen. The mesh size in extrude direction (z-direction) was kept very small (fine mesh) but in the planer direction (x and y direction), the mesh size was kept relatively large

(coarse mesh). The mesher settings and the meshed model of the cantilever are shown in Figure 3.20 and Figure 3.21, respectively.

Figure 3.17 Physical Properties of AlN film mentioned in *material editor.*

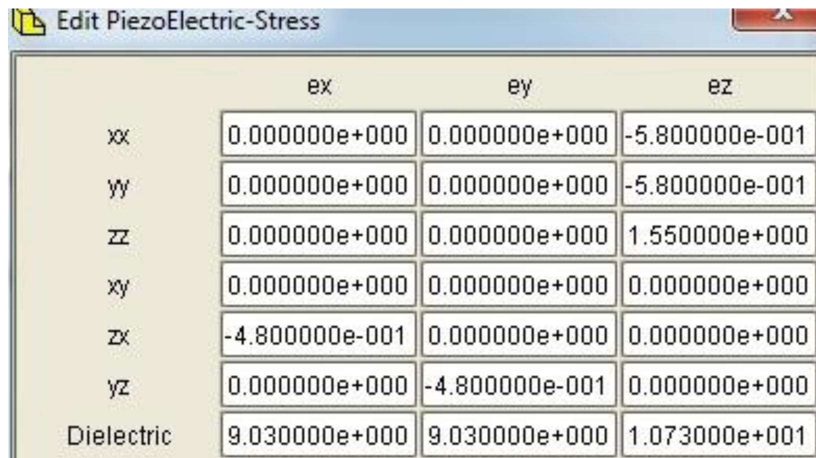

Figure 3.18 Piezoelectric coefficient matrix and dielectric constants.

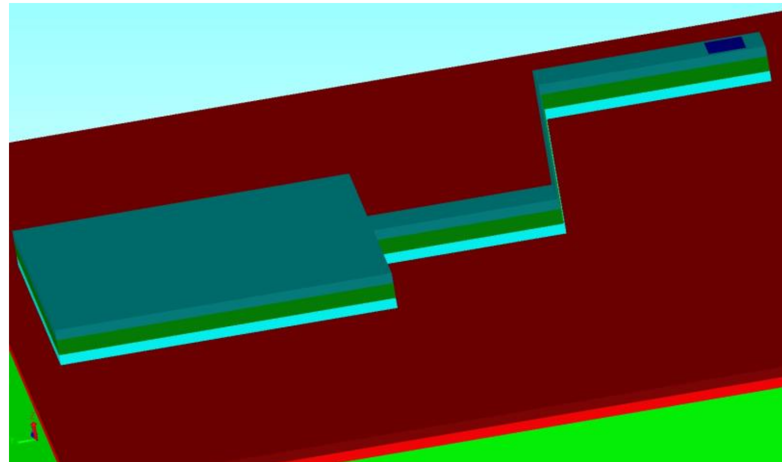

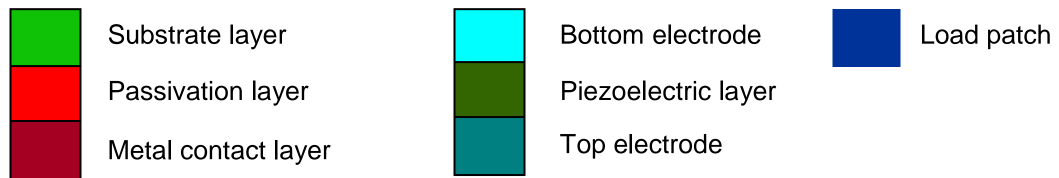

Figure 3.19 The exaggerated view (in z-direction) of the cantilever with proper labeling.

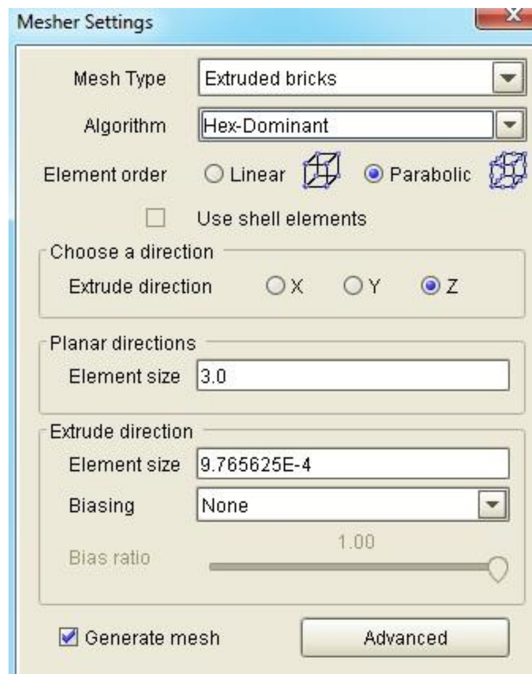

Figure 3.20 Mesher settings

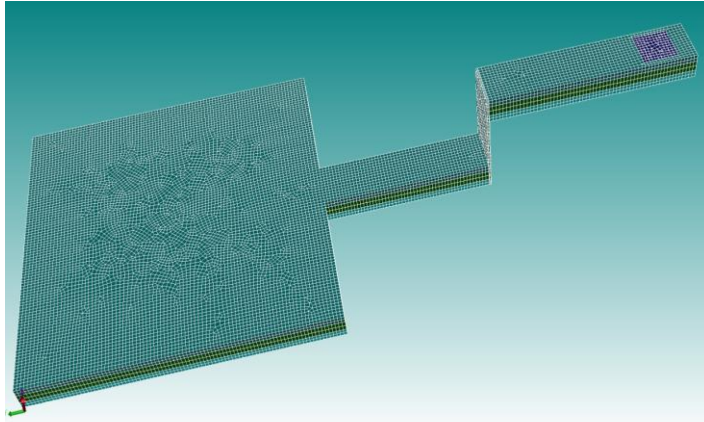

Figure 3.21 Meshed model of the cantilever

The mechanical analysis was carried out using MemMech analysis. For each new analysis, surface boundary conditions were chosen and defined (Figure 3.22) such as one of the surfaces of the cantilever structure (i.e., bottom surface) was kept as fixed and one surface (i.e., load patch) was used as load patch. Static loads (i.e., mechanical pressure) in the z-direction were put on top of the patch in the parametric mechanical analysis. Once the boundary conditions are set, simulation is run until it is completed and until it generates CoventorWare® Visualizer results. Different parameters like maximum displacements of the beam, stress in different directions, Mises stress, strain etc. are found from the simulations results (Figure 3.23). The achievable maximum displacement for the beam was 2.3 μm but to avoid the 'pull in' effect of the cantilever beam, the load was applied such a way so that the maximum displacement of the beam did not reach 2.3 μm rather somewhat near the value of the maximum displacement. Having found the simulation results, numerical modeling was done over the entire beam including the bond pad in order to find the piezoelectric charge produced by the AlN cantilevers with respect to different load and eventually to compare the calculated results with the experimental ones, hence to find the piezoelectric response from the output voltage versus load plot.

(a)

SurfaceBCs

SurfaceBCs	FixType	Patch1	and1	Patch2	and2	Patch3	LoadValue		Variable	Transient
Set1	fixAll	fixed_end	and	none	and	none	Scalar	0.0	Fixed	Fixed
Set2	LoadPatch	load_patch	and	none	and	none	Scalar	0.01	Fixed	Fixed
Set3	none	none	and	none	and	none	Scalar	[illegible]	Fixed	Fixed
Set4	none	none	and	none	and	none	Scalar	0.0	Fixed	Fixed
Set5	none	none	and	none	and	none	Scalar	0.0	Fixed	Fixed

Load patch (b) **Load value in MPa**

Figure 3.22 (a) and (b) Boundary conditions set up

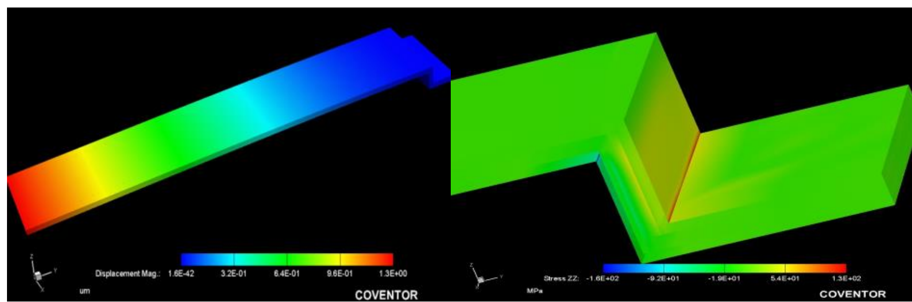

(a) (b)

Figure 3.23 CoventorWare® Visualizer results showing (a) displacement (b) Mises stress after mechanical analysis (here, applied load is 0.01 MPa in z direction).

3.5.5. Numerical Modeling

Theory and mechanism: The phenomenon that involves piezoelectric transduction is usually represented by two constitutive equations [21]. One constitutive equation is used for direct piezoelectric effect when the devices are applied as sensors (i.e., when mechanical vibration or energy is transformed into electrical signals) and the other one is used for indirect piezoelectric effect when the devices are applied as actuators (i.e., when electrical signal is transformed into mechanical energy). The scope of our research deals with direct piezoelectric transduction. Detailed theory was covered in chapter 2

Circuit model: The design of the device can be represented with an electrical circuit model. For the modeling of our cantilever sensor, the circuit model was represented using a first order RC circuit. The circuit model had three parts which include the AlN based cantilever beam, the bondpad from which the signal was carried out to the external circuits and a low noise preamplifier. External loading comes from the low noise preamplifier in terms of capacitance and resistance. In Figure 3.24, Q_C represents the cantilever or the sensor charge across the electrodes, C_C represents the sensor capacitance and R_C denotes the cantilever internal resistance whereas C_B and R_B are bondpad capacitance and bondpad resistance, respectively. C_A and R_A represent the amplifier capacitance and its resistance, respectively. The equivalent circuit of Figure 3.24 is represented in Figure 3.25. The equivalent model has an equivalent charge Q_T, an equivalent capacitance C_E (i.e., the parallel combination of the preamplifier input capacitance C_A, the bondpad capacitance C_B and the cantilever beam capacitance C_C) and an equivalent resistance R_E (i.e., the parallel combination of preamplifier input resistance R_A, and the bondpad resistance R_B and the cantilever resistance R_C). However, R_E of the equivalent circuit model was broken down into two parts; an ideal

resistance R_S and a noise current source I_N (Figure 3.25). I_N indicates the noise current related to thermal Johnson noise. For simplicity, R_S and R_E were considered to be equal. The aim of the modeling was to find the total charge (Q_T) or (Q_C) across the electrodes of the sensing part of the AlN cantilever due to induced strain up on applied force. After that, sensor dynamic output voltage (V_{so}) was calculated. To avoid confusion, it is safe to mention that Q_T in Figure 3.25 is equivalent to the Q_C of Figure 3.24 where 'T' stands for total and C stands for cantilever.

By applying Norton equivalent circuit theorem, the sensor output voltage V_{so} was calculated in the frequency domain from Figure 3.25 [22]:

$$V_{so} = \frac{sR_s}{sR_sC_E + 1} Q_T \tag{3.1}$$

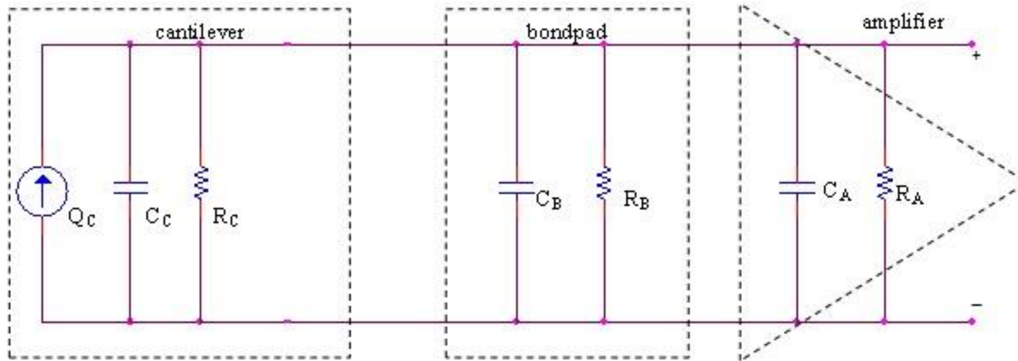

Figure 3.24 Circuit model of the AlN cantilevers including external loading.

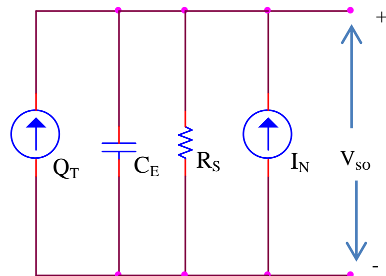

Figure 3.25 Equivalent circuit model for the piezoelectric cantilever.

The absolute value for the sensor output voltage is as follows,

$$|V_{so}| = \sqrt{\left(\frac{(sR_s)^2}{(sR_sC_E)^2 + 1^2}\right)} \cdot |Q_T| \tag{3.2}$$

However, the charge produced by the piezoelectric sensor can be also written in terms of current term in the frequency domain, such as

$$I_T = sQ_T = \frac{d}{dt}(Q_T) \tag{3.3}$$

The Johnson noise current in the circuit can be expressed by the following equation,

$$I_N = \sqrt{\frac{4k_BT\Delta f}{R_s}} \tag{3.4}$$

Where, k_B=Boltzmann's constant, T=absolute temperature, and R_s=ideal resistance, and Δf=noise bandwidth. During the mechanical simulation, with the mechanical load applied on the cantilever 'patch' in z-direction, the cantilever beam bends downward, therefore produces mechanical stress (or strain) and electric field across the AlN layer. For the numerical modeling, the known normal stresses (σ_1, σ_2, and σ_3) of each surface node of the AlN layer found in the simulation results were used to find the corresponding strains (S_1, S_2, and S_3). Then, the electric flux density (D_3 or ρ_s) of each node is calculated by using Equation (2.11). By integrating the electric flux densities over the entire sensing element using equation (2.10) total electric charge (Q_T) is calculated. To find the output voltage equation (3.2) is used and equivalent capacitance (C_E) and equivalent resistance R_E (or R_s) are calculated beforehand. To simplify the calculation, however, the dominant stresses (normal stress) in the AlN film are considered only, rest of the stresses (including shear stresses) are ignored. Since, the cantilever beam is an L-shaped structure, so the calculation for finding Q_C (or Q_T), $C_{C,}$

and R_C are done in two steps. First, Q_C, C_C, and R_C are calculated for both vertical and horizontal part of the cantilever beam separately and added together to find the total Q_C, R_C and C_C. Figure 3.26 is shown to make the explanation more understandable.

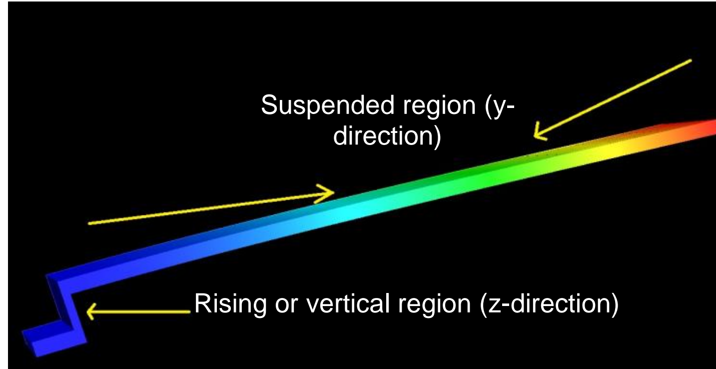

Figure 3.26 Region of the cantilever under consideration for charge calculation due to piezoelectricity.

Modeling Results: Table 3.10 shows the numerical modeling results. As discussed earlier, the piezoelectric output voltages are calculated using Equation (3.2). The calculated voltages ranges from 1.16×10^{-4} V to 4.16×10^{-5} V at different operating frequency and will be compared to the experimental voltages later. Figure 3.27 shows the plot of the calculated force response at various frequencies. It is found that the calculated voltage response varies between 66.5 V/N to 41.2 V/N.

Table 3.10 Simulation and numerical analysis results with applied load

Load, P (KPa)	Force, F (μN)	Total surface charge, Q_T (pC)	Equivalent capacitance, C_E (F)	Ideal resistance, R_s (Ω)	Voltage, V (μV)			
					For f=2.5 Hz	For f=3.0 Hz	For f=3.5 Hz	For f=4.0 Hz
10.00	1.00	265	5.58×10^{-11}	1.0×10^{8}	41.6	49.9	58.2	66.5
11.25	1.13	297	5.58×10^{-11}	1.0×10^{8}	46.6	55.9	65.2	74.5
12.50	1.25	331	5.58×10^{-11}	1.0×10^{8}	52.0	62.4	72.8	83.2
13.75	1.38	363	5.58×10^{-11}	1.0×10^{8}	56.9	68.3	79.7	91.1
15.00	1.50	395	5.58×10^{-11}	1.0×10^{8}	62.0	74.4	86.9	99.3
16.25	1.63	428	5.58×10^{-11}	1.0×10^{8}	67.3	80.7	94.2	108.0
17.50	1.75	460	5.58×10^{-11}	1.0×10^{8}	72.2	86.6	101.0	116.0

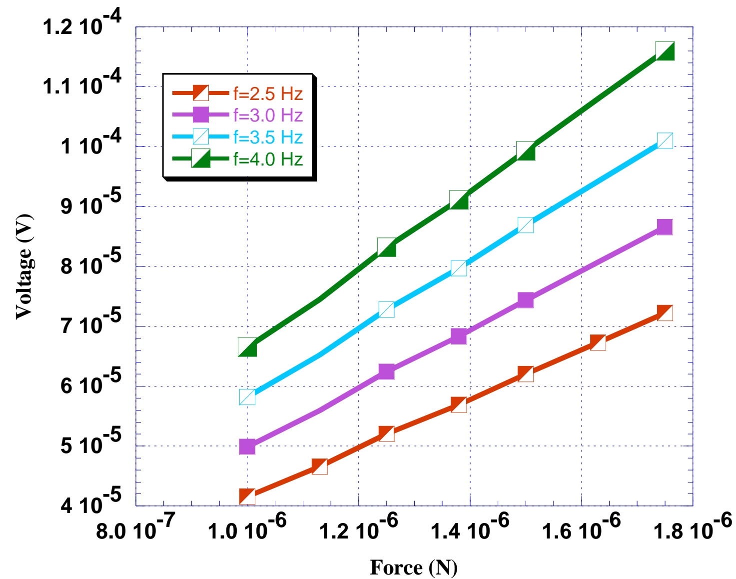

Figure 3.27 Piezoelectric responses from simulation and numerical modeling at different loading frequency (Piezoelectric voltage versus applied force).

3.6 Flexibility and Stress Analysis of the Cantilever

3.6.1 Stress analysis of the cantilever

One of our primary goals from the CoventorWare® simulation results was to observe the stress test or reliability test up on maximum deflection of the cantilever. The safe maximum deflection was assumed to be 2.23 µm in our simulation analysis. It is the maximum deflection of the cantilever tip when the applied load 17.5 KPa. Since, the actual distance between tip and contact layer is 2.3 µm, so 17.5 kPa is assumed to be the maximum threshold load above which the cantilever breaks. However, the maximum tensile and compressive stress of the AlN film was found to be 83 MPa and 74 MPa, respectively, at 17.5 kPa load. In both cases, the stresses are lower than their ultimate strengths. From literatures, it is found that the tensile strength and compressive strength of AlN film are 340 MPa [46] and 1.5 GPa~4.0 GPa [47], respectively. For Ti film, the maximum Mises stress from simulation was to be 305.5 MPa at 17.5 kPa load which is

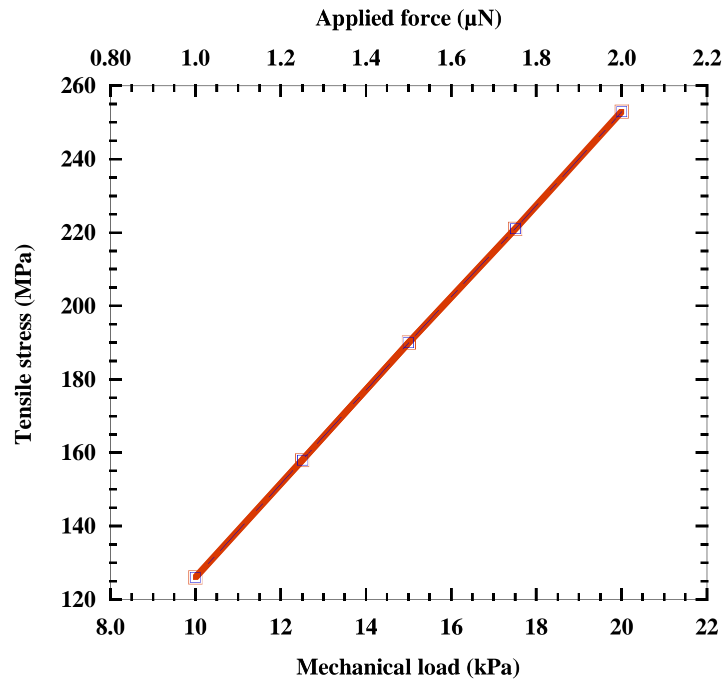

Figure 3.28 The simulated tensile stresses of the cantilever with respect to different applied load (AlN film thickness=300 nm).

well below than its ultimate tensile strength (i.e., 950 MPa ±150 MPa) [48,49]. Therefore, the stress analysis of the cantilever proves that even with 300 nm ultrathin AlN film, the device is highly reliable as far as its mechanical durability is concerned. Figure 3.28 shows tensile stress of the cantilever at different applied load.

3.6.2 AlN as a flexible material

Flexibility of any particular film can be determined by the values of its thickness, maximum tensile/compressive stress and bending radius of curvature. The thinner the film, the more flexible it becomes. Also, it is necessary to keep Von Mises stress of the material below its yield strength/tensile strength. To analyze the flexibility, stress analysis for AlN film was carried out by keeping the maximum deflection i.e., 2.23 μm fixed but changing its thickness on CoventorWare®. The maximum von Mises stress for both the

Ti films i.e., top and bottom electrodes, of the cantilever were compared with the yield strength of the material. Similarly, tensile stress and compressive stress of the AlN film were also compared against the tensile strength and compressive strength of AlN by changing its thickness. The results are shown on Figure 3.29, Figure 3.30, and Figure 3.31. Table 3.11 shows the comparison between the films ultimate strength versus simulated maximum stress. It is observed that maximum stresses of both AlN and Ti films in the cantilever are well below compared to their reported yield/tensile strength/compressive strength while changing AlN film thickness and are flexible enough to withstand upon applying of considerable amount of force until it reaches its maximum displacement.

The Mises stress of the cantilever increases linearly with respect to the increment of the AlN film thickness and the stress analysis not only validates the feasibility of the thickness applied in the fabrication of AlN film i.e., 300 nm but also promises about other thicknesses those can be applied to make AlN based flexible micro-sensors in future.

Bending radius of curvature was calculated for the cantilever assuming the height to be 2.23 μm and length to be 120 μm of the curvature. R S. Dahiya *et al.* [50] discussed about the flexibility of ultra-thin silicon chips where the mentioned bending radius of curvature were 6 mm for 44 μm and 4.1 mm for 24 μm thick Si substrate. H. Dong *et al.* [51] discussed about ROC i.e., 1.5 mm for microcrystalline silicon top-gate thin-film transistor and L. Wang *et al.* [52] reported of 1 mm ROC for 0.5 μm thick ultrathin Si substrate. Flexible AlN based sensors were reported as well for different thicknesses [53,54]. But, none of the papers really discussed about the bending radius of curvature which is one of the defining parameters for flexibility of a material. In this work, the calculated radius of arc was found to be 0.8 mm and the angle subtended by arc was 9°.

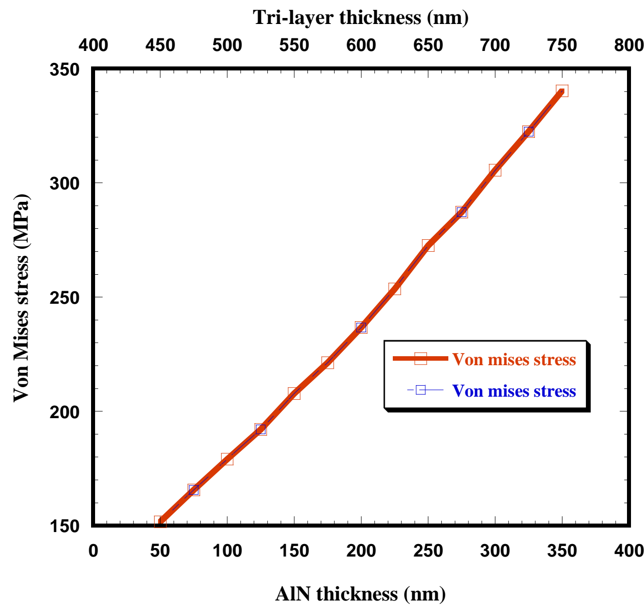

Figure 3.29 Simulated stress analyses for Titanium (Ti) films as top and bottom electrodes with respect to various thicknesses of AlN film while keeping the cantilever maximum displacement fixed to 2.23 µm.

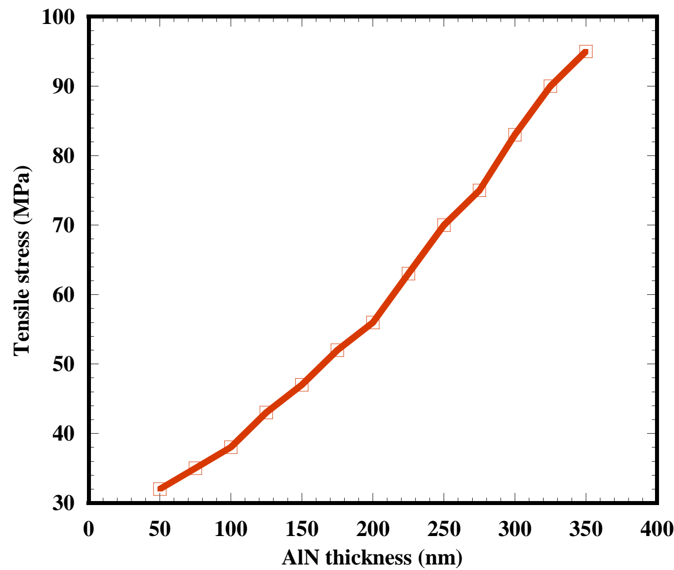

Figure 3.30 Simulated tensile stress analyses for AlN film with respect to change its thickness while keeping the cantilever maximum displacement fixed to 2.23 µm.

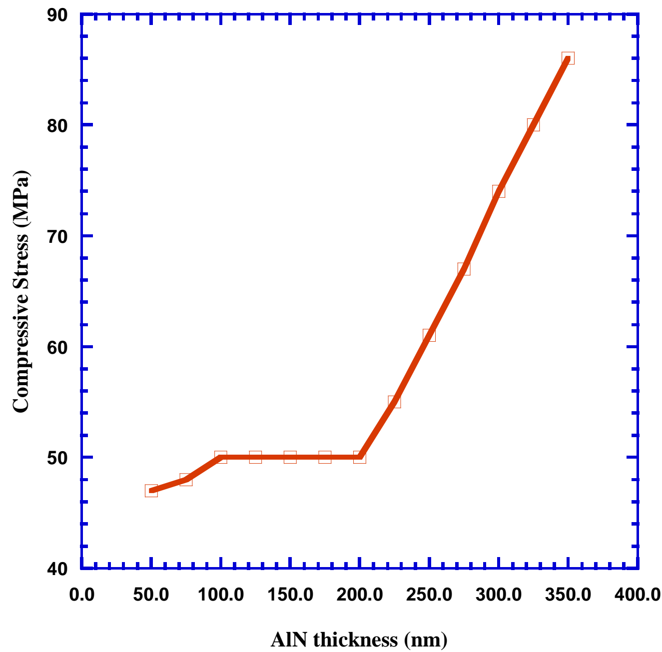

Figure 3.31 Simulated compressive stress analysis for AlN film with respect to change its thickness while keeping the cantilever maximum displacement fixed to 2.23 μm.

Table 3.11 Simulated stress analysis varying AlN film thickness

AlN film thickness (nm)	Tensile Stress of AlN (MPa)	Tensile strength of AlN (MPa)	Compressive stress of AlN (MPa)	Compressive strength of AlN (GPa)	Von Mises stress of Ti (MPa)	Yield strength of Ti (MPa)
50	32	340 [46]	47	1.5-4.0 [47]	151.647	950 ±150 [48,49]
75	35		48		165.636	
100	38		50		179.129	
125	43		50		192.139	
150	47		50		207.833	
175	52		50		221.219	
200	56		50		236.734	
225	63		55		253.602	
250	70		61		272.549	
275	75		67		287.29	
300	83		74		305.502	
325	90		80		322.423	
350	95		86		340.352	

3.7 Conclusions

3.7.1 Discussions

The fabrication, characterization and modeling of piezoelectric, ultra-thin (~300 nm) aluminum nitride (AlN) cantilevers are reported. The novel flexible, ultra-thin film AlN provides excellent compatibility for flexible sensors. The tri-layer cantilevers were fabricated with the AlN layer sandwiched between two titanium layers. Low deposition temperature (300 ^oC) was maintained to deposit AlN for superior CMOS and flexible substrate compatibility. The characterization and the numerical modeling of AlN cantilevers were performed to find the output voltage (both experimentally and numerically) and the piezoelectric response. Multiple cantilever sensors were characterized after fabrication at various loading frequency and a range of output voltage was measured. The measured voltages ranged from 4.48×10^{-4} V to 5.66×10^{-6} V. CoventorWare® software was used for simulation and modeling of the cantilevers to find output voltage as well as force response. The simulated results for output voltages ranged from 1.16×10^{-4} V to 4.16×10^{-5} V. Force response was found to be between 66.5 V/N to 41.2 V/N. The power spectral density and the Johnson noise floor were also characterized. Noise equivalent force (NEF) can also be calculated using the characterized and simulated results.

$$Noise\ equivalent\ force\ (NEF) = \frac{Johnson\ noise\ voltage}{Piezoelectric\ response}$$

Calculated Johnson noise voltage was found to be 1.28×10^{-6} V/√Hz. The calculated average piezoelectric response from the numerical modeling was 53.85 V/N. Therefore, the noise equivalent force is calculated to be 2.38×10^{-8} N/√Hz. From the results measured in the experiment and calculated in the numerical modeling, it is observed that the calculated output voltages deviate from the experiential voltages. There

could be several reasons. One possible reason for this to happen could be the negligence of the resistive loss through the coaxial cable. Resistive loss must have happened while the signal is carried from the bond pad of the cantilever to the low noise amplifier and then dynamic signal analyzer through the coaxial cables. Also, sometimes insufficient bending of the cantilever under applied stress could be an issue for the deviation between the two (experimental and numerical analyses) results. However, the responses of the cantilevers in the characterization at different low frequencies prove that the AlN cantilevers were fabricated successfully. The SEM, EDAX and XRD images show the quality of the AlN thin film. As far as the characterization is concerned, the cantilevers were operated at low frequencies since at relatively higher frequency (> 5 Hz), the cantilevers got broken. In future work, AlN film with much lower thickness i.e., 50 nm~300 nm will be the target thickness for the deposition of piezoelectric material for MEMS sensors to increase the flexibility of the sensors.

3.7.2 Future work

The motivation of my PhD work was based on ultra-thin film AlN cantilever structure which apparently forms the basis for future flexible force/pressure sensors, accelerometers, pressure sensors, fingerprint sensors, and so on. Therefore, the next goal will be to design various types of sensors for MEMS applications using ultrathin AlN films as sensing element that include high resolution MEMS fingerprint sensors and MEMS accelerometer.

Chapter 4

Ultrathin AlN based Fingerprint Sensors for High Resolution Fingerprint Detection

4.1 Introduction

In this modern world with so much advancement in technology one must be aware of his personal data security which can be hacked easily nowadays. Since most of the financial and nonfinancial activities (e.g., online banking, email etc.) are now mostly processed in personal laptops, smartphones, tablets, and so on, it is, therefore, a matter of concern to protect those data from hacking by hackers out there.

With the ever increasing need of security for personal/public data from data theft, biometric identification has grown as a viable solution in recent times in recognizing people and rejecting false match. In biometrics, biological characteristics are utilized for identification or verification purpose of an individual. The focus of the biometric systems is to improve the quality of personal identification in an automated manner. There are some criteria that need to be considered in biometric systems:

1. The biometric sensor should be able to collect meaningful data in various conditions that include different users and diverse environmental conditions in which the measurements are operated.
2. The biometric system should be able to differentiate between an artificial skin and human skin so that the identification is not compromised.

There are two types of biometric systems. They are: a) behavioral biometrics and b) physical biometrics. Behavioral biometrics includes typing recognition and speaker identification whereas physical biometrics includes fingerprint identification, voice authentication, hand or finger geometry recognition, and facial recognition.

Among the techniques, fingerprint sensing is one of the most reliable and widely utilized techniques for personal authentication. This type of identification involves

comparing between two scanned fingerprints for identification. Each finger surface has ridges (raised) and valleys (recessed) which defines the fingerprint [55]. A fingerprint pattern consists of arch, loop, and whorl which are nothing but parts of ridges. When a fingerprint is scanned ridges only make contact with surface of the scanner/sensor, valleys do not make any contact thus do not take part directly in creating fingerprint pattern. Therefore, fingerprint information that is stored in a database is basically the information of the location of ridges of a finger surface. A sample fingerprint of a person is compared to the information of previously stored fingerprints in a database for matching in order to verify the person.

A fingerprint sensor can be made of hundreds or thousands of pixels. Again each pixel can have a sensing element. The sensing element can be of capacitive, piezoelectric, and piezo-resistive. AlN being the sensing element of a fingerprint sensor can offer high sensitivity and flexibility. In this chapter, design of three different fingerprint sensors with a resolution of 725 dpi and a resolution of 1016 dpi will be discussed.

4.1.1 Background and motivation

Biometrics such as fingerprint sensing techniques has become popular over the past few years. The reason is because it provides the one of the best security options for any personal identification devices. The conventional techniques such as passwords and personal identification numbers (PINs) are becoming obsolete and gradually being replaced by biometric identification such as fingerprint because it serves better security and safety measures than the conventional techniques. Among the various existing identification system for fingerprint identification system the following have been studied by many researchers. They are: i) optical, ii) capacitive, iii) RF field-AC capacitive, iv) piezoresistive, v) thermal, vi) tactile, vii) ultrasound, viii) touchless, and ix) piezoelectric.

Among the mentioned above, optical fingerprint sensors have been broadly and extensively used [56,57,58]. But like many other conventional imaging techniques, it possesses some disadvantages too. For example, poor images may occur with optical fingerprint sensor from conditions like dry skin, bad surface feature of the finger, poor contact between the sensor and the fingertip, vivid ambient light, and surface moisture. In 2001, N. Sato *et al.* [55] brought a discussion about capacitive MEMS fingerprint sensor with arrayed cavity structures. Each cavity structure was nothing but a pixel. The pixel had a dimension of 50 μm by 50 μm and a resolution of 508 dpi. They mainly investigated the mechanical strength of the sensor by tapping tests and discussed the fabrication process of the MEMS fingerprint sensor. In 2004, B. Charlot *et al.* [59] first reported about a sweeping mode integrated fingerprint sensor. The sensor consisted of 256 pressure sensitive microbeams and was completely integrated with analog and mixed signal electronics. The advantage with this type of sensor was that it required smaller surface area for scanning which minimized the cost, however, it created problems too on the measurements when the finger speed was not constant on the microbeams. In 2009, M. Damghanian and B. Y. Majlish reported the design and modeling of a pressure sensitive capacitive MEMS fingerprint sensor where a wide micro beam was used as a pressure gauge for the fingerprint sensors [60]. They investigated on the improvement of sensitivity of MEMS fingerprint by using wide microbeam instead of using common membrane based structure to gauge capacitive changes which is induced due to applied pressure. They claimed that the designed sensor could improve sensitivity up to 5 times compared to other membrane based structure for fingerprint sensing. In 2011, J. -C. Liu *et al.* [61] reported about a capacitive sensor array for fingerprint sensing using CMOS micromachining technique. In their approach, they used array of circular membrane structures or pixels for measurement of capacitive changes while fingerprint scanning.

The pixel size was 65 μm by 65 μm and equivalent to a resolution of 390 dpi. In 2013, B. A. Ganji *et al.* [62] reported about a MEMS capacitive fingerprint sensor using slotted membrane for high sensitivity. The slotted membrane helped reduce the air damping, especially, squeeze film damping and improved sensitivity. The fingerprint sensor was made of array slotted membrane structure which had a dimension of 50 μm by 50 μm and a resolution of 508 dpi but with improved sensitivity unlike previous capacitive fingerprint sensors. In 2015, H. Tang *et al.* [63] discussed about an ultrasonic fingerprint sensor using pulse-echo imaging technique where the authors reported the first implementation of a fully integrated thin AlN based pulse-echo ultrasonic fingerprint sensor by bonding MEMS and CMOS wafers to attain compact size, low power consumption and fast response. The sensor had a pitch of 100 μm and was equivalent to a resolution of 254 dpi. In 2015, S. –M. Huang *et al.* [64] designed and modeled a-Si TFT based 1000 ppi fingerprint sensor. The model showed that it can improve sensor sensitivity and signal-to-noise ratio remarkably.

Each type of fingerprint sensor follows unique technology. For example, the operation mechanism for optical fingerprint sensor is something that a reflected optical image of a fingerprint is detected once a finger is scanned. However, the optical system requires some optical apparatus such as lenses, an illumination source, and an imaging camera to capture quality images but it eventually increases the overall cost for a fingerprint scanner. Moreover, it requires some other maintenance costs for the mechanical parts [65]. All other fingerprint sensors such as capacitive fingerprint sensor and TFT sensor are used in great scale in many big companies like Apple, Sony, and Fujitsu. However, they have the cost issues too since the fingerprint sensors need larger area to produce accurate imaging information from the fingerprint. Nowadays, 600 dpi (i.e., 23 pixels/mm) capacitive sensors have become popular in the market with average

pitch size of 42 µm. Recent study shows that 582 dpi 3D piezoelectric micromachined ultrasonic transducers (PMUTs) with a pitch of 43 µm can be a good improvement in fingerprint scanning [66].

We propose three AlN based piezoelectric fingerprint sensor with a pitch of 35 µm and 25 µm and a resolution of approximately 725 dpi and 1016 dpi. The goal toward this work is to improve image resolution and sensitivity of fingerprint detection by reducing the pitch of the pixels. To make that happen, ultrathin AlN film can be used as the sensing element which provides excellent sensitivity, high flexibility and CMOS compatibility for piezoelectric material. Al_2O_3 cavity structure was used as the pixel membrane which offers good mechanical stability as well as transparency. The high resolution fingerprint sensors will also enable detection of unique dimples in the finger ridges for additional biometric measures to get more accurate and more secure personal identification. This chapter will present the basic design, simulation and modeling of the pixel of three different fingerprint sensors. The responses of the sensors are also calculated. A thin protective polymer layer will be put on top surface of the pixels of the fingerprint sensors for practical use. But, for the scope of the work, this section is avoided here.

4.2 Design and Simulation

4.2.1 725 dpi fingerprint sensor (FPS725A)

We propose a 725 dpi fingerprint sensor which is designed using FEA software CoventorWare® and named as FPS725A. The pitch or the distance between two pixels is 35 µm. Using the 'process editor' tool in CoventorWare® the design steps and layer names including their thickness are mentioned. A silicon_100 wafer is chosen for substrate material. Then, a silicon nitride (Si_3N_4) layer is chosen as the passivation layer. 1 µm thick Si_3N_4 is deposited on top of the Si substrate. After that, a 4 µm thick polyimide

is used as the sacrificial layer. Aluminum oxide (Al_2O_3) is used to form a cavity like structure which includes 1.8 μm thick Al_2O_3 membrane structure and 2.5 μm thick walls of Al_2O_3 at the boundary that are shared between the pixels. Titanium (Ti) is used as top and bottom electrode layer whereas AlN is used as the piezoelectric layer in the 'process editor' and sandwiched between two electrodes. The electrodes (Top and bottom) are 0.1 μm each in thickness and the AlN layer is 0.2 μm thick. A liftoff process is used to pattern the trilayer stack Ti/AlN/Ti. To remove the sacrificial layer in order to form the cavity structure, holes are etched through the Al_2O_3 membrane. The process editor steps are shown in Figure 4.1. Then, a 2D layout is drawn and used to build a solid model (Figure 4.2). The 3D solid model of the pixel is built using CoventorWare® preprocessor with the help of layout editor and process editor. Figure 4.3 show the process flow of the 3D solid model of the pixel. The step for removal of sacrificial layer is not shown in Figure 4.3. However, the solid model is meshed afterwards. Different regions are meshed differently. Before proceeding into mechanical simulation, mesh convergence is studied thoroughly. Once the mesh convergence is satisfied then all the mechanical analyses are carried out. Parametric mechanical analyses are carried out with respect to different loading conditions. Stress analyses in the AlN film are analyzed and normal stresses, for example, S_{xx}, S_{yy}, S_{zz} are used to calculate the surface charge densities of the film. The dimension of the pixel is shown in Figure 4.4 and Figure 4.5.

Lastly, piezoelectric output voltages and response are calculated using the voltage-charge relationship for a parallel plate capacitor. The results are discussed in Results and Discussion section of this chapter. Figure 4.6 shows the labeling for different layers of the pixel.

Process editor

Number	Step Name	Layer Name	Material Name	Thickness	Mask Name	Photoresist	Depth	Mask Offset	Sidewall Angle	Comments
0	Substrate	Substrate	SILICON_100	10	SubstrateMask					
1	Planar Fill	passivation	SI3N4	1						
2	Stack Material	sacrificial	POLYIMIDE	4						
3	Straight Cut				polyimide	+		0	0	
4	Conformal Shell	Al2O3	AL2O3	4						
5	Straight Cut				Al2O3	+		0	0	
6	Straight Cut				Al2O3_depth_reduction	-	2.2	0	0	
7	Straight Cut				hole_for_sacrificial	-		0	0	
8	Delete	sacrificial								
9	Stack Material	bot	TITANIUM	0.1						
10	Straight Cut				bot	+		0	0	
11	Stack Material	piezo	AlN	0.2						
12	Straight Cut				piezo	+		0	0	
13	Stack Material	top	TITANIUM	0.1						
14	Straight Cut				top	+		0	0	

Figure 4.1 Process Editor

2D layout

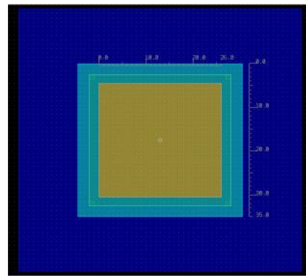

Figure 4.2 2D layout

Design process flow

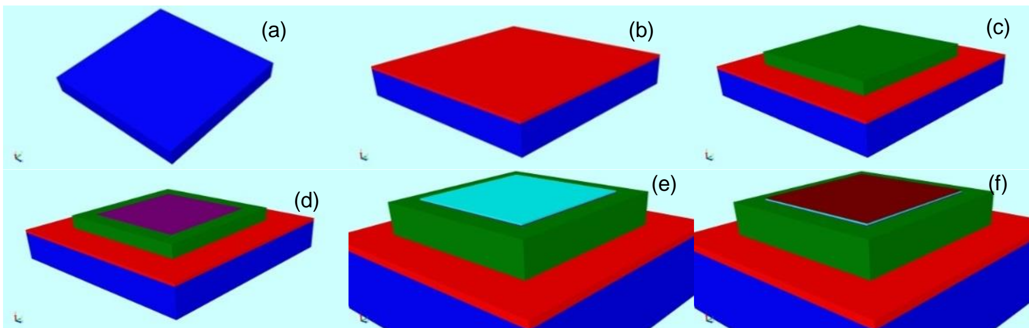

Figure 4.3 Process flow of the pixel design in preprocessor (a) Si Substrate (b) deposition and pattern of passivation (Si_3N_4) layer (c) deposition and pattern of polyimide layer (d), (e), and (f) deposition and trilayer liftoff of bottom electrode (Ti), piezoelectric (AlN) layer , and top electrode (Ti).

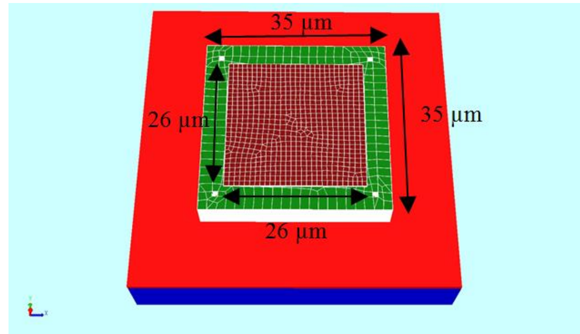

Figure 4.4 3D solid meshed model of a pixel of the sensor. Dimension of Al_2O_3 membrane: 35 µm×35 µm; AlN and Ti: 26 µm×26 µm.

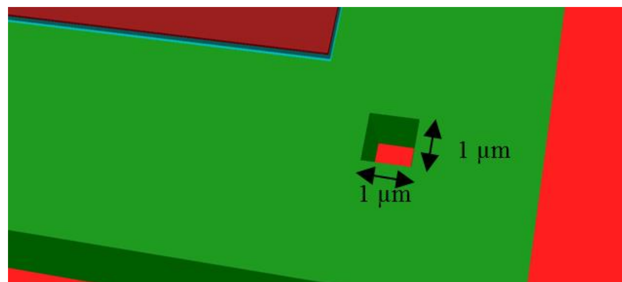

Figure 4.5 Dimension of the hole is shown. Holes are used to remove the sacrificial layer (i.e., polyimide) and form a cavity like structure.

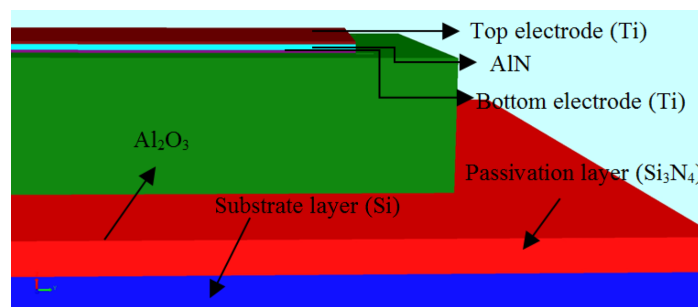

Figure 4.6 Labeled layers of a pixel (partial).

Mesh Convergence

Mesh study is shown for this design in the following table. After the coarse mesh, finer mesh is done in Al_2O_3 membrane structure for mesh convergence. For all the materials, extruded brick mesh type is chosen. For both electrodes, extruded bricks mesh

type is used where 1 μm×1 μm brick is chosen in planer direction and 0.01 μm thickness is chosen in extruded or z-direction. As of AlN layer, a 0.5 μm×0.5 μm brick size is chosen in planer direction and a 0.01 μm thickness is chosen in extruded direction. And, for Al_2O_3, a 1.75 μm×1.75 μm brick size is chosen in planer direction and a 0.05 μm thickness is chosen for z-direction. It is found that change in mesh size in AlN and Ti layers do not affect much in mesh convergence. Figure 4.7 and Figure 4.8 shows the convergence of the mesh study which shows the variation in stress with the change of Al_2O_3 mesh size in planer direction (i.e., x and y direction). Table 4.1 shows the mesh conditions for different layers for mesh to converge.

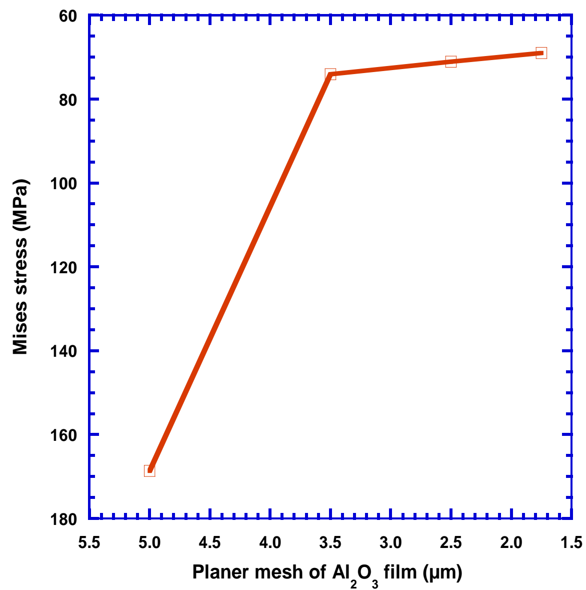

Figure 4.7 Simulated maximum Mises stress of Al_2O_3 film with respect to different planer mesh size of Al_2O_3 membrane layer (Mesh convergence study).

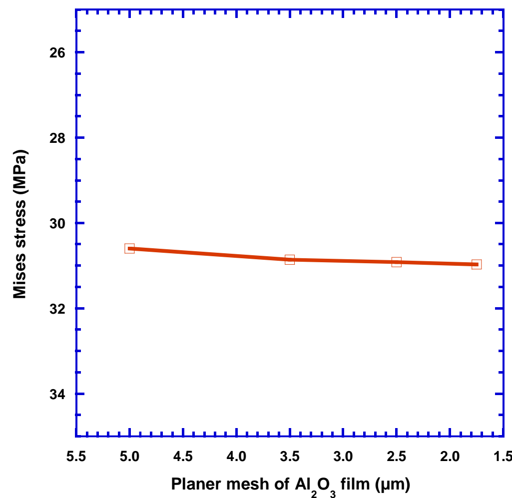

Figure 4.8 Simulated maximum Mises stress of AlN film with respect to different planer mesh size of Al_2O_3 membrane layer (Mesh convergence study).

Table 4.1 Mesh conditions for different layers in CoventorWare®

Layer Name	Material	Mesh Type	Mesh Size (μm)
Bottom electrode	Ti	Extruded bricks	Planer direction (x, y) =(1,1), Extruded direction, z =0.01
Piezoelectric layer	AlN	Extruded bricks	Planer direction (x, y) =(0.5,0.5), Extruded direction, z =0.01
Top electrode	Ti	Extruded bricks	Planer direction (x, y) =(1,1), Extruded direction, z =0.01
Cavity/Membrane structure	Al_2O_3	Extruded bricks	Planer direction (x, y) =(1.75,1.75), Extruded direction, z =0.05

4.2.2 725 dpi fingerprint sensor (FPS725B)

The design process flow of this sensor is pretty similar to FPS725A discussed in section 4.2.1 except that the trilayer Ti/AlN/Ti are deposited underneath the Al_2O_3 membrane structure. Two metallization layers are used for proper wiring and to carry the electrical signal from the electrodes to the CMOS circuit. The design is completed step by step in process editor, 2D layout and preprocessor in CoventorWare®. Same materials are used for FPS725B as FPS725A. In addition to that, aluminum is used for metallization layers. The layer names and material thicknesses are shown in Figure 4.9.

Figure 4.10 shows the 2D layout of the fingerprint sensor. Figure 4.11 shows step by step 3D solid model design flow. For mesh analysis, mesh sizes are mostly kept same as in section 4.2.1. Table 4.2 shows the mesh study for this design. Mechanical analysis for stress analysis and other analysis are done in similar way as those were done for FPS725A. Figure 4.12 shows the top and bottom view of the fingerprint sensor along with the meshed model.

Process editor

Number	Step Name	Layer Name	Material Name	Thickness	Mask Name	Photoresist	Depth	Mask Offset	Sidewall Angle	Comments
0	Substrate	Substrate	SILICON_100	5	SubstrateMask					
1	Planar Fill	passivation	SI3N4	1						
2	Straight Cut				Passivation_etch	-		0	0	
3	Planar Fill	contact	GOLD	0.2						
4	Straight Cut				contact_pattern	+		0	0	
5	Planar Fill	sacrifical	POLYIMIDE	4						
6	Straight Cut				polyimide	+		0	0	
7	Conformal Shell	lower_level_Wiring	ALUMINUM	0.05						
8	Straight Cut				lower_level_wirirng	+		0	0	
9	Conformal Shell	bot	TITANIUM	0.1						
10	Straight Cut				bot	+		0	0	
11	Conformal Shell	piezo	AlN	0.2						
12	Straight Cut				piezo	+		0	0	
13	Conformal Shell	top	TITANIUM	0.1						
14	Straight Cut				top	+		0	0	
15	Conformal Shell	insulation_layer	AL2O3	0.1						
16	Straight Cut				insulation	+		0	0	
17	Straight Cut				window_for_upper_wiring	-		0	0	
18	Conformal Shell	upper_level_wiring	ALUMINUM	0.05						
19	Straight Cut				upper_level_wiring	+		0	0	
20	Conformal Shell	Al2O3	AL2O3	4						
21	Straight Cut				Al2O3	+		0	0	
22	Straight Cut				Al2O3_depth_reduction	-	2.75	0	0	
23	Straight Cut				hole_for_sacrificial	-		0	0	
24	Delete	sacrifical								

Figure 4.9 Process Editor

2D layout

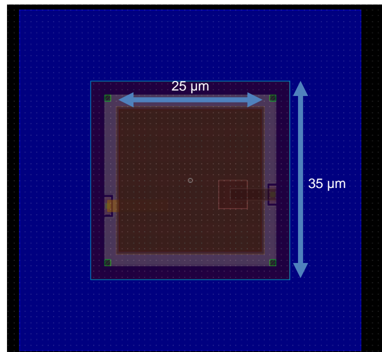

Figure 4.10 2D layout including the dimension. Dimension of Al_2O_3 based membrane: 35 µm×35 µm; AlN and Ti: 25 µm×25 µm.

Design process flow

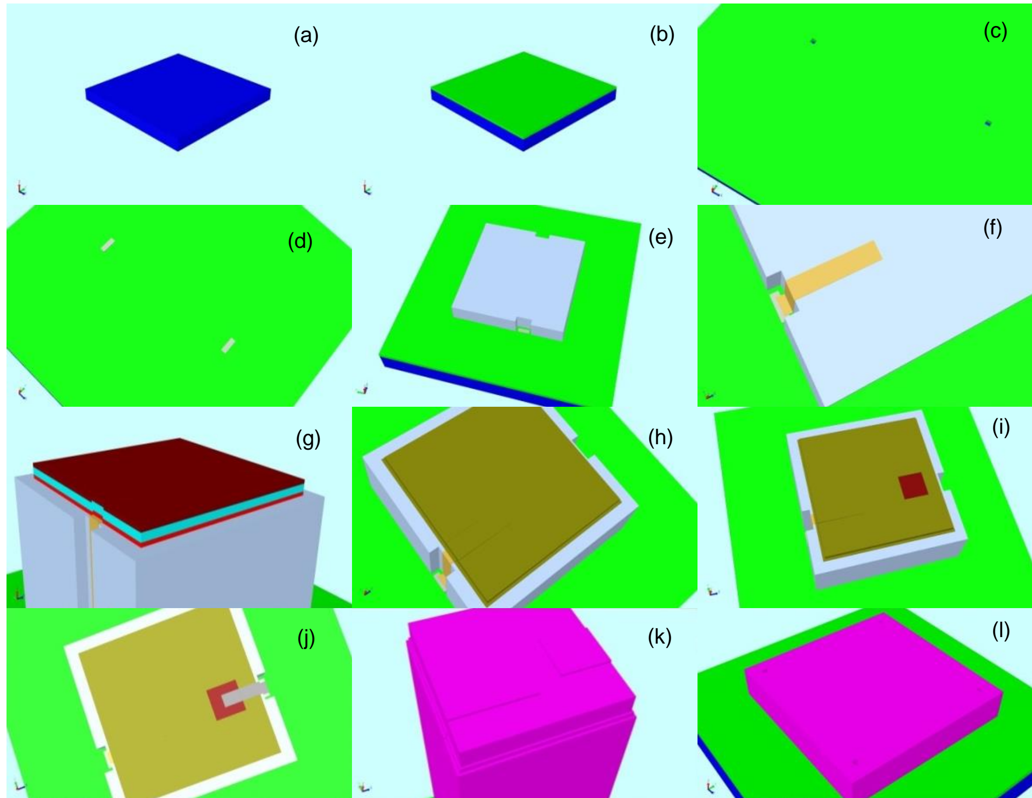

Figure 4.11 3D Process flow of the 35 μm×35 μm pixel design in preprocessor (FPS725B) (a) Silicon substrate layer (b) deposition of passivation (Si_3N_4) layer (c) etching of hole in the passivation layer for contact pad (d) lift off of contact pad (e) deposition and pattern of polyimide layer (f) 1st level of metallization for bottom electrical connection using lift off technique (g) trilayer deposition Ti/AlN/Ti stack and simultaneous lift off pattern (h) deposition of an insulation layer to provide side wall insulation to prevent electrical short between top and bottom electrode (i) etching a window on the insulation layer for electrical connect (j) 2nd level of metallization for top electrical connection (k) deposition of Al_2O_3 all over the area to form the cavity structure (membrane+side walls) (l) top surface planarization and pattern of Al_2O_3 cavity structure including the etching hole to remove the sacrificial polyimide layer.

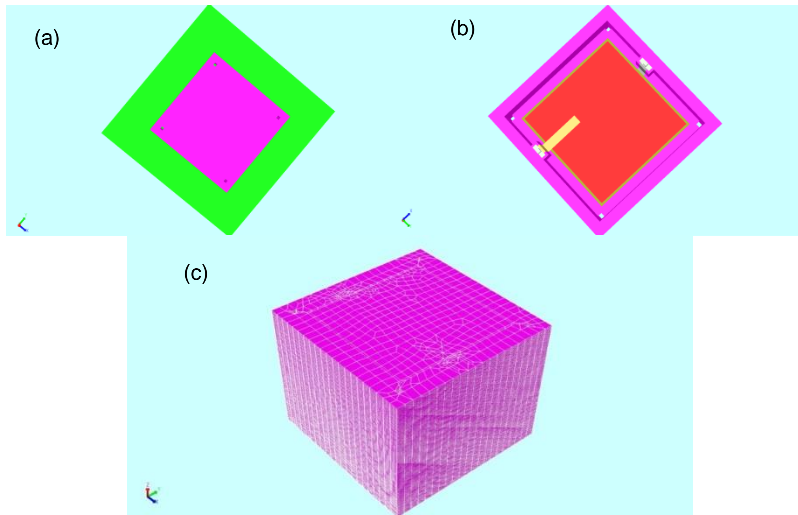

Figure 4.12 (a) top view of the final structure of the pixel (b) bottom view of the final structure of the pixel (c) meshed model of the pixel.

In the fabrication process, 1 µm thick silicon nitride (Si_3N_4) was sputtered on top of silicon substrate as a passivation layer. Next, after that, passivation layer was etched to make holes so that electrical connection can be achieved through passivation layer for CMOS read out and external signal conditioning circuit. Then, metal contact, for example, gold (Au) was deposited using lift-off technique to form contact pads for top and bottom electrodes of the sensor. Then, a 4 µm polyimide layer was spin coated, patterned by photolithography, and annealed. Once the polyimide layer was patterned, 1st electrical metallization pattern was carried out using Aluminum (Al) for electrical connection from bottom electrode. Lift-off technique was used to pattern the Al layer. Next, a trilayer lift off was simultaneously for bottom electrode [Titanium (Ti)], piezoelectric layer (AlN), and top electrode (Ti). In the next step, 2nd metallization layer was completed for electrical connection from top electrode. Before the 2nd metallization layer, an insulation layer of Al_2O_3 was deposited and pattered to prevent any electrical short between top and bottom electrode. The metallization layers were extended to contact pads for CMOS read out.

After that, Al_2O_3 was sputtered everywhere uniformly. The top surface of the Al_2O_3 was planarized afterwards such as way so that a thickness of 1.8 µm achieved for the membrane part of Al_2O_3 based structure. After that, 4 holes of 1 µm×1 µm dimension were etched on top of the Al_2O_3 structure. Finally, polyimide layer was completely removed by O_2 plasma ashing to form a cavity or diaphragm like structure of Al_2O_3 with boundary walls and membrane which was termed as a “pixel” of the fingerprint sensor.

Mesh Convergence

Table 4.2 Mesh for different layers

Layer Name	Material	Mesh Type	Mesh Size (µm)
Metal wiring for bottom electrode	Al	Extruded bricks	Planer direction (x, y)=(1,1), Extruded direction, z=0.01
Bottom electrode	Ti	Extruded bricks	Planer direction (x, y) =(1,1), Extruded direction, z =0.01
Piezoelectric layer	AlN	Extruded bricks	Planer direction (x, y) =(0.5,0.5), Extruded direction, z =0.01
Top electrode	Ti	Extruded bricks	Planer direction (x, y) =(1,1), Extruded direction, z =0.01
Insulation layer	Al_2O_3	Extruded bricks	Planer direction (x, y) =(1,1), Extruded direction, z =0.01
Metal wiring for top electrode	Al	Extruded bricks	Planer direction (x, y) =(1,1), Extruded direction, z =0.01
Cavity/Membrane structure	Al_2O_3	Extruded bricks	Planer direction (x, y) =(1.75,1.75), Extruded direction, z =0.05

4.2.3 1016 dpi fingerprint sensor (FPS1016)

Process editor

The process editor for 1016 dpi fingerprint sensor (FPS1016) is exactly same as the 725 dpi fingerprint sensor with FPS725B. Therefore, the process editor steps are skipped in this section. Figure 4.13 and Figure 4.14 show the 2D layout and the solid model, respectively. Table 4.3 show the mesh study of different layers of the pixel. 3D solid model process flow is also exactly same as Figure 4.11. Therefore, the step by step description is avoided in Figure 4.14.

2D layout

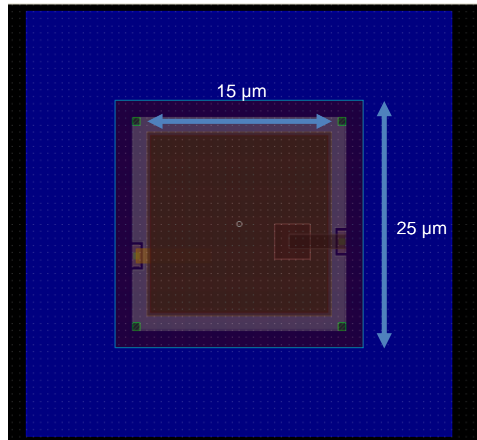

Figure 4.13 2D layout including the dimension. Dimension of Al_2O_3 membrane: 25 µm×25 µm; AlN and Ti: 15 µm×15 µm.

Design process flow

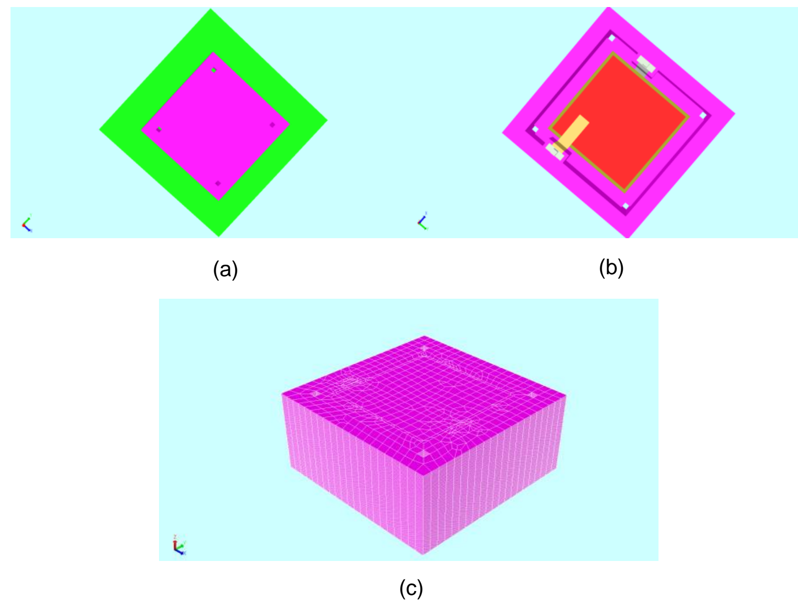

Figure 4.14 Design of 25 µm×25 µm pixel in preprocessor (FPS1016) (a) top view of the final structure of the pixel (b) bottom view of the final structure of the pixel (c) meshed model of the pixel.

Mesh Convergence

Table 4.3 Mesh for different layers

Layer Name	Material	Mesh Type	Mesh Size (μm)
Metal wiring for bottom electrode	Al	Extruded bricks	Planer direction (x, y)=(1,1), Extruded direction, z=0.01
Bottom electrode	Ti	Extruded bricks	Planer direction (x, y) =(1,1), Extruded direction, z =0.01
Piezoelectric layer	AlN	Extruded bricks	Planer direction (x, y) =(0.5,0.5), Extruded direction, z =0.01
Top electrode	Ti	Extruded bricks	Planer direction (x, y) =(1,1), Extruded direction, z =0.01
Insulation layer	Al_2O_3	Extruded bricks	Planer direction (x, y) =(1,1), Extruded direction, z =0.01
Metal wiring for top electrode	Al	Extruded bricks	Planer direction (x, y) =(1,1), Extruded direction, z =0.01
Cavity/Membrane structure	Al_2O_3	Extruded bricks	Planer direction (x, y) =(1.25,1.25), Extruded direction, z =0.05

4.3 Results and discussion

4.3.1 725 dpi fingerprint sensor (FPS725A)

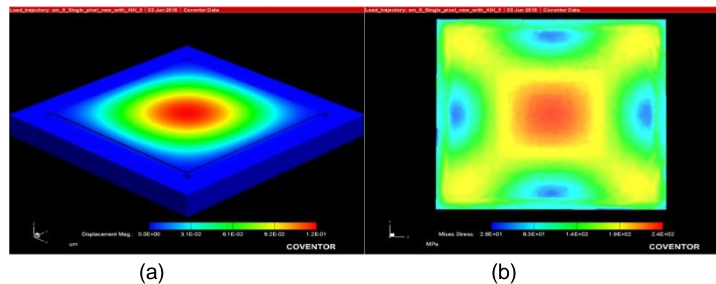

(a) (b)

Figure 4.15 (a) Displacement contour of a pixel and (b) Mises stress contour in the piezoelectric AlN layer from CoventorWare® simulation.

Stress analysis For understanding of the reliability or mechanical strength of a sensor, Mises stress is an important parameter to look into. In this case, the maximum Mises stress of each layer/material is compared with its corresponding ultimate tensile strength and compressive strength. The tensile strength and compressive strength for AlN and Ti are discussed in many literatures [46,47,49] and are found to be noticeably higher than the simulated maximum Mises stresses. Figure 4.16 shows the linear change of the Mises stresses of the materials with respect to different pressure or finger

pressure. For Al_2O_3, the maximum tensile stress and compressive stress are found from the stress contour and also compared with its corresponding strengths. The tensile strength of Al_2O_3 varies from 350 MPa~588 MPa [67]. It is evident that the tensile strength of Al_2O_3 is at least 5 times higher than the maximum Mises stress of Al_2O_3 found from the simulation when a load or finger pressure of 1 MPa (Figure 4.15) is applied. Similar comparison goes with the compressive stress. The value is much lower than the compressive strength of Al_2O_3 which ranges between 0.69 GPa ~5.5 GPa [67]. The maximum load applied during the simulation process is 1 MPa. It has been reported in the literature that the upper limit of the finger pressure in practical use is 0.6 MPa; hence, the maximum loading of 1 MPa for simulation purpose is justified. However, Mises stress of the sensor or in the pixel at 0.6 MPa finger pressure is 41.41 MPa which show sufficient proof of mechanical reliability of the sensor as far as the mechanical strength is concerned. In other way, the results show that the sensor is stable enough to withstand any range of typical finger pressure under this circumstance.

Spring constant Spring constant of the pixel is also calculated from the force-displacement relationship. Figure 4.17 shows the simulated spring constant of the pixel.

Table 4.4 Simulated stress analysis of the sensor (FPS725A)

Applied Load (MPa)	Applied force (N)	Maximum Mises stress of the sensor (MPa)	Mises stress (Al_2O_3) (MPa)	Mises stress (AlN (MPa)	Mises stress (Ti) (MPa)
0.1	6.76E-05	6.90	6.90	3.11	3.082
0.2	1.35E-04	13.80	13.80	6.22	6.164
0.3	2.03E-04	20.70	20.70	9.33	9.246
0.4	2.70E-04	27.60	27.60	12.44	12.328
0.5	3.38E-04	34.51	34.51	15.55	15.410
0.6	4.06E-04	41.41	41.41	18.66	18.492
0.7	4.73E-04	48.31	48.31	21.77	21.574
0.8	5.41E-04	55.21	55.21	24.88	24.656
0.9	6.08E-04	62.11	62.11	27.99	27.738
1.0	6.76E-04	69.01	69.01	31.1	30.820

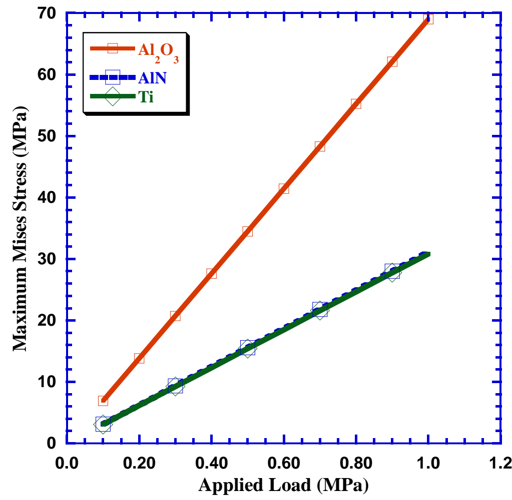

Figure 4.16 Simulation plot of maximum Mises stress of each layer with respect to different loads.

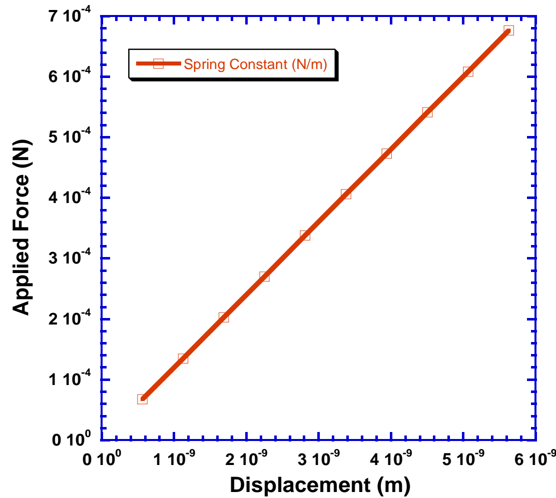

Figure 4.17 Simulation plot of spring Constant of the pixel of FPS725A.

Piezoelectric Voltage Response The response of the pixel is calculated using simulation results and is shown in Figure 4.18. Table 4.5 shows the calculated values of the open circuit piezoelectric output voltage (i.e., prior to including external CMOS circuits

in the system) with respect to various finger pressure. Applied pressures are converted to applied force to calculate the response in Table 4.5.

Table 4.5 Simulation and numerical modeling results for piezoelectric Response of the sensor (FPS725A)

Applied Load, P_L (MPa)	Applied Force, F (μN)	Charge Produced in the AlN film, Q (fC)	Capacitance, C (pF)	Piezoelectric Voltage, V (V)	Piezoelectric Response, R_F (V/N)
0.1	67.6	4.77	31.3	0.015	225.74
0.2	135	9.56	31.3	0.030	225.74
0.3	203	14.3	31.3	0.045	225.74
0.4	270	19.1	31.3	0.061	225.74
0.5	338	23.8	31.3	0.076	225.74
0.6	406	28.7	31.3	0.091	225.74
0.7	473	33.4	31.3	0.106	225.74
0.8	541	38.2	31.3	0.122	225.74
0.9	608	43.0	31.3	0.137	225.74
1.0	676	47.7	31.3	0.152	225.74

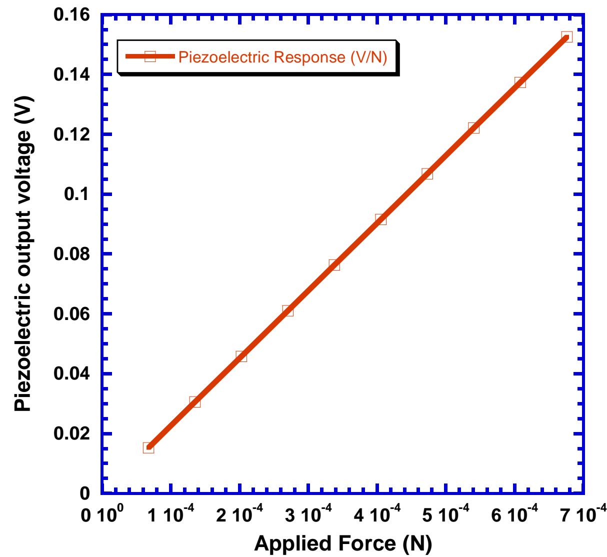

Figure 4.18 Simulation plot of piezoelectric output voltage of the sensor with respect to different loads mentioned in Table 4.5.

4.4.2 725 dpi fingerprint sensor (FPS725B)

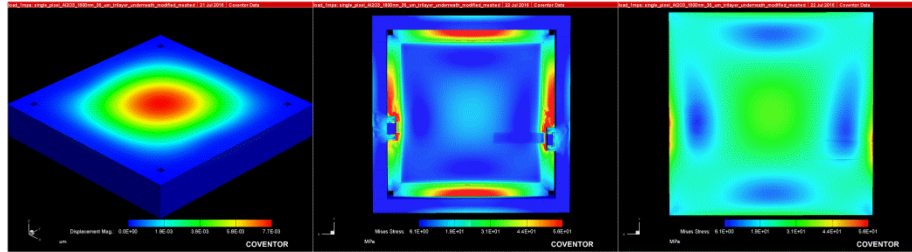

Figure 4.19 (a) Simulated displacement contour of a pixel and (b) simulated Mises stress contour of the pixel (bottom view) (c) Mises stress of AlN film from simulation.

Stress analysis The discussion of stress analysis for FPS725B is similar to what has been discussed for FPS725A. However, in this design, Aluminum (Al) was used as the material for metallization wiring. So, the yield strength or ultimate tensile strength of Al is also compared with the Maximum Mises stress value from the simulation to check mechanical stability of the pixel or/and the sensor. It is observed that the simulated maximum Mises stress value at 1 MPa loading condition is well below than its yield strength [68,69]. Also, the maximum Mises stress of Al_2O_3 i.e., 356.041 MPa is nothing but the compressive strength of the material. Therefore, it does not really affect the mechanical stability of the pixel since the compressive strength is very high for Al_2O_3 [67]. Table 4.6 and Figure 4.20 show the results of the stress analysis.

Table 4.6 Simulated stress analysis of the sensor (FPS725B)

Applied Load (MPa)	Applied force (μN)	Mises stress of Al_2O_3 (MPa)	Mises stress of AlN (MPa)	Mises stress of Ti (MPa)	Mises stress of Al (MPa)
0.1	122	35.649	5.612	5.663	18.793
0.2	244	71.298	11.225	11.326	37.586
0.3	366	106.947	16.837	16.989	56.379
0.4	488	142.596	22.450	22.652	75.172
0.5	611	178.245	28.063	28.315	93.965
0.6	733	213.894	33.675	33.979	112.758
0.7	855	249.543	39.288	39.642	131.551
0.8	977	285.192	44.901	45.305	150.344
0.9	1100	320.841	50.513	50.968	169.137
1.0	1220	356.490	56.126	56.631	187.930

Spring constant Spring constant of the pixel for FPS725B is calculated from the force-displacement relationship. Figure 4.21 shows the simulated spring constant of the pixel.

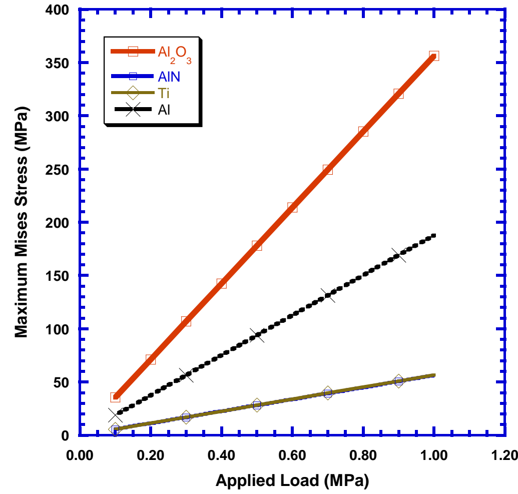

Figure 4.20 Simulation plot of maximum Mises stress of each layer with respect to different loads.

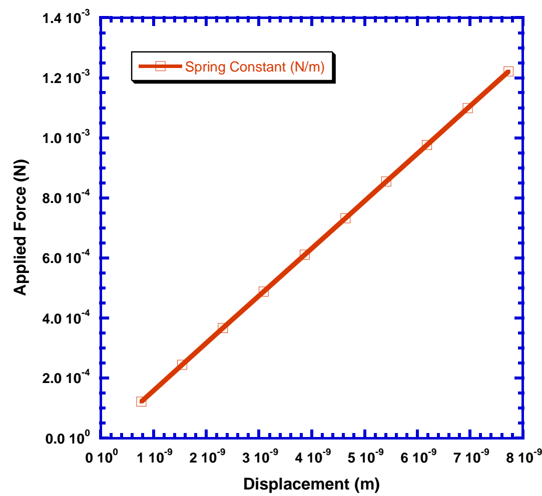

Figure 4.21 Simulation plot of spring Constant of FPS725B

Piezoelectric Voltage Response The response of the FPS725B is calculated using simulation results and is shown in Figure 4.22. Table 4.7 shows the calculated values of the open-circuit piezoelectric output voltage (i.e., prior to including external CMOS circuits in the system) with respect to various finger pressure. Applied pressures are converted to applied force to calculate the response in Table 4.7.

Table 4.7 Simulation and modeling results for piezoelectric Response of the 725 dpi (FPS725B) sensor

Applied Load, P_L (MPa)	Applied Force, F (μN)	Charge Produced in the AlN film, Q (fC)	Capacitance, C (pF)	Piezoelectric Voltage, V (V)	Piezoelectric Response, R_F (V/N)
0.1	122	4.16	295	0.014	115.58
0.2	244	8.31	295	0.028	115.58
0.3	366	12.5	295	0.042	115.58
0.4	488	16.6	295	0.056	115.58
0.5	611	20.8	295	0.071	115.58
0.6	733	24.9	295	0.085	115.58
0.7	855	29.1	295	0.099	115.58
0.8	977	33.3	295	0.113	115.58
0.9	1100	37.4	295	0.127	115.58
1.0	1220	41.6	295	0.141	115.58

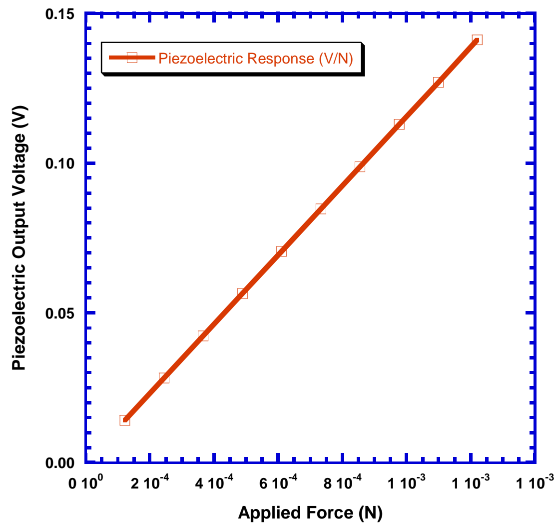

Figure 4.22 Simulation plot of piezoelectric output voltage of the sensor with respect to different loads mentioned in Table 4.7

4.4.3 1016 dpi fingerprint sensor (FPS1016)

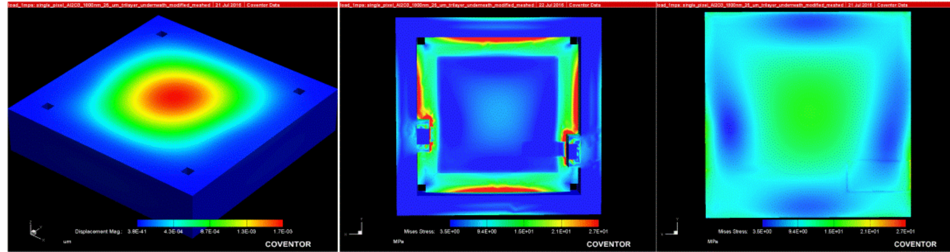

Figure 4.23 (a) Simulated displacement contour of a pixel and (b) simulated Mises stress contour of the pixel (bottom view) (c) Mises stress of AlN film.

Stress analysis The discussion of stress analysis for FPS1016 is similar to what has been discussed for FPS725B. It is observed that the simulated maximum Mises stress values at 1 MPa loading condition for the materials are well below than their corresponding ultimate strength. Table 4.8 and Figure 4.24 show the results of the stress analysis.

Table 4.8 Simulated stress analysis of the 1016 dpi fingerprint sensor (FPS1016)

Applied Load (MPa)	Applied force (μN)	Mises stress of Al_2O_3, (MPa)	Mises stress of AlN (MPa)	Mises stress of Ti (MPa)	Mises stress of Al (MPa)
0.1	62.1	17.925	2.695	1.918	8.479
0.2	124	35.850	5.390	3.836	16.958
0.3	186	53.775	8.084	5.754	25.437
0.4	248	71.700	10.779	7.672	33.916
0.5	311	89.625	13.474	9.590	42.395
0.6	373	107.549	16.169	11.509	50.874
0.7	435	125.474	18.864	13.427	59.353
0.8	497	143.399	21.559	15.345	67.832
0.9	559	161.324	24.253	17.263	76.311
1.0	621	179.249	26.948	19.181	84.790

Spring constant Spring constant of the pixel for FPS1016 is calculated from the force displacement relationship. Figure 4.24 shows the spring constant plot of the pixel.

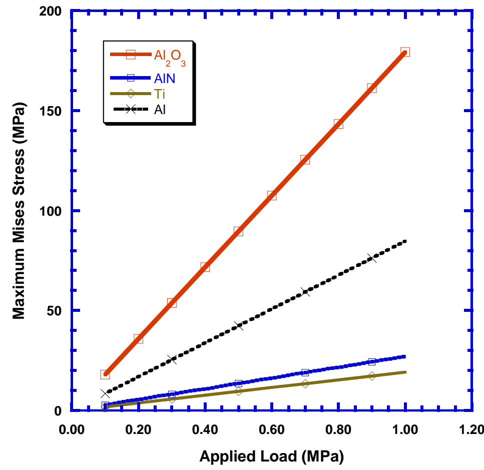

Figure 4.24 Simulation plot of maximum Mises stress of each layer with respect to different loads.

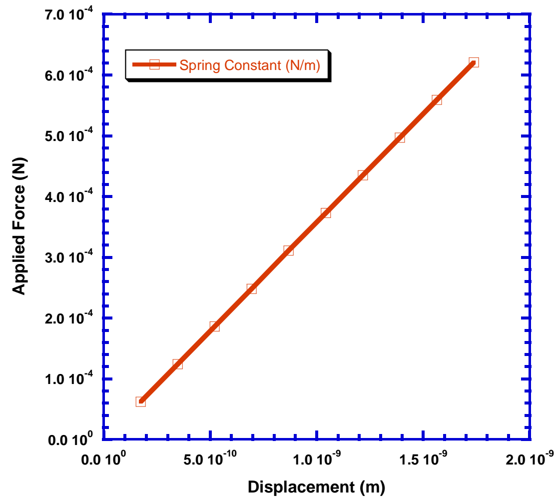

Figure 4.25 Simulation spring Constant of the pixel of FPS1016.

Piezoelectric Voltage Response The response of FPS1016 is calculated using simulation results and is shown in Figure 4.26. Table 4.9 shows the calculated values of the open-circuit piezoelectric output voltage (i.e., prior to including external CMOS circuits in the system) with respect to various finger pressure. Applied pressures are converted to applied force to calculate the response in Table 4.9.

Table 4.9 Simulation and modeling results of piezoelectric Response of the sensor (FPS1016)

Applied Load, P_L (MPa)	Applied Force, F (μN)	Charge Produced in the AlN film, Q (fC)	Capacitance, C (fF)	Piezoelectric Voltage, V (V)	Piezoelectric Response, R_F (V/N)
0.1	62.1	0.826	106	0.008	125.52
0.2	124	1.65	106	0.016	125.52
0.3	186	2.48	106	0.023	125.52
0.4	248	3.30	106	0.031	125.52
0.5	311	4.13	106	0.039	125.52
0.6	373	4.96	106	0.047	125.52
0.7	435	5.78	106	0.055	125.52
0.8	497	6.61	106	0.062	125.52
0.9	559	7.43	106	0.070	125.52
1.0	621	8.26	106	0.078	125.52

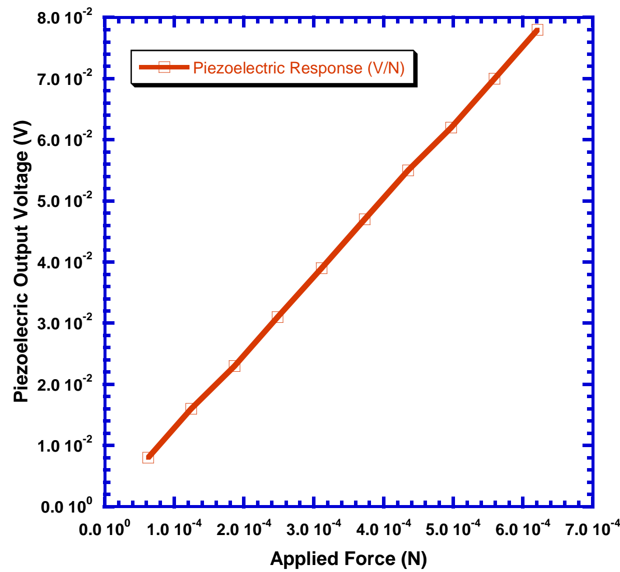

Figure 4.26 Simulation plot of piezoelectric output voltage of the sensor with respect to different loads mentioned in Table 4.9.

4.4 Noise Analysis

4.4.1 725 dpi fingerprint sensor (FPS725A)

Noise analysis for FPS725A should be much similar to the more complex structure FPS725B. Therefore, noise analysis is skipped in this section rather these are investigated for FPS725B and FPS1016.

4.4.2 725 dpi fingerprint sensor (FPS725B)

Johnson noise

Johnson noise occurs due to thermal agitation in the devices. For MEMS device or any kind of electronic device, this type of noise indicates an electrical noise which is related to electrical resistance of the sensing element rather than a mechanical entity. The Johnson noise can be modeled by an equivalent circuit (Figure 4.27).

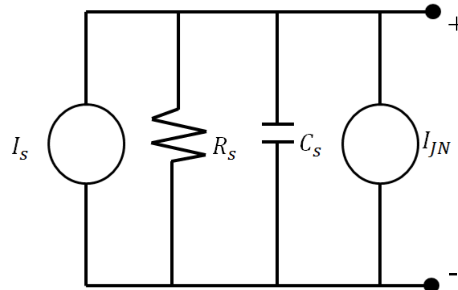

Figure 4.27 The equivalent electrical circuit

For a low frequency response where $f \to 0$, the power spectral density for Johnson noise voltage is,

$$S_{Jv}(f) = 4k_BTR \quad (4.1)$$

On the other hand, for a high frequency response,

$$S_{Jv}(f) = \frac{4k_BTR}{1+(2\pi fRC)^2} \quad (4.2)$$

where, $S_{Jv}(f)$ is the power spectral density, R is the electrical resistance of the sensing element, C is the capacitance of the sensing element, T is the absolute room

temperature, and k_B is the Boltzmann's constant. The values of the parameters are shown in the following table. The electrical resistance and the capacitance of the AlN film are assumed to be lumped and in parallel as shown in Figure 4.27. Therefore, the time constant of the RC circuit is calculated.

Table 4.10 Parameters for calculation of Johnson noise spectra (FPS725B)

Resistivity of AlN, ρ (Ω-m)	Area of AlN film, A_{AlN} (m^2)	Length of the AlN film for charge flow, L (m)	Resistance of the sensing element , R (Ω)	Capacitance of the sensing element, C (F)	Time constant for a parallel RC circuit, τ (s)
10×10^{9}	6.25×10^{-10}	2.0×10^{-7}	3.2×10^{12}	2.95×10^{-13}	0.9425

After that, Johnson noise voltage or current can be calculated by the following equations. For Johnson noise voltage,

$$v_{JN} = \sqrt{S_{Jv}} \tag{4.3}$$

and for Johnson noise current,

$$i_{JN} = \frac{v_{JN}}{R} \tag{4.4}$$

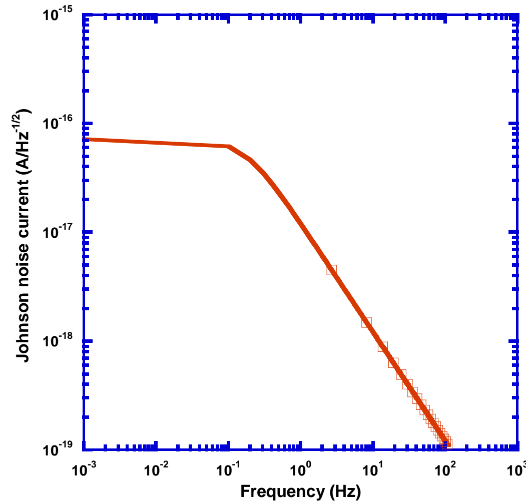

Figure 4.28 Johnson noise current plot from calculation.

Figure 4.28 shows the Johnson noise current spectra with respect to frequency. The value of the Johnson noise current at low frequency (e.g., where $f \approx 0$) is found to be 7.19×10^{-17} A.

Thermo-mechanical noise

Theoretical approach

Thermo-mechanical noise of the FPS725B can be approximated using theory used for microphone. Scheeper *et al.* [70] mentioned about thermal rms noise pressure of the microphone diaphragm where the diaphragm shape was octagonal but it was approximated with a circular diaphragm with a radius 'R'. Similar technique can be applied to approximate the thermal-mechanical noise for the square diaphragm based fingerprint sensor. The reason why the approximation is sufficient enough is simply because the displacement behavior of the membrane is similar to the behavior of a circular microphone and the displacement contour from the simulation validates the approximation. Figure 4.29 shows the displacement contour of the Al_2O_3 diaphragm.

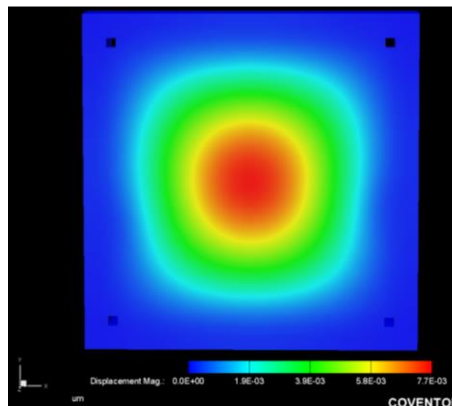

Figure 4.29 circular displacement contour of the square diaphragm.

So, the approximated thermo-mechanical rms noise pressure of the pixel diaphragm can be expressed by the following [70] where the pixel acts a linear oscillator. The unit of P is Pa/√Hz.

$$P = \sqrt{\frac{8.\sigma.t.k_B.T}{\pi.r^4}} \tag{4.5}$$

Where, P=thermo-mechanical rms noise pressure

σ=stress of the diaphragm

t=the diaphragm thickness

k_B=Boltzmann's constant

T=absolute room temperature

r=radius of the approximated circular diaphragm

To find the noise equivalent thermomechanical noise current the following is applied,

$$i_{TMN} = \frac{P.S_p}{R} \tag{4.6}$$

Where, S_p=pressure sensitivity or response (V/Pa)

Table 4.11 Parameters involving the thermo-mechanical noise applying theoretical results for FPS725B (assuming, T=300 K)

Mises Stress of the diaphragm, σ (Pa)	Diaphragm thickness,t (m)	Internal radius of the circular diaphragm, r (m)	Boltzmann's constant, k_B (J/K)	rms noise pressure, P (Pa/√Hz)	Pressure sensitivity, S_P,(V/Pa)	Noise equivalent voltage, v_{TMN} (V/√Hz)	Noise equivalent current, i_{TMN} (A/√Hz)
3.56×10^{8}	1.8×10^{-6}	1.5×10^{-5}	1.38×10^{-23}	11.56	1.41×10^{-7}	1.63×10^{-6}	5.22×10^{-19}

Loss-tangent/tanδ noise

In dissipation or lossy medium, the loss tangent of AlN film is approximately 0.034 [71] at low frequency operation i.e., at 20 Hz. Since, the sensing element has a resistance, R and a capacitor, C in parallel; therefore, the equivalent AC resistance will be different than equivalent series resistance associated with a capacitor. For a parallel combination of R and C, the tanδ equation becomes,

$$tan\delta = \frac{X_C}{R_{ac}} \tag{4.7}$$

Or,

$$R_{ac} = \frac{X_C}{\tan\delta} \tag{4.8}$$

Therefore, the noise current involving the ac resistance is,

$$i_{tan\delta} = \sqrt{\frac{4k_BT}{R_{ac}}} \tag{4.9}$$

For higher frequency operation, the tanδ noise becomes,

$$i_{tan\delta} = \sqrt{\frac{4K_BT}{R_{ac}(1+(2\pi f R_{ac}C)^2)}} \tag{4.10}$$

Using equation (4.8) and (4.10) the noise current related to loss tangent or tanδ is calculated. The following table (Table 4.12) shows the calculation results.

Table 4.12 parameters and calculation of loss tangent noise for FPS725B (Assuming T=300 K)

tanδ at 20 Hz	Capacitance of sensing element, C (F)	Reactance corresponding to capacitance, X_c (Ω)	AC resistance, R_{ac} (Ω)	Noise current, $i_{tan\delta}$ (A)
0.034	2.94×10^{-13}	2.70×10^{10}	7.95×10^{11}	1.44×10^{-16}

In frequency domain, the following plot is achieved (Figure 4.30).

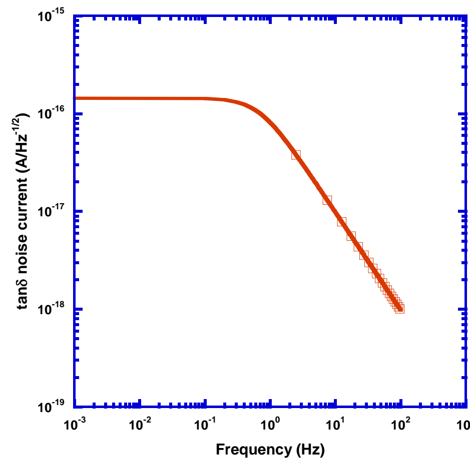

Figure 4.30 tanδ noise spectra from calculated data.

Total noise current

So the total rms noise current is,

Total noise current (when ω≈0) =√(Johnson noise current+ thermo-mechanical noise current+ loss tangent noise current)

$$\text{Or,} \qquad i_n = \sqrt{({i_{JN}}^2 + {i_{TMN}}^2 + {i_{tan\delta}}^2)} \qquad (4.11)$$

$$\text{Or,} \quad i_{n=}\sqrt{(7.19 \times 10^{-17})^2 + (5.22 \times 10^{-19})^2 + (1.44 \times 10^{-16})^2}$$

$$i_n = 2.16 \times 10^{-16}\ A/\sqrt{Hz}$$

Clearly, the loss tangent current and Johnson noise current dominate over thermo-mechanical noise at low frequencies. Figure 4.31 shows the noise components and total noise over a low frequency range. The total noise equivalent voltage is also calculated and the value is 2.57×10^{-4} V/√Hz.

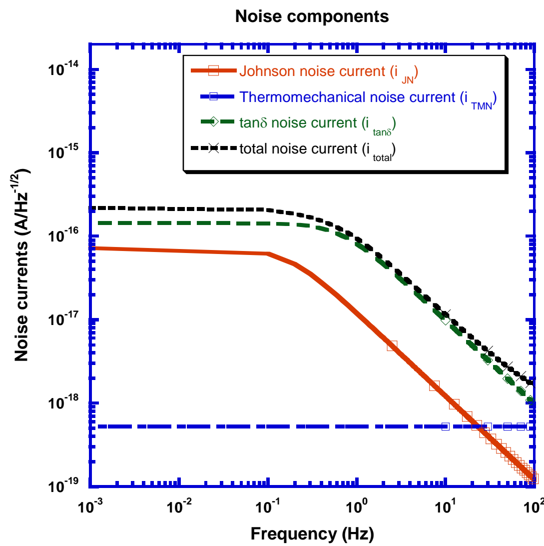

Figure 4.31 Plot from calculated data for total noise current of the pixel of FPS725B

4.4.3 1016 dpi fingerprint sensor (FPS1016)

Johnson noise

In a similar manner to section 4.4.2, Johnson noise voltage and Johnson noise current are calculated using described in that section. The values of the parameters are shown in the following table.

Table 4.13 Parameters for calculation of Johnson noise spectra (FPS1016)

Resistivity of AlN, ρ (Ω-m)	Area of AlN film, A (m^2)	Length of the AlN film for charge flow, L (m)	Resistance of the sensing element , R (Ω)	Capacitance of the sensing element, C (F)	Time constant, τ (s)
10×10^{9}	2.25×10^{-10}	2.0×10^{-7}	8.89×10^{12}	1.06×10^{-13}	0.9417

Figure 4.32 shows the Johnson noise current spectra with respect to frequency. The value of the Johnson noise current at low frequency (e.g., where f≈0) is found to be 4.31×10^{-17} A/√Hz.

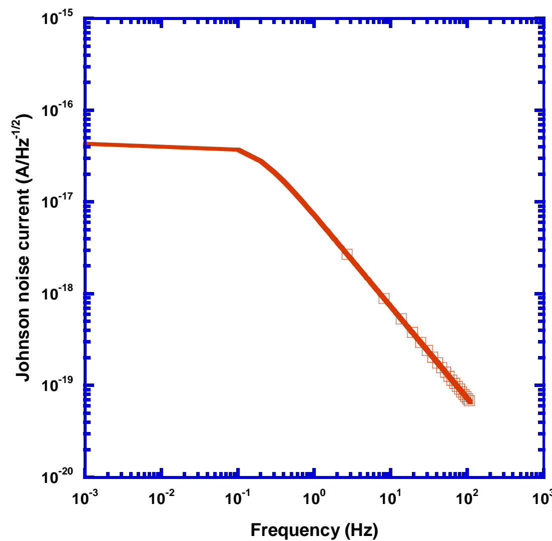

Figure 4.32 Johnson noise current spectra from calculated data

Thermo-mechanical noise

Theoretical approach

Although the parameters of FPS1016 are different, however, the mechanism is same as FPS725B. Equation (4.5) and (4.6) are applied to calculate the theromomechnaical noise current for FPS1016. The following table shows the parameters and calculation of rms thermomechanical noise current for FPS1016.

Table 4.14 Parameters involving the thermo-mechanical noise applying theoretical results for FPS1016 (assuming, T=300 K)

Mises Stress of the diaphragm, σ (Pa)	Diaphragm thickness,t (m)	Internal radius of the circular diaphragm, r (m)	Boltzmann's constant, k (J/K)	rms noise pressure, P (Pa/√Hz)	Pressure sensitivity, S_P,(V/Pa)	Noise equivalent voltage, v_{TMN} (V/√Hz)	Noise equivalent current, i_{TMN} (A/√Hz)
1.79×10^{8}	1.8×10^{-6}	1.0×10^{-5}	1.38×10^{-23}	18.44	7.8×10^{-8}	1.44×10^{-6}	1.62×10^{-19}

Loss-tangent/tanδ noise

Using equation (4.8) and (4.10) the noise current related to loss tangent is calculated. The following table (Table 4.15) shows the calculation results. In frequency domain, the following plot is achieved (Figure 4.33).

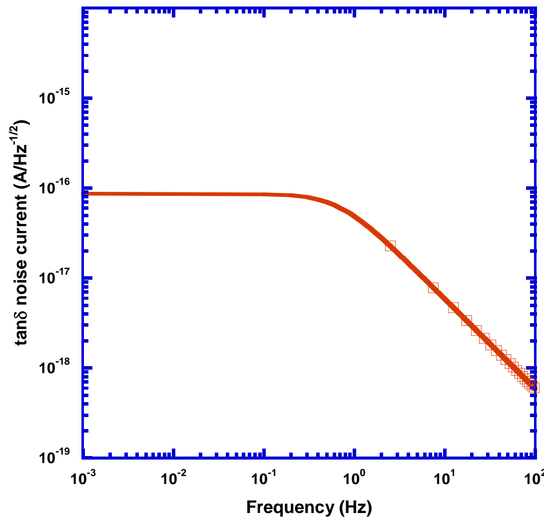

Figure 4.33 tanδ noise spectra from calculated data

Table 4.15 parameters and calculation of loss tangent noise for FPS1016 (Assuming T=300 K)

tanδ at 20 Hz	Capacitance of sensing element, C (F)	Reactance corresponding to capacitance, X_c (Ω)	AC resistance, R_{ac} (Ω)	Noise current, $i_{tan\delta}$ (A/√Hz)
0.034	1.06×10^{-13}	7.51×10^{10}	2.21×10^{12}	8.66×10^{-17}

Total noise current

The total rms noise current is, (when ω≈0)

$$i_n = \sqrt{({i_{JN}}^2 + {i_{TMN}}^2 + {i_{tan\delta}}^2)}$$

$$\text{Or,} i_{n=}\sqrt{(4.31\times10^{-17})^2 + (1.61\times10^{-19})^2 + (8.66\times10^{-17})^2}$$

$$i_n = 1.30\times10^{-16}\ A/\sqrt{Hz}$$

Clearly, the loss tangent current and Johnson noise current dominate over thermo-mechanical noise at low frequencies. Figure 4.34 shows the noise components

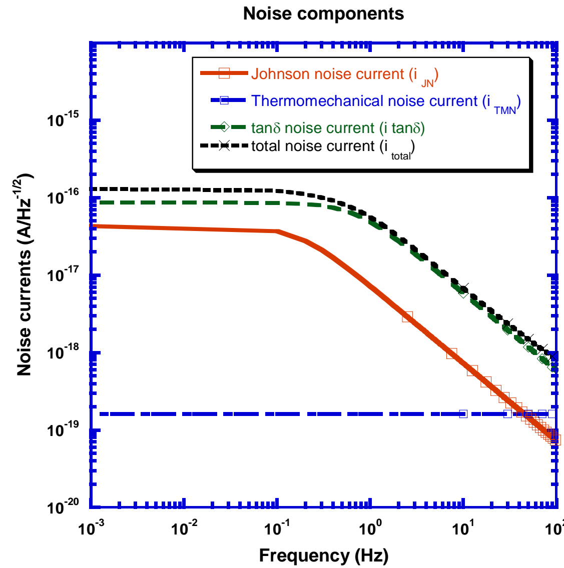

Figure 4.34 total noise current spectra from calculated data for the pixel of FPS1016

and total noise over a low frequency range. The total noise equivalent voltage is also calculated and the value is 4.29×10^{-4} V/√Hz.

4.5 Figures of Merit

4.5.1 725 dpi fingerprint sensor (FPS725B)

The voltage sensitivity (R_P) or response of the fingerprint sensor depends on change in voltage of the sensing material due to the pressure variation and is given as the change in the output voltage with pressure:

$$R_P = \frac{\Delta V}{\Delta P} \tag{4.12}$$

Where, ΔV is the change in output voltage for the pressure change ΔP applied on the sensor. The average voltage sensitivity of FPS725B due to applied finger pressure was calculated to be 1.41×10^{-7} V/Pa.

Another important figure of merit in this context is defined as the noise equivalent pressure (*NEP*), the amount of pressure changed on the sensor that will produce a signal to noise ratio (SNR) of 1. Hence, the *NEP* can be written as root mean square of total noise voltage divided by the voltage sensitivity:

$$NEP = \frac{V_{n(rms)}}{R_P} \tag{4.13}$$

where $V_{n(rms)}$ is the root-mean-square noise voltage which includes Johnson noise, thermomechanical noise, and tanδ noise.

Table 4.16 Calculated data of figures of merit for FPS725B

Response, R_P (V/Pa)	Johnson noise voltage, V_{JN} (V/√Hz)	Thermo-mechanical noise voltage, V_{TMN} (V/√Hz)	tanδ noise voltage, $V_{\tan\delta}$ (V/√Hz)	RMS noise voltage, $V_{n(rms)}$ (V/√Hz)	NEP (Pa/√Hz)	NEP_{JN} (Pa/√Hz))
1.41×10^{-7}	2.30×10^{-4}	1.62×10^{-6}	1.14×10^{-4}	2.57×10^{-4}	1.82×10^{3}	1.63×10^{3}

The *NEP* of FPS725B was calculated over the low frequency range and found to be 1.82×10^3 Pa/√Hz. In the Johnson noise limited system, the average *NEP* was found to be 1.63×10^3 Pa/√Hz over the low frequency range. The table 4.16 shows the figures of merit for FPS725B.

4.5.2 1016 dpi fingerprint sensor (FPS1016)

The average voltage sensitivity of FPS1016 due to applied finger pressure was calculated to be 7.8×10^{-8} V/Pa.

Another important figure of merit in this context is defined as the noise equivalent pressure (*NEP*), which was defined in the earlier section. The *NEP* of FPS1016 was calculated over the low frequency range and found to be 5.52×10^3 Pa/√Hz. In the Johnson noise limited system, the average *NEP* was found to be 4.92×10^3 Pa/√Hz over the low frequency range. The following table shows the figures of merit for FPS1016.

Table 4.17 Calculated data of figures of merit for FPS1016

Response, R_P (V/Pa)	Johnson noise voltage, V_{JN} (V/√Hz)	Thermo-mechanical noise voltage, V_{TMN} (V/√Hz)	tanδ noise voltage, $V_{tan\delta}$ (V/√Hz)	RMS noise voltage, $V_{n(rms)}$ (V/√Hz)	NEP (Pa/√Hz)	NEP_{JN} (Pa/√Hz))
7.80×10^{-8}	3.84×10^{-4}	1.44×10^{-6}	1.91×10^{-4}	4.29×10^{-4}	5.50×10^3	4.92×10^3

Comparing both the table of figures of merit, it is apparent that noise equivalent voltage and noise equivalent pressure increases with the decrease of sensing element area or with the scaling down the sensing element since lesser area of the sensing element produce higher resistance which in turn produces higher Johnson noise voltage and higher tanδ noise voltage. Voltage sensitivity with pressure is also decreased with the scaling but voltage sensitivity with force, however, increases with increase of applied force. The piezoelectric output voltage, here, is limited by the maximum finger pressure that can be applied on the fingerprint sensor. However, the sensitivity can be improved by

reducing the thickness of AlN film also to make it even thinner and flexible, e.g, 50 nm. Therefore, the aim of achieving high resolution for accurate and secure identification can be obtained with the scaling effect of the pixel. To improve the figures of merit, optimization is required.

4.5 Conclusions

Three novel MEMS piezoelectric fingerprint sensors have been designed using FEA software CoventorWare®. They were named as FPS725A, FPS725B, and FPS1016 where the number part indicates resolution of the sensors. As of the sensing element, piezoelectric, CMOS compatible, ultrathin AlN film was used. The thickness of the sensing element was 200 nm for each sensor. FPS725A consists of an array of 35 μm×35 μm (or 725 dpi) Al_2O_3 based diaphragm structure or pixels where a 26 μm×26 μm AlN film was patterned on top of the diaphragm and sandwiched between two Ti electrodes. For fabrication, the actual sensor dimension will be considered to be 15 mm×15 mm and that is applicable for FPS725B and FPS1016 as well. 3D model of a single pixel was created and mesh convergence was investigated. Fabrication process flow was also discussed. A polyimide layer of 4 μm thickness was used as the sacrificial layer to make a hollow or air gap for the diaphragm and to remove the polyimide layer few holes were created on the Al_2O_3 membrane layer. However, after the meshing mechanical analyses were done to understand the mechanical stability or strength of the device, to find the simulated values of the stress contour of the sensing element. The simulated stress results were applied to calculate the piezoelectric response of the fingerprint sensor. The maximum Mises stress of the device occurs in Al_2O_3 diaphragm and the value is 69.01 MPa which is almost 5 times lower than the value of its tensile strength. The piezoelectric response for FPS725A was calculated to be 225.74 V/N. Piezoelectric voltage increases proportionally with respect to applied load. For example,

piezoelectric voltage comes out 0.152 V in response to 1 MPa (or 676 μN) applied load or finger pressure whereas the sensor produces 0.0152 V at 0.1 MPa (or 67.6 μN) applied load. Spring constant was also calculated from the simulated results.

As of FPS725B, the diaphragm material, dimension as well as pixel resolution are same as FPS725A. Only difference was that the sensing element including the top and bottom electrodes were placed underneath the diaphragm instead of on top of it. Also, the sensing element i.e., AlN film was reduced in size and kept to 25 μm×25 μm. The design was a much more elaborated one compared to FPS725A, because for FP725B, electrical metallization wiring including contact pad was designed for CMOS electrical read out which was missing for FPS725A for simplicity of the design. Aluminum (Al) layer was used for wiring and gold (Au) was used as the contact pads. After the designing, the FPS725B pixel was meshed and simulated for mechanical analysis. The steps are quite similar to what was done for FPS725A. The piezoelectric voltage response with applied force for FPS725A was calculated to be 115.58 V/N. Finally, noise analysis was investigated for FPS725B. Johnson noise, thermomechanical noise and tanδ noise/loss tangent noise were investigated by theoretical calculation. Total noise was also calculated and plotted in frequency domain. The rms value of the total noise current for FPS725B was 2.16×10^{-16} A/√Hz. The comparisons between the noise components were observed in the plot. It was apparent that the tanδ noise and Johnson noise dominates over thermomechanical noise. The maximum stress of the device (or pixel) occurs in Al_2O_3 diaphragm and this time around it was a compressive stress of 356.49 MPa at 1 MPa (or 1220 μN) applied load that occurs in Al_2O_3 diaphragm. Since, the value of the compressive strength of Al_2O_3 ranges between 0.69 GPa~5.5 GPa, therefore, the maximum mises stress of the device in the simulation does not affect much toward the performance of the device. In other way, the device is mechanically very

stable since the maximum stress of the device remains well below than the strength of Al_2O_3 material. As far as piezoelectric response concerned, it gives lower value than the first configuration; however, this configuration provides more mechanical stability and safety for the device. The voltage produced due to 1 MPa load or finger pressure was 0.141 V. With same pixel size or resolution, the piezoelectric output voltage for FPS725B is little lesser than FPS725A.

For FPS1016, the dimension of each Al_2O_3 based pixel is 25 μm×25 μm (or 1016 dpi) whereas the AlN sensing element is 15 μm×15 μm which is equivalent to a pixel resolution of 1016 dpi. All the simulation and analysis are pretty much similar to what was done for FPS725B. The piezoelectric voltage response with applied force for FPS1016 was calculated to be 125.52 V/N. For noise analysis, tanδ noise and Johnson noise dominates over the thermomechanical noise. The rms value of the total noise current for FPS1016 was 1.30×10^{-16} A/√Hz. With reduction of pixel size, the response improves for fingerprint sensor since FPS1016 provides better response than FPS725B under fixed finger pressure or applied load. So, it can be concluded that with scaling down or shrinking of the device, the responsivity and the resolution both are improved. Moreover, FPS1016 produces lesser Mises stress (179.25 MPa) in the Al_2O_3 diaphragm than FPS725B which produces maximum Mises stress of 356.49 MPa in the diaphragm structure under a fixed loading condition i.e., at 1 Mpa finger pressure.

Therefore, it can be proved that with the scaling down effect, the overall performance of the fingerprint sensor improves in a great manner without affecting its physical property or changing any material characteristics. FPS1016 or 1016 dpi fingerprint sensor provides more responsitivity, more mechanical stability and higher resolution using ultrathin AlN film as the sensing element than that of FPS725B. For future work, the design of FPS1016 and FPS725B can be implemented through

fabrication and characterization to analyze the performance of the device for practical use. Also, comparing the noise equivalent pressure between both fingerprint sensors (FPS725B and FPS1016), it is apparent that NEP (5.50×10^{3} Pa/√Hz) is higher in 1016 dpi sensor than the NEP (1.82×10^{3} Pa/√Hz) in 725 dpi sensor.

Chapter 5

Ultrathin AlN based Piezoelectric MEMS Accelerometer

5.1 Introduction

With the increase in demand of MEMS inertial sensors such as accelerometers and gyroscopes, MEMS market is booming rapidly. Starting from the automobile safety to health monitoring, MEMS accelerometers have been playing a pivotal role in changing the world, improving the quality of life. The applications of MEMS accelerometers are so dynamic and wide that these are used in many applications such as military, aerospace, automobile industry, seismology and so on. Among these applications, accelerometers are mostly known for their uses in aircraft/automobile airbags. Apart from the automotive industry, the rest of the markets typically produce inertial MEMS sensors for consumer applications. The major companies in MEMS industry like Analog Devices, STMicroelectronics, Freescale, Bosch are producing different accelerometers with different size and sensitivities and building up billion dollars MEMS market. The combination of accelerometers and gyroscopes in inertial measurement units (IMUs) are getting popular in aircrafts, satellites, spacecraft, guided missiles, GPS devices, game controllers and in many other applications.

There are various types of accelerometers, for examples, resonant accelerometers, beam accelerometers, tunneling accelerometers, convective and bubble accelerometers, 1D to 6D accelerometers (i.e., piezoresistive accelerometers, capacitive accelerometers, and piezoelectric accelerometers). The basic mechanism of an accelerometer can be realized in a mass-spring-damper system which will be discussed in this chapter. For the scope of our work, 1D piezoelectric accelerometer will be highly emphasized.

5.1.1 Basic concepts

Like many other transducers, accelerometers follow transduction mechanism where a mechanical input is converted to an electrical output. In accelerometers, acceleration is, particularly, converted into deflections or stress deviations. The deflections or stress deviations are then converted into an electrical output signal. However, for any inertial system, the output depends on six inertial forces which are produced due to three linear accelerations and three angular accelerations. For example, in a 1D accelerometer, the effects of all the accelerations (i.e., in six directions) are present but only one inertial force is dominant over others. In other way, the cross-coupling effects are negligible or suppressed by the dominant inertial force in the system.

Since an accelerometer detects the movement of an entity in inertial space, and later acceleration, therefore, the principle of any accelerometer can be realized with a mass-spring system. Typically, a mass-spring system consists of a seismic mass which is oscillated within the system and clamped to an object of interest. However, the spring or beam structure supports the seismic mass and the displacement-sensing element (i.e., capacitive, piezoresistive, piezoelectric and so on). The sensing element realizes the force which is acted up on the test object as well as the seismic mass.

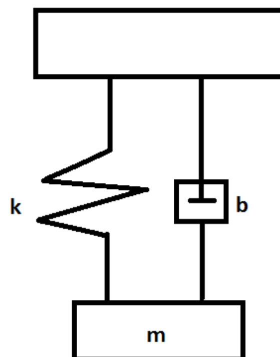

Figure 5.1 Mass-spring-damper system.

The basic structure and operation of a linear accelerometer can be modeled as mass-spring-damper system as shown in Figure 5.1. A complete MEMS accelerometer structure can be connected to a rigid or flexible surface such as Silicon substrate via anchors. The anchors are typically connected to the suspended proof mass via spring. The behavior of springs depends of its geometry, material property, and proof mass weight and so on. The proof mass can be of a single layer to multiple layers depending on the device specification. During oscillation of the proof mass, damping forces comes into play. They play an important role toward the performance of an accelerometer. In an ideal condition such as in vacuum, damping effect is considered negligible or zero. The dynamic behavior for the mass-spring-damper system relative to the substrate can be described by Newton's second law of motion and is expressed in Equation 5.1.

$$m\ddot{x} + b\dot{x} + kx = -F = -ma_{pm} \tag{5.1}$$

where, m = mass of the proof-mass , b = damping coefficient of the system, k = spring constant, a_{pm} = acceleration of the proof-mass and x = relative displacement of the proof-mass with respect to the substrate.

A Laplace transfer function is achieved by introducing s in place of the derivative operators, and the transfer function is

$$\frac{X(s)}{A_{pm}(s)} = -\frac{1}{s^2 + \frac{b}{m}s + \frac{k}{m}} \tag{5.2}$$

If we consider, $\omega_n = \sqrt{\frac{k}{m}}$ as the resonant or natural frequency of the device, and $\zeta = \frac{b}{2\sqrt{km}}$ as the damping ratio, we get,

$$H(s) = -\frac{1}{\left(\frac{s}{\omega_n}\right)^2 + \left(2\zeta\frac{s}{\omega_n}\right) + 1} \tag{5.3}$$

During the oscillation due to applied force or acceleration, the sensing element which converts the mechanical motion into an electrical signal are made of a variety of

materials such as resistive, capacitive, inductive, piezoelectric, piezoresistive, and optical effects.

5.1.2 Ideal criteria a single/multiaxial (1D to 3D) accelerometer [72]

- The output should be linear with respect input. For example, $Y_{out}=mX_{in}$ where, m is a scaling factor.
- The resolution or minimum detectable signal is typically realized by the spectral density of the output signal in g/√Hz and is equal to the noise density.
- For a zero input, there must be zero output signal or close to zero.
- The system should demonstrate negligible cross-coupling effects.
- Output of the system must show stability over temperature variations and over time.
- While operating, the system should not have a drop-out and malfunction.

5.1.3 Primary specification parameters for commercially available sensors *[72]*

- Sensitivity
- Linearity
- Resolution
- Bias
- Bias drift
- Cross-axis sensitivity
- Shock robustness
- Vibration sensitivity against high-frequency accelerations
- Self-test capability
- Safety

5.1.4 Piezoelectric accelerometers

Piezoelectric accelerometers are structurally somewhat similar to the piezoeresistive transducers. The piezoelectric sensing element or material e.g, AlN, ZnO, PZT etc. do not require external biasing since they can provide their own biasing due to their intrinsic ability to be polarized under stress or without stress. These materials are deliberately placed on the supporting beams or springs of the device where the induced stress is relatively high. The piezoelectric material in an accelerometer is usually sandwiched between two electrodes so that the produced charge/voltage can be measured via electrodes. When acceleration is applied to the accelerometer, a corresponding force/pressure is applied to the opposite surfaces of the piezoelectric material due to motion of the proof mass, and an electric charge is generated. The charge can then be converted to voltage through a preamplifier and signal external signal conditioning circuit arrangements.

Among the parameters that define the characteristics of a particular accelerometer, sensitivity and operating frequency range (i.e., this is the frequency bandwidth where sensitivity does not deviate or barely deviates) are the most important ones. Usually, the upper limit of the operating frequency range is restricted by the first resonant frequency of the accelerometer. In a 1D or single axial piezoelectric accelerometer, the improvement in sensitivity is achieved by increasing the mass of the proof mass. However, the increase of mass reduces the resonant frequency of the device and, hence, constricts the operating frequency range. So, there is a trade-off between the operating frequency range and the sensitivity.

5.1.5 Background

The history of MEMS accelerometer is quite old. In 1979, bulk-micromachined cantilever based piezoresistive accelerometer was introduced [73] with a view to batch

fabrication. Both static and dynamic behavior of the accelerometer was discussed in the paper. In 1990, a bulk-micromachined silicon based capacitive accelerometer including CMOS integrated circuit was developed for micro-gravity measurement in spacecraft [74]. The cross-sensitivity was 0.4 % which was a significant improvement than the previous developments of accelerometer but the package size for the system was relatively large i.e., 33 mm×15 mm×5 mm. The accelerometer was developed to provide selectivity and optimization for the system for the measurement of the residual acceleration that ranges from 1 μg to 0.1g in acceleration and 0.01 to 100 Hz in frequency. Silicon was used as proof mass with a 3000 μm long silicon beam. Resonant frequency was measured to be 2330 Hz and the transverse sensitivity was around 10%. In 1994, a tri-axis capacitive accelerometer was introduced by [75] where the off-axis sensitivity varied 1.3%-7.3%. A ZnO based piezoelectric accelerometer was first introduced by [76] in 1996. A theoretical discussion of the accelerometer was discussed where mechanical-thermal noise of the bulk-micr machined accelerometer was discussed and the detection level was expected to be 10^{-3} $ms^{-2}/\sqrt{Hz}$. In 1996, PZT based bulk-micromachined accelerometer was developed [77]. The sensitivity was 320 mV/g and the resonant frequency was 225 KHz. In 1999 [78], ZnO based piezoelectric accelerometers were developed using bulk-micromachining technique. The sensitivity was measured to be 0.1 pC/g and a noise detection level was estimated to be 1×10^{-4} $g/\sqrt{Hz}$. Although, the measurements in [78] exhibited high-directional sensitivity but an accurate measurements of the cross-axis sensitivity like [74] was not possible with their experimental set up. In 2001, S. P. Beeby et al. [79] discussed about a bulk-micromachined PZT/Silicon based z-axis accelerometer which showed a sensitivity of 16 pC/ms^{-2} and a resonant frequency of 7.55 kHz experimentally. Before that, FE modeling was done and a calculated sensitivity of 400 μV/g at 1g input was found. Experimental cross sensitivity was achieved 4% as reported.

The accelerometer had a proof mass of 17 mg in weight and 4 mm^2 in dimension. The piezoelectric layer was very thick I.e., 60 μm compared to thin-film based accelerometer which means the accelerometer was not that much flexible. Again in 2001, ZnO based surface micromachined accelerometers were reported by D. L. DeVoe *et al.* [80]. Two different designs were reported. One design was a simple cantilever based design without any proof mass and the other design had four cantilever beams with a suspended proof mass. The design without proof mass showed a measured sensitivity of 0.21 mV/g at a 3.3 kHz (measured) resonant frequency. On the other hand, the design with two different proof masses showed 13.3 mV/g and 44.7 mV/g measured sensitivities at 2.23 kHz and 1.02 kHz resonant frequency, respectively. The radius of curvature for the cantilever based accelerometers was also measured and it was 455 m^{-1}. In 2003, two different shaped (i.e., trampoline and annular diaphragm accelerometers) diaphragm based bulk-micromachined accelerometers with PZT thick films were reported [81]. The reported thickness of PZT film ranged from 1.5-7 μm. Piezoelectric sensitivities were measured and they ranged from 0.77 pC/g to 7.6 pC/g at resonant frequencies that ranged from 35.3 kHz to 3.3 kHz. The reported minimum detectable signal was 30 μg at 100 Hz operating frequency. The cross sensitivity was less than 2%. The measured and FEA results show good consistency with each other. In 2004, an analytical and FE modeling of a bulk-micromachined accelerometer using PZT thin film was reported [82]. The analytical sensitivity was 5.02 pC at 4.77 kHz driving frequency. The maximum acceleration that can be measured by the accelerometer was estimated to be 1220 g and the analytical resonant frequency was 5.78 kHz. No analysis for noise was reported. In 2004, Q. Zou *et al.* [83] reported about bulk-micromachined tri-axis accelerometer using ZnO thin film. The reported sensitivities in x, y and z-axis were 0.93 mV/g, 1.13 mV/g and 0.88 mV/g, respectively at 1 g acceleration and an operating frequency of 20 Hz. The

minimum detectable signal was found to be 0.04 g over a bandwidth of 100 Hz from the experiment. However, the cross-axial sensitivity was around 15% which was kind of high. In 2006, AlN based bulk-micromachined accelerometers were fabricated using SOI techniques in order to reduce noise floor [25]. The thickness of the AlN film was 1.5 μm. Charge sensitivities varied from 0.06 pC/g to 0.45 pC/g based on design parameters. Brownian noise floor was calculated which ranged from 0.55 to 2.3 μg/√Hz and the measured noise floor ranged from 0.5 to 1 μV/√Hz. The accelerometers were operated in the range of 50 Hz to 3.2 Hz dynamic frequency range. In 2007, F. Gerfers et al. [84] reported about CMOS-compatible AlN based surface micromachined MEMS accelerometers which showed an experimental sensitivity of 5.2 pC/g and a very low noise floor I.e., 670 ng/√Hz which means the accelerometer showed very good signal-to-noise ratio. The resonant frequency was 1.1 kHz in this case. The authors focused on improving the sensitivity per area. Quality factor was reported to be 160. However, the size of the accelerometer sensor was quite big and it was 45.8 mm^2. In 2009, post-CMOS-compatible AlN based bulk-micromachined resonant MEMS accelerometers were reported [31]. The sensitivity, quality factor, and bandwidth were measured to be 3.4 Hz/G, 5090, and 1.4 kHz, respectively. The minimum detection level is found to be 0.9 mG/√Hz over 10 to 200 Hz frequency range. The proof mass weight was around 110 ng. The principle in resonant frequency is quite different than in capacitive, piezoeresistive, piezoelectric, optical or tunneling accelerometers because unlike others the key parameter to measure is the change in resonant frequency induced by strain. The oscillation induced by these resonators showed very low phase noise due to high quality factor and linear piezoelectric conversion of AlN thin films i.e, 1 μm which was sputter deposited at 350 ^{o}C. In 2009, T. Kobayashi et al. [85] reported a SOI based digital output piezoelectric accelerometer where PZT thin films was used as the sensing element. The

piezoelectric accelerometer was fabricated with a view to chicken health monitoring. The maximum measured sensitivity was found to be 30.8 mV/g. The resonant frequency was measured to be 33 Hz. For practical application for chicken health monitoring, the accelerometers were operated at 90 Hz. At the discussion section, the authors commented on the improvement of the metal wiring loss and suggested that Al which has relatively lower resistivity than Pt could be used for metallization wiring instead of Pt. Again in 2009, T Kobayashi *et al.* [86] reported about SOI based digital out piezoelectric accelerometer where CMOS-compatible AlN thin film was used. The reported measured sensitivity was 184 mV/g and it was 6 times higher than the PZT thin film based accelerometer. The measured resonant frequency was 53 Hz. However, the accelerometers tested at 1 g acceleration at a frequency of 80 Hz. C. Hindrichsen et al. [87] in 2009, reported two different bulk micromachined tri-axial PZT based accelerometers where both the accelerometers had a resonant frequency of 25 kHz. The measured sensitivity was 0.927 mV/g for both type of accelerometers. The cross axial sensitivity was found to be as low as 0.7%. The thickness varied from 15 μm to 100 μm for PZT film. In the same year, a bulk-micromachined circular PZT accelerometer was reported for high bandwidth application [88]. The thickness of the PZT film was 24 um as reported. The measured sensitivity and the quality of the accelerometer was 0.24 mV/g and 340, respectively. The resonant frequency was 23.5 kHz whereas the bandwidth was between 0.1 to 4 kHz. The accelerometer responded linearly up to 45 g. In 2011, M. Hrairi *et al.* [89] reported about a piezoresistive silicon based surface micromachined accelerometer. The authors mainly discussed about the design and modeling of the accelerometer. According to the design, the resonant frequency was greater than 1 kHz and the bandwidth was greater than 4 kHz. The acceleration was designed to be less than 0.02 g. The design was carried out a FEA analysis software ANSYS. In 2011, S.

Shanmugavel *et al.* [90] Reported about a piezoelectric thin films based miniaturized acceleration sensors where PLZT was used as the piezoelectric film. SOI bulk machining technique was used for the fabrication. Depending on the accelerometer dimension, the resonant frequencies of all the accelerometers ranged from 8 to 35 kHz. The sensors had a high signal to noise ratio. The peak to peak voltage output of a packaged sensor was measured to be 1 mV at 2g acceleration and at 16 kHz operating frequency. In 2013 [91], PZT based bulk-micromachined accelerometers were demonstrated where Silicon cantilever based simple accelerometer and bulk silicon proof mass based accelerometer were discussed. The resonant frequency for the accelerometers ranged from 60 Hz to 1.5 kHz and sensitivities ranged from 3.4 pC/g to 50 pC/g. The minimum detection level was measured to be 1.7 $\mu g/\sqrt{Hz}$ at 30 Hz. As per the report, PZT film was 800 nm thick but the device size was quite big. They also reported about loss tangent for PZT film as 0.02. In 2014, bulk-micromachined ZnO based accelerometer was reported [92]. At 500 Hz operating frequency, a theoretical sensitivity of 5.07 mV/g was realized and the experimental sensitivity was measured to be 1.69 mV/g. The theoretical and measured resonant frequencies were 2.437 kHz and 2.189 kHz, respectively. Table5.1 summarizes most of the previous works on piezoelectric accelerometers from the literature.

We propose a surface-micromachined, CMOS compatible ultrathin AlN based piezoelectric accelerometer for low bandwidth and high sensitivity application. The design, modeling and analysis results of the accelerometer will be discussed thoroughly in the following chapters.

5.2 Design and Simulation

We propose AlN based single-axial piezoelectric accelerometer which is designed using CoventorWare®. Before designing the accelerometer, resonant frequency, bandwidth, and damping ratio are chosen. Based on these parameters, spring

Table 5.1 Summary of previous works on piezoelectric MEMS accelerometers

Sl. No.	Authors	Year	Material	Sensitivity and other features	NEA*/MDS*	Resonant frequency	Fabrication process (μ-machining)
1	P. Scheeper *et al.* [76]	1996	ZnO	--	1×10^{-3} $ms^{-2}/\sqrt{Hz}$	10 kHz	bulk
2	Y. Nemirovsky *et al.* [77]	1996	PZT	320 mV/g	78×10^{-3} $ms^{-2}/\sqrt{Hz}$	225 kHz	bulk
3	R. de Reus, P. Scheeper [78]	1999	ZnO	0.1 pC/g	9.8×10^{-4} $ms^{-2}/\sqrt{Hz}$	4.5 kHz	bulk
4	Beeby *et al.* [79]	2001	PZT	16 pC/ ms^{-2}	--	7.55 kHz	bulk
5	D. L. DeVoe *et al.* [80]	2001	ZnO	13.3 fC/g at 2.23 kHz, 44.7 fC/g at 1.03 kHz	--	2.23 kHz, 1.03 kHz, 3.3 kHz	surface
6	L.-P. Wang *et al.* [81]	2003	PZT	0.77 pC/g to 7.6 pC/g.	30 μg at 100 Hz	35.3 kHz to 3.7 kHz	bulk
7	Q.-M. Wang *et al.*[82]	2004	PZT	5.02 pC at 4.77 kHz	--	5.78 kHz	bulk
8	Q. Zou *et al.* [83]	2004	ZnO	S_x=0.93 mV/g, S_y=1.13 mV/g, S_z=0.88 mV/g	0.04g over a 1~100 Hz bandwidth	100 Hz	bulk
9	L. –P. Wang *et al.* [25]	2006	AlN	0.06 to 0.45 pC/g	0.5-1.0 μV/√Hz; Brownian NF=0.55 -2.2 μg/√Hz	--	bulk
10	F. Ferfers *et al.* [84]	2007	AlN	5.2 pC/g	670 ng/√Hz	1.1 kHz	surface
11	R. H. Olsson et al. [31]	2009	AlN	3.4 Hz/G	0.9 mG/√Hz over 10 to 200 Hz	1.4 kHz	bulk
12	T. Kobayashi *et al.* [85]	2009	AlN	184 mV/g (6 times greater than with PZT)	--	Measured resonant frequency 53 Hz	SOI
13	T. Kobayshi *et al.* [86]	2009	PZT	S (calc.)=30.8 mV/g at 33 Hz	--	--	SOI
14	C. C. Hindrichsen *et al.* [87]	2009	PZT	S_v=2.75 mV/g (D_1), S_h=2.75 mV/g (D_1), S_v=0.927 mV/g (D_2), S_h=0.927 mV/g (D_2)	--	25 kHz	bulk
15	C. C. Hindrichsen *et al.* [88]	2009	PZT	S_v=0.24 mV/g, S_q=0.23 pC/g Quality factor=340		23.5 kHz, bandwidth= 0.1-4 kHz	bulk
16**	M. Hrairi *et al.* [89]	2011	Piezo resistive	--	--	>1 kHz (design)	surface
17	S. Shanmugavel *et al.* [90]	2011	PLZT ((Pb,La)(Zr,Ti))	V_p=0.5 mV, Acc.= 2g, S=V/G=0.25 mV/g at 16 kHz operating frequency; High SNR		22.4 kHz	bulk/SOI
18	N. N. Hewa-Kasakarage *et al.* [91]	2013	PZT	3.4-50 pC/g	1.74 μg/√Hz at 30 Hz	60 Hz~1.5 kHz	bulk
19	C. Saayujya *et al.* [92]	2014	ZnO	5.07 mV/g (theo.) 1.69 mV/g (exp.) at 500 Hz frequency.	--	2.43 kHz (theo.) 2.19 kHz (exp.)	bulk

(Here, NEA=noise equivalent acceleration, MDS=minimum detectable signal, S_v=vertical sensitivity, S_h=horizontal sensitivity, theo. =theoretical, exp. =experimental, D_1=design 1, D_2=design 2, calc. =calculated)

stiffness and proof mass geometry are designed. There are several steps in design process in CoventorWare®. At first, all the lithography steps, layer names, selectivity of photoresists, thickness of the materials used in the design are mentioned. For substrate material, silicon_100 is chosen. After that, a Si_3N_4 film of 2 μm is chosen as the passivation layer. For fabrication, Si_3N_4 will be sputtered uniformly on top a silicon wafer. Next, a 10 μm thick polyimide which will be used as a sacrificial layer is deposited on top of the passivation layer. Then, using standard lithography process, polyimide layer is patterned. Then, Aluminum oxide (Al_2O_3) is deposited all over the wafer and planarized where thickness of Al_2O_3 is kept 5 μm except the anchor parts which are made of Al_2O_3 film as well. After that, Al_2O_3 film is patterned to get the device pattern that includes the proof mass, four springs on both sides of the proof mass and the anchors. Next, Tungsten material of 4 μm thickness is electroplated and patterned to add some weight to the proof mass. After that, 100 nm thick titanium (Ti) material is sputtered and patterned to shape the bottom electrode. Similarly, a 200 nm thick AlN layer and a 100 nm thick Ti layer are also sputtered as piezoelectric layer and top electrode layer, respectively. Liftoff process is used to pattern all metal layers. After that, another Al_2O_3 layer of 200 nm thickness is deposited again and patterned as an insulation layer to avoid electrical short between top and bottom electrodes. Two different masks are used for patterning the insulation layer. First mask is used to get a square like pattern where positive photoresist is used for the lithography process and second mask is used to etch a square shaped hole on the previous pattern. However, in the next step, the polyimide layer is removed

by ashing process to release the proof mass and springs so that they can move during oscillation or any mechanical vibration. After that, a lift off process is employed for the metallization wiring from the top electrode. Aluminum material of 200 nm is used for the metallization wiring. The wiring is extended to the top surface of the passivation layer such a way so that it is connected to contact pad which is deposited in the next step. Another lift off process is used for the contact pad which is also made of Al film. The thickness for the contact pad is kept 0.3 µm. The process editor steps are shown in Figure 5.1. Then, a 2D layout (Figure 5.2) is drawn and used to build a solid model. The 3D solid model of the accelerometer is built using CoventorWare® preprocessor with the help of layout editor and process editor. The whole process flow is broken down into two figures for clarity of understanding. Figure 5.3 and Figure 5.4 show the process flow of the 3D solid model of the accelerometer where sequence (a)-(l) are shown in Figure 5.3 and sequence (m)-(p) are shown in Figure 5.4. However, the solid model is meshed afterwards. Different regions are meshed differently. Before proceeding into mechanical simulation, mesh convergence is studied thoroughly. Once the mesh convergence is satisfied then all the mechanical analyses are carried out. Modal Harmonic analysis is studied thoroughly. Static parametric mechanical analyses are carried out with respect to different loading conditions or accelerations. Stress analyses in the AlN film are analyzed and normal stresses such as S_{xx}, S_{yy}, S_{zz} are used to calculate the surface charge densities of the piezoelectric film. Figure 5.5 shows the completed accelerometer. Figure 5.6 shows the partial view of the model including the meshed model.

Finally, piezoelectric output voltages and response are calculated using the voltage-charge relationship for a rectangular shaped parallel plate capacitor. The results are discussed in Results and Discussion section of this chapter. The dimension of each layer is shown in Table 5.2.

5.2.1 Process editor

Process Editor - [C:/Coventor/Design_Files/MEMS_Accelerometer/Devices/SR_piezo_accelerometer_including_trilayer_test.proc *]

File Edit View Tools Windows Help

Number	Step Name	Layer Name	Material Name	Thickness	Mask Name	Photoresist	Depth	Mask Offset	Sidewall Angle
0	Substrate	Substrate	SILICON_100	20	SubstrateMask				
1	Stack Material	passivation_layer	SI3N4	2					
2	Planar Fill	sacrificial_layer	POLYIMIDE	10					
3	Straight Cut				sacrificial	-		0	0
4	Planar Fill	anchor_and_spring	AL2O3	5					
5	Straight Cut				device_and_beam	+		0	0
6	Conformal Shell	Tungsten	TUNGSTEN	4					
7	Straight Cut				Tungsten	+		0	0
8	Conformal Shell	bottom_electrode	TITANIUM	0.1					
9	Straight Cut				bottom_electrode	+		0	0
10	Conformal Shell	piezoelectric_layer	AlN	0.2					
11	Straight Cut				piezo	+		0	0
12	Conformal Shell	top_electrode	TITANIUM	0.1					
13	Straight Cut				top_electrode	+		0	0
14	Conformal Shell	insulation_between_electrodes	AL2O3	0.2					
15	Straight Cut				inslulation_between_electrodes	+		0	0
16	Straight Cut				insulation_cut	-		0	0
17	Straight Cut				sacrificial_2nd_cut	-		0	0
18	Conformal Shell	contact_pad	ALUMINUM	0.3					
19	Straight Cut				contact_pad	+		0	0
20	Delete		POLYIMIDE						

Figure 5.1 Process Editor

5.2.2 2D layout

Table 5.2 Accelerometers design parameters and their symbols

Parameters	Abbreviation	Values (μm)
Length of Al_2O_3 and Tungsten proof mass	L_P	2000
Width of Al_2O_3 and Tungsten proof mass	W_P	1000
Length of Springs	L_S	1000
Width of springs	W_S	100
Anchor length (square)	A_L_1	500
Anchor width (square)	A_W_1	500
Anchor length (rectangular)	A_L_2	600
Anchor width (rectangular)	A_W_2	100
Length of piezoelectric layer	L_{Piezo}	200
Width of piezoelectric layer	W_{Piezo}	90
Length of contact pad	L_{CP}	90
Width of contact pad	W_{CP}	90
Length of top electrode	L_{top}	180
Width of top electrode	W_{top}	80
Length of small opening for top electrical connection	L_O	30
Width of small opening for top electrical connection	W_O	30
Length of bottom electrode	L_{bot_1}	500
	L_{bot_2}	100
	L_{bot_3}	700
Width of bottom electrode	W_{bot_1}	495
	W_{bot_2}	90
	W_{bot_3}	90

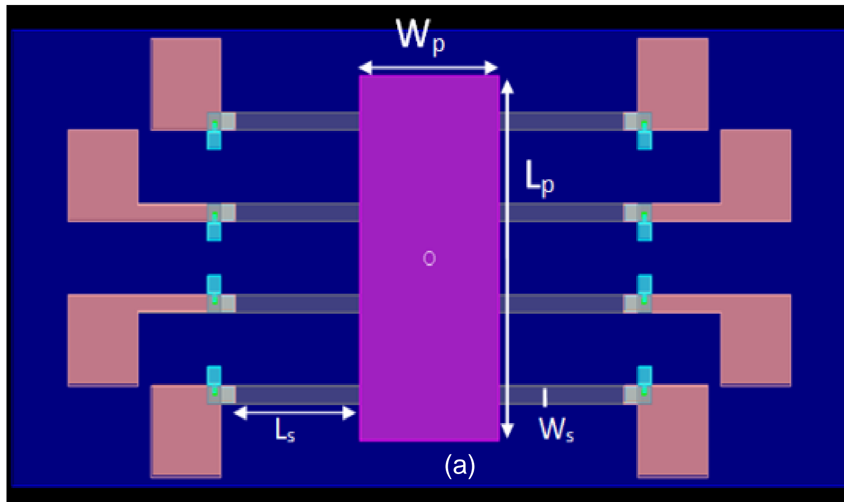

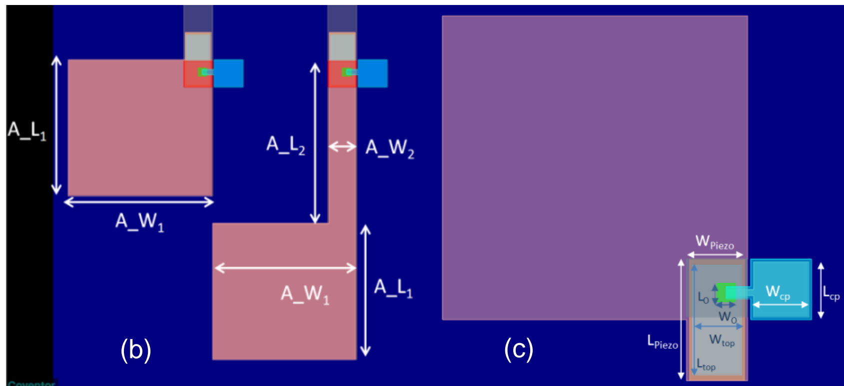

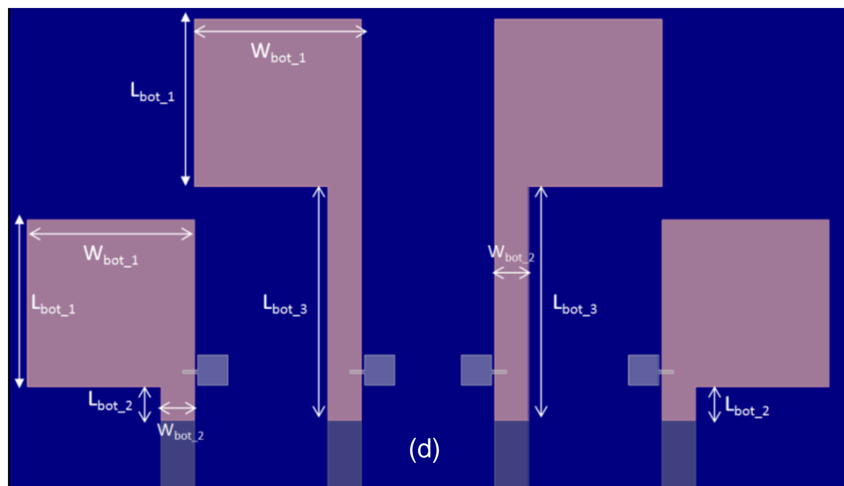

Figure 5.2 2D layout (a) full view, (b), (c) and (d) partial view

5.2.3 The Design process flow in 3D solid model

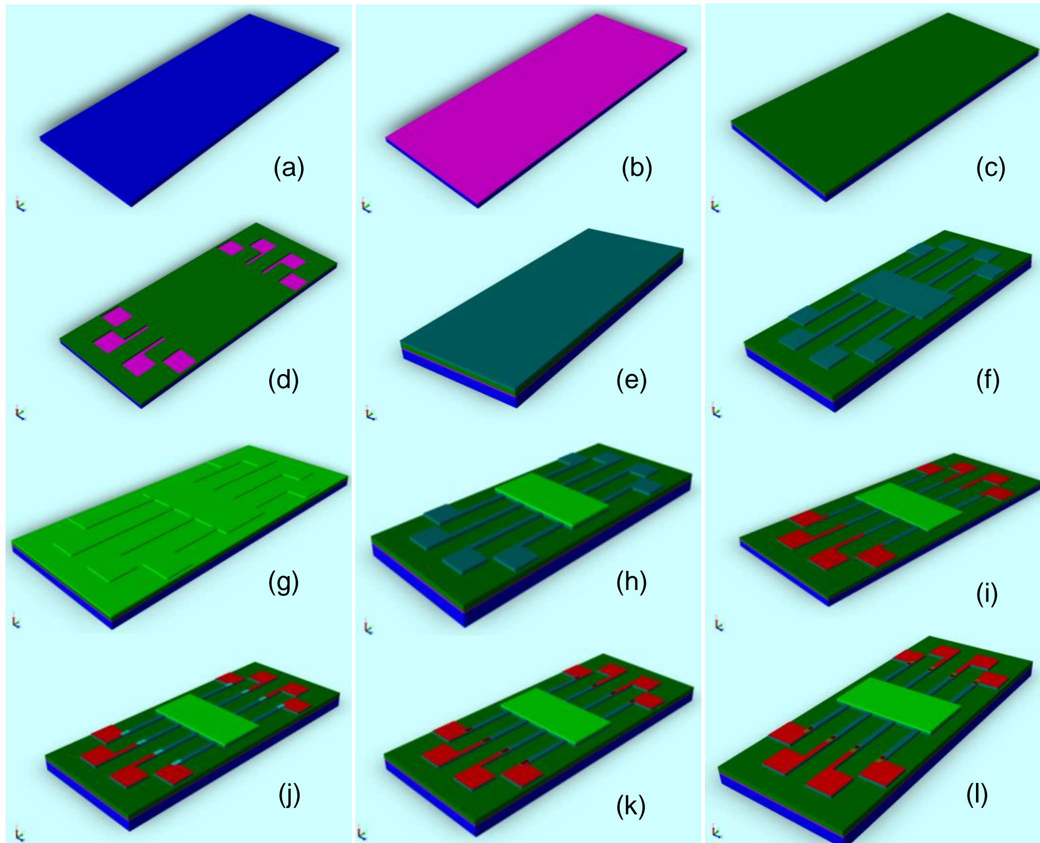

Figure 5.3 Process flow of the MEMS accelerometer design in preprocessor (a) Silicon Substrate layer (b) deposition of passivation (Si_3N_4) layer (c) deposition of polyimide layer (d) Pattering of polyimide layer using negative photoresist to achieve the anchor region (e) deposition of Al_2O_3 and planarization (f) pattering of Al_2O_3 layer using positive photoresist to achieve the dimension of anchor, spring and proof mass (g) electroplating of Tungsten metal (h) pattering of Tungsten layer to get an additional proof mass (i) deposition and patterning of Ti film as bottom electrode (j) deposition and pattering of AlN film as piezoelectric layer (k) deposition and pattering of Ti as the top electrode (l) deposition and pattern of Al_2O_3 insulation layer to prevent short between electrodes.

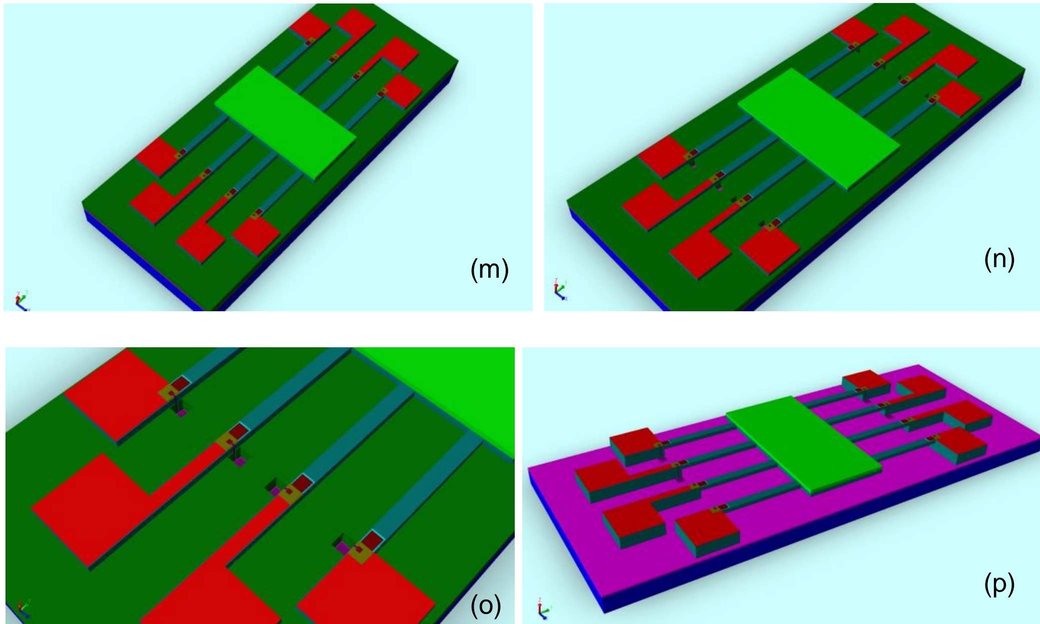

Figure 5.4 (m) Etch hole in the Al_2O_3 layer to release an opening for the metallization wiring (n) pattern of polyimide layer again to release opening for the wiring and contact pad (o) Aluminum deposition and lift off for the metallization layer and contact pad (p) Removal of polyimide sacrificial layer by plasma ashing to make the springs and proof mass structures suspended.

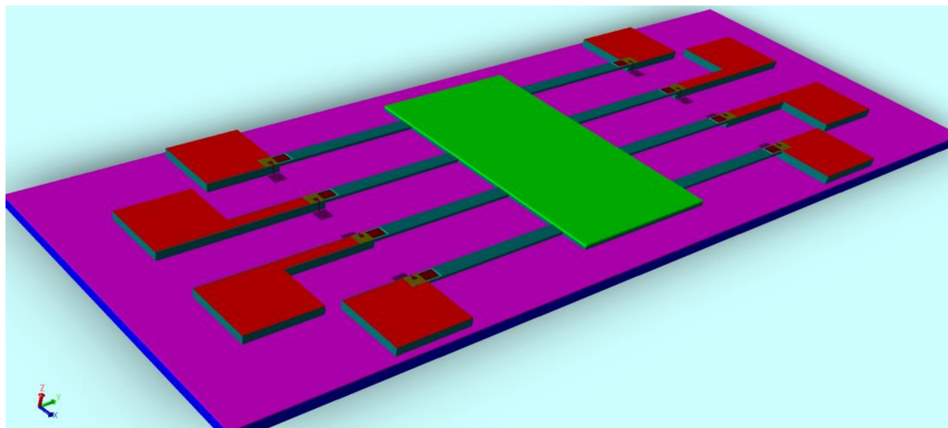

Figure 5.5 Full view of the completed accelerometer

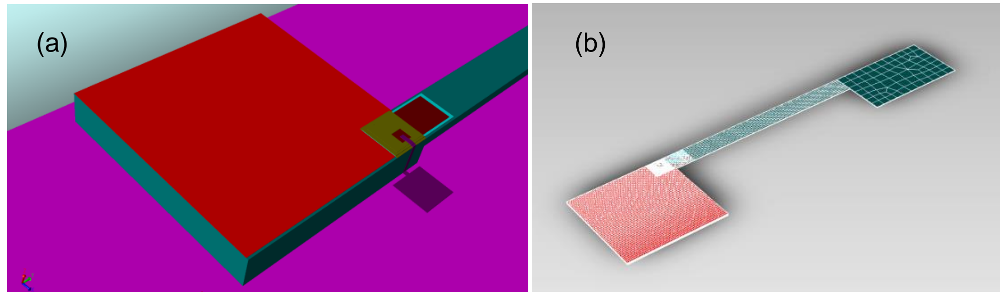

Figure 5.6 (a) zoomed view of an anchor and adjacent layers and (b) Meshed model (partial view).

5.2.4 Mesh Convergence

Mesh study is shown for this design in the Table 5.3. After the coarse mesh, finer mesh is done in the spring and tri layer stack (Ti/AlN/Ti) for mesh convergence. Three different mesh types are used for the mesh study; these are: Manhattan bricks, extruded bricks, and tetrahedron. The following table shows the mesh study in details.

Table 5.3 Parameters for different layers of the accelerometer for mesh convergence

Layer Name	Material	Mesh Type	Mesh Size (μm)
Anchor and spring	Aluminum oxide	Manhattan bricks	(x,y,z) direction=(10,6.25,1)
Proof mass	Aluminum oxide	Extruded bricks	Planer direction (x, y) =(50,50), Extruded direction, z =0.5
Proof mass	Tungsten	Extruded bricks	Planer direction (x, y) =(50,50), Extruded direction, z =0.5
Top electrode	Titanium	Manhattan bricks	(x,yz) direction = (10, 6.25,0.01)
Bottom electrode	Titanium	Manhattan bricks	(x,yz) direction = (10, 6.25,0.01)
Piezoelectric Layer	Aluminum nitride	Manhattan bricks	(x,yz) direction = (10, 6.25,0.01)
Insulation between electrodes	Aluminum oxide	Tetrahedrons	5.0
Contact pad and wiring	Aluminum	Tetrahedrons	2.5

5.3 Simulation and modeling Results

5.3.1 Modal Harmonic Analysis

From the simulation, assuming a damping ration of 0.1 (i.e., underdamped condition), mechanical quality factor is found. The quality factor is found to be 5.0 and the

value is unit less. From the modal harmonic analysis, the bandwidth is also calculated. Figure 5.7 and Figure 5.8 shows the type of modal oscillation and the modal frequencies from the modal harmonic analysis. The spring constant is also found from the simulation results and spring constant, $k=\omega_0^2 m=30.18$ N/m for the total no of springs. But, for a single spring, it is 3.77 N/m. Table 5.4 shows different modal frequency and corresponding mass of the accelerometer.

Table 5.4 Modal frequencies from simulation

Mode no	Modal frequency (kHz)	Gerneralized mass (Kg)
1	2.26	1.49×10^{-7}
2	2.69	5.27×10^{-8}
3	7.86	4.86×10^{-8}
4	13.50	3.92×10^{-8}
5	17.07	2.60×10^{-8}
6	33.52	2.33×10^{-8}

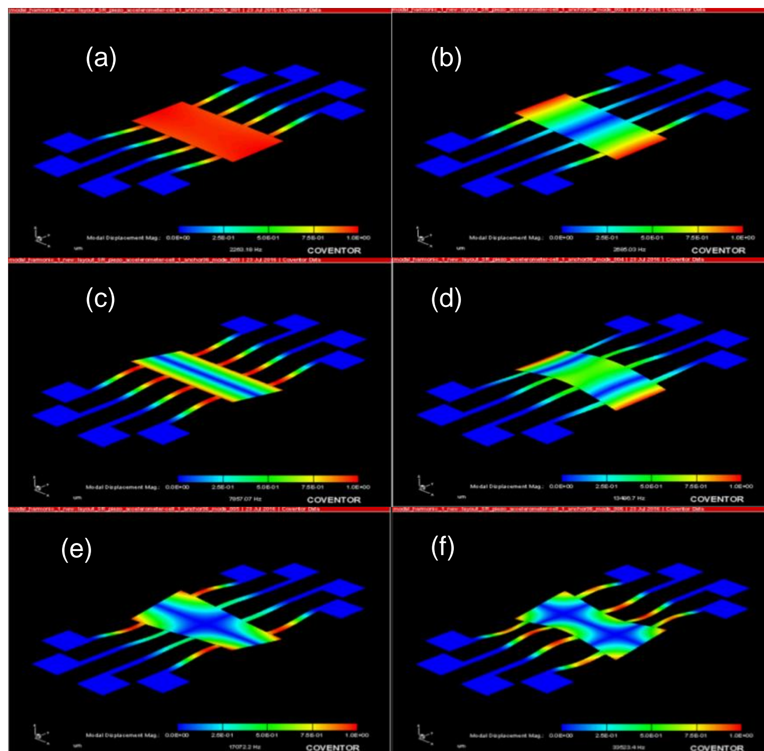

Figure 5.7 Modal harmonic analysis

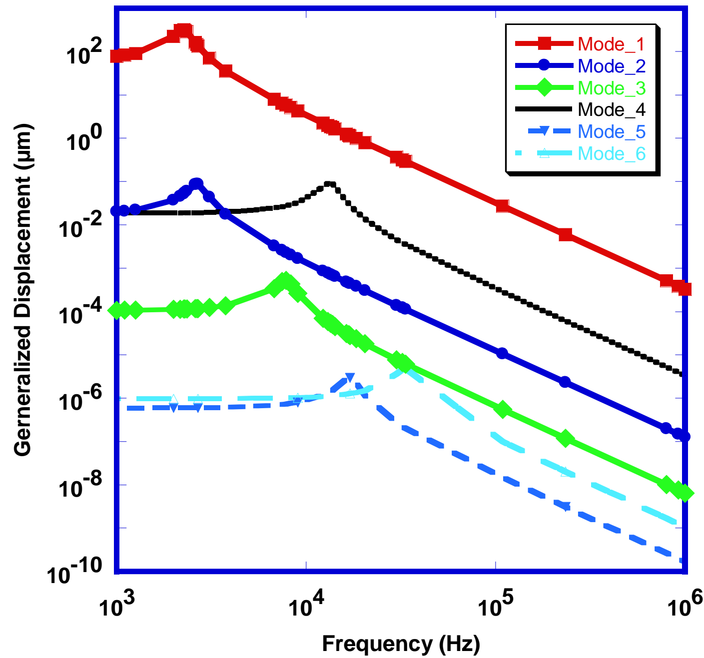

Figure 5.8 Modal frequencies versus displacements from modal harmonic analysis.

5.3.2 Stress analysis

From the stress analysis, it seems that all the Mises stresses of different materials are very much lower than their corresponding yield or tensile strength. The tensile yield strength for Tungsten was reported 1700 MPa [93] which is very much higher than the maximum Mises stress found in the simulation. For Al_2O_3, AlN, Ti, and Al, the tensile strength, compressive strength and/or yield strength are well above than their corresponding Mises stress found from the simulation [46,47,49,67]. The following table maximum Mises stress of the device is 2.212 MPa at 10g acceleration which means the accelerometer can be operated at higher acceleration also without any mechanical difficulty. Figure 5.9 shows the Mises stress versus loading plot. Table 5.5 shows the obtained data from the simulation for stress analysis.

Table 5.5 Simulated stress analysis of the sensor

Applied Load, g (1g=9.8 ms^{-2})	Maximum Mises stress of the accelerometer, σ_v [MPa]	Mises stress of Tungsten (W), $\sigma_{v(W)}$ [MPa]	Mises stress of Al_2O_3, $\sigma_{v(Al2O3)}$ [MPa]	Mises stress of AlN, $\sigma_{v(AlN)}$ [MPa]	Mises stress of Ti, $\sigma_{v(Ti)}$ [MPa]	Mises stress of Al, $\sigma_{v(Al)}$ [MPa]
1	0.221	0.071	0.221	0.157	0.101	0.0004
2	0.442	0.142	0.442	0.313	0.202	0.0008
3	0.664	0.213	0.664	0.470	0.302	0.0011
4	0.885	0.283	0.885	0.626	0.403	0.0015
5	1.106	0.354	1.106	0.783	0.504	0.0019
6	1.327	0.425	1.327	0.940	0.605	0.0023
7	1.549	0.496	1.549	1.096	0.705	0.0027
8	1.770	0.567	1.770	1.253	0.806	0.0030
9	1.991	0.638	1.991	1.409	0.907	0.0034
10	2.212	0.709	2.212	1.566	1.008	0.0038

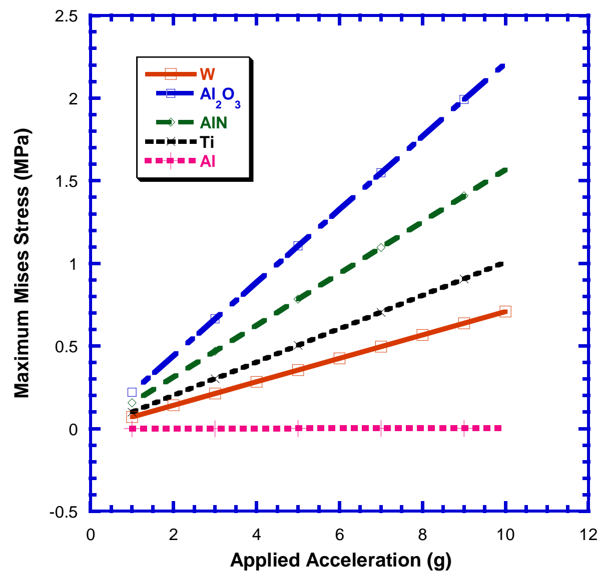

Figure 5.9 Simulated plot of von Mises stress versus acceleration for different materials.

5.3.4 Piezoelectric Response

Maximum stress occurs closer to the anchor and proof mass. For the feasibility of the design, the piezoelectric films are placed where the stresses are higher so that the piezoelectric material can produce sufficient charge or electrical voltage under various acceleration conditions. The red box area in Figure 5.10 shows the relatively higher

stress where the AlN layer is deposited. Once the acceleration is applied, the AlN thin film produces charge due to piezoelectricity. Using piezoelectric theory discussed in chapter 2 (two) along with the simulation results, piezoelectric peak-to-peak voltage is calculated for various acceleration shown in Table 5.6. After that, piezoelectric sensitivity is calculated and found to be 82.1 μV/g. Figure 5.11 shows calculated output voltage corresponding to various acceleration.

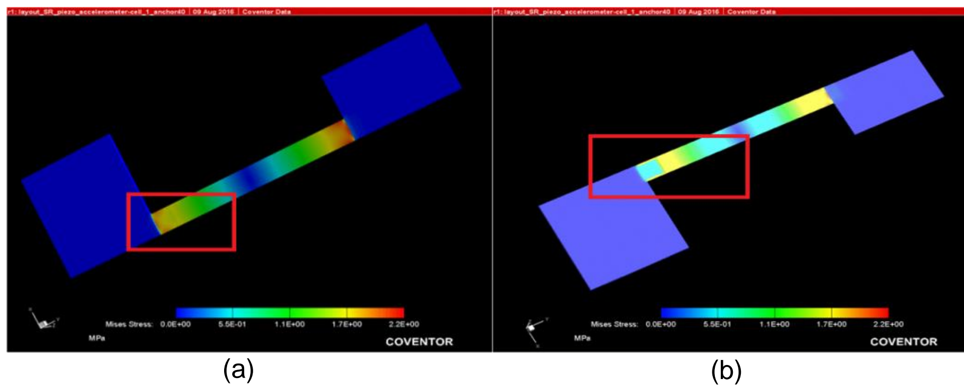

(a) (b)

Figure 5.10 Visualizer stress contour from CoventorWare®.

Table 5.6 Calculation of piezoelectric Response of the accelerometer

Applied Load, A (g)	Charge Produced in the AlN film, Q [fC]	Capacitance, C [pF]	Piezoelectric Voltage, V [V]	Piezoelectric sensitivity, S_a (μV/g)
1	0.35	4.34	0.00008	82.1
2	0.71	4.34	0.00016	82.1
3	1.07	4.34	0.00025	82.1
4	1.43	4.34	0.00033	82.1
5	1.78	4.34	0.00041	82.1
6	2.14	4.34	0.00049	82.1
7	2.49	4.34	0.00057	82.1
8	2.85	4.34	0.00066	82.1
9	3.21	4.34	0.00074	82.1
10	3.56	4.34	0.00082	82.1

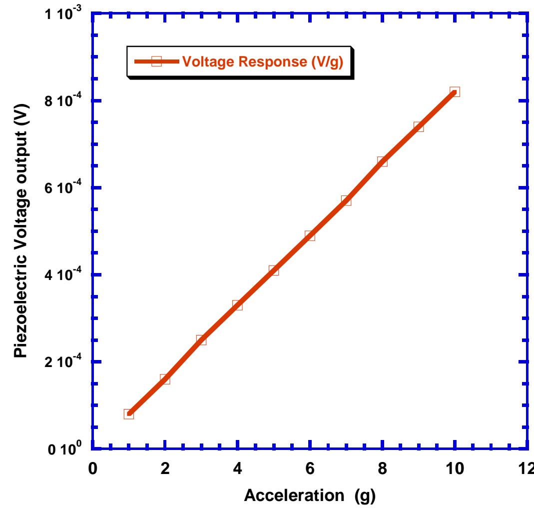

Figure 5.11 Piezoelectric voltages versus acceleration plot from simulation and modeling.

5.4 Noise Analysis

5.4.1 Johnson noise

For a low frequency response where $f \rightarrow 0$, the power spectral density for Johnson noise voltage is, $S_v(f) = 4K_BTR$. On the other hand, for a high frequency response, $S_v(f) = \frac{4K_BTR}{1+(2\pi fRC)^2}$; where, $S_v(f)$ is the power spectral density, R is the electrical resistance of the sensing element, C is the capacitance of the sensing element, T is the absolute temperature (or room temperature), and K_B is the Boltzmann's constant. The values of the parameters are shown in the following Table 5.7.

Table 5.7 Calculated parameters for Johnson noise spectra

Resistivity of AlN, ρ (Ω-m)	Area of AlN film, A (m^2)	Length of the AlN film for charge flow, L (m)	Resistance of the sensing element , R (Ω)	Capacitance of the sensing element, C (F)	Time constant for a parallel RC circuit, τ (s)
10×10^9	1.80×10^{-8}	2.0×10^{-7}	1.11×10^{11}	4.34×10^{-12}	0.4822

After that, Johnson noise voltage or current can be calculated by the following equations. For Johnson noise voltage, $v_{JN} = \sqrt{S_v}$ and for Johnson noise current, $i_{JN} = \frac{v_{JN}}{R}$. Figure 5.12 shows the Johnson noise current spectra with respect to frequency. The value of the Johnson noise current at low frequency (e.g., where f≈0) is found to be 3.86×10^{-16} A.

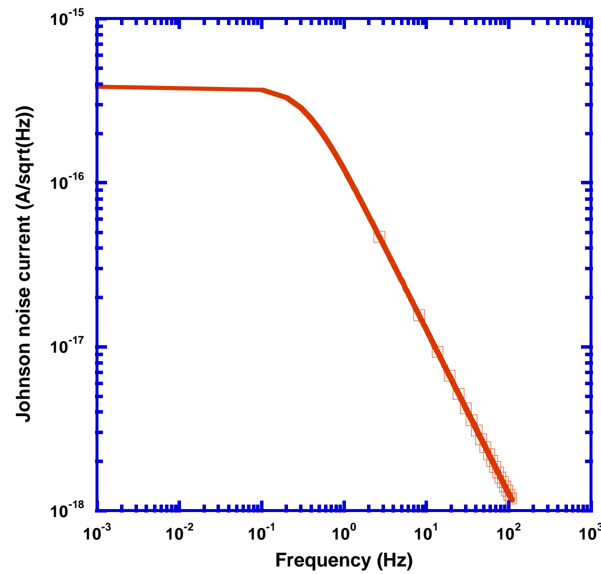

Figure 5.12 Johnson noise current spectra from calculated data

5.4.2 Thermo-mechanical noise

Gabrielson [94] described an expression for the SNR of the accelerometer system:

$$SNR = \frac{a^2 mQ}{4k_B T\omega_0} \tag{5.4}$$

Where, a=input acceleration, k_B=Boltzmann constant, T=absolute temperature, ω_0=angular resonant frequency, m=seismic mass, Q=quality factor

The desired detection level or minimum detection level, a_n can be achieved by setting SNR=1.

$$a_n = \sqrt{\frac{4k_B T\omega_0}{mQ}} \tag{5.5}$$

For a system that is oscillating, damping occurs and in this case squeeze film damping kicks in when since the system is oscillating vertically and the relation between damping coefficient and quality factor is given below:

$$b = \frac{m\omega_0}{Q} \tag{5.6}$$

Where, b= damping coefficient of the damping force.

By using equation (5.5) and (5.6), we get the following form,

$$a_n = \frac{\sqrt{4k_B Tb}}{m} \tag{5.7}$$

The equation is valid at the frequencies less than the resonant frequency. However, the corresponding noise voltage and noise current in an accelerometer due to the damping are also calculated [95].

$$v_{TMN} = \sqrt{\frac{4k_B Tb}{m^2} S_a^2} \tag{5.8}$$

$$i_{TMN} = \frac{v_{TMN}}{R} \tag{5.9}$$

Where, S_a=calculated sensitivity of the accelerometer and R= electrical resistance of the active or sensing part of AlN film.

To get the value of noise current, first we need to calculate the damping coefficient of the accelerometer. For a mass spring damper system, the free vibration frequency is given as:

$$\omega_0 = \sqrt{\frac{k}{m}} \quad (5.10)$$

A very important aspect that is used in analyzing the damping effect is the cutoff frequency. It is usually defined as the frequency when the elastic force equals the damping force. The expression is given by the following:

$$\omega_c = \frac{\pi^2 h_0^2 p_a}{12\mu w^2} \quad (5.11)$$

As per the device specification, the above parameters are known and given below:

h_0=the air gap film thickness=10 μm=10×10^{-6} m

P_a=the ambient pressure=0.1013 MPa=0.1013×10^{6} Pa

w=width of the structure=1000 μm=1000×10^{-6} m

μ=coefficient of viscosity=1.86×10^{-11} Kg/μms=1.86×10^{-5} kg/ms

π =3.1416

Using equation (5.11), we get, angular cut off frequency, ω_c=4.48×10^{5} rad/s whereas the angular resonant frequency, ω_0=1.42×10^{4} rad/s

For MEMS devices with high sensitivity, the resonance frequency is typically low and from the calculated data, it is also observed that $\omega_c \gg \omega_0$.

In this circumstance, the coefficient of damping force is assumed to be constant and the gas or air film is assumed to be incompressible because the squeeze action is a slow process and there is sufficient time for the gas to escape. In that case the damping ratio is given as:

$$\xi = \frac{b}{2m\omega_0} \quad (5.12)$$

Where, ξ= the damping ratio. Any system that falls under the above given condition related to mechanical damping i.e., equation (5.12) is assumed to be,

1. *under damped if ξ<1,*
2. *over damped if ξ>1 and*
3. *critically damped if ξ=1.*

As per the damping ratio, a critically damped system comes to rest as fast as possible without being oscillated. For an over damped system, it takes longer to come to rest than critically damped system without oscillating. As of under damped system, it continues to oscillate at its natural damped frequency and gradually comes to rest position. The optimum damping is achieved when damping ratio, $\xi \approx 0.707$ [96],[97]

The thermo-mechanical noise current can be found using equation (5.8), (5.9), and (5.12). The following table shows the calculation of minimum desired detection level or resolution and the corresponding thermo-mechanical noise current.

Table 5.8 Calculated results for thermomechanical noise current (assuming ξ=0.707 and T=300 K)

Resonant frequency, f_0 (Hz)	Circular resonant frequency, ω_0 (rad/s)	Mass, m (Kg)	Damping ratio, ξ	Damping Coefficient, b (N s/m))	Minimum detection level, a_n (g/√Hz)	Bandwidth, Δf (Hz)	Noise current, i_{TMN} (A/√Hz)
2.26×10^{3}	1.42×10^{4}	1.49×10^{-7}	0.707	3.0×10^{-3}	4.82×10^{-6}	2.26×10^{3}	3.56×10^{-21}

For the accelerometer designed in this work, the corresponding thermo-mechanical noise current is calculated by calculating the damping coefficient using the following equation [96]

$$D_{sfd} = \frac{\mu_{eff} l_{eff} w_{eff}^3}{h_0} \beta\left(\frac{w_{eff}}{l_{eff}}\right) \quad (5.13)$$

Where, D_{sfd}= Damping coefficient of damping force due to squeeze film damping

μ_{eff}=effective gas viscosity

l_{eff}=effective length of the membrane= 2000×10^{-6} m

w_{eff}=effective width of the membrane= 1000×10^{-6} m

$\beta(\frac{w_{eff}}{l_{eff}})$=a function of l_{eff} and w_{eff}

h_0=static air gap between the membrane plate and the surface of the passivation layer=10×10^{-6} m.

Effective gas viscosity, μ_{eff} and factor $\beta(\frac{w_{eff}}{l_{eff}})$ are, however, described by the following equations.

$$\mu_{eff} = \frac{\mu}{1+9.638K_n^{1.159}} \quad (5.14)$$

$$\beta\left(\frac{w}{l}\right) = \left\{1 - \frac{192}{\pi^5}\left(\frac{w}{l}\right)\sum_{n=1,3,5}^{\infty}\frac{1}{n^5}\tanh\left(\frac{n\pi l_{eff}}{2w_{eff}}\right)\right\} \quad (5.15)$$

Where, K_n=λ/h_0=Knudsen number and λ =mean free path of gas molecules. Once D_{sfd} is calculated using equation (5.13), (5.14), and (5.15), and noise equivalent acceleration, noise voltage, and noise current can be calculated by equation (5.7), (5.8), and (5.9), respectively. Table 5.9 shows the results obtained by this theoretical approach in order to find thermomechanical noise current.

Table 5.9 Calculated results of thermo-mechanical noise current (assuming, T=300 K)

Mean free path, λ (m)	Effective gas density, μ_{eff} (Kg/ms)	K_n	$\beta\left(\frac{w}{l}\right)$	Damping coefficient, D_{sfd} (N.s/m)	Minimum detection level, a_n (g/√Hz)	Noise equivalent voltage, v_{TMN} (V/√Hz)	Noise equivalent current, i_{TMN} (A/√Hz)
6.70×10^{-8}	1.81×10^{-5}	6.70×10^{-3}	0.6861	2.48×10^{-2}	1.38×10^{-5}	1.14×10^{-9}	1.02×10^{-20}

5.4.3 Loss tangent or tanδ noise

In dissipation or lossy medium, the loss tangent of AlN film is approximately 0.0026 [71] at 1000 Hz. Since, the sensing element has resistance, R and capacitor, C in parallel; therefore, the equivalent AC resistance will be different than equivalent series resistance associated with a capacitor. For a parallel combination of R and C, the tanδ equation becomes,

$$tan\delta = \frac{X_C}{R_{ac}} \quad (5.16)$$

Or, $$R_{ac} = \frac{X_C}{\tan\delta} \quad (5.17)$$

Where, X_c =capacitive reactance or pure capacitive impedance= $\frac{1}{\omega C}$ and R_{ac}=AC resistance of the AlN film.

Therefore, the noise current involving the tanδ noise is,

$$i_{tan\delta} = \sqrt{\frac{4k_BT}{R_{ac}}} \quad (5.18)$$

For higher frequency operation, the tanδ noise becomes,

$$i_{tan\delta} = \sqrt{\frac{4k_BT}{R_{ac}(1+(2\pi f R_{ac}C)^2)}} \quad (5.19)$$

Using equation (5.16)-(5.19), the noise current related to loss tangent is calculated. The following table shows the calculation results. Figure 5.13 shows the tanδ noise in the frequency domain.

Table 5.10 parameters and calculation of loss tangent noise current (Assuming T=300 K)

tanδ at 1000 Hz	Capacitance of sensing element, C (F)	Reactance corresponding to capacitance, X_c (Ω)	AC resistance, R_{ac} (Ω)	Noise current, $i_{tan\delta}$ (A)
0.0026	4.34×10^{-12}	3.67×10^{7}	1.41×10^{10}	1.08×10^{-15}

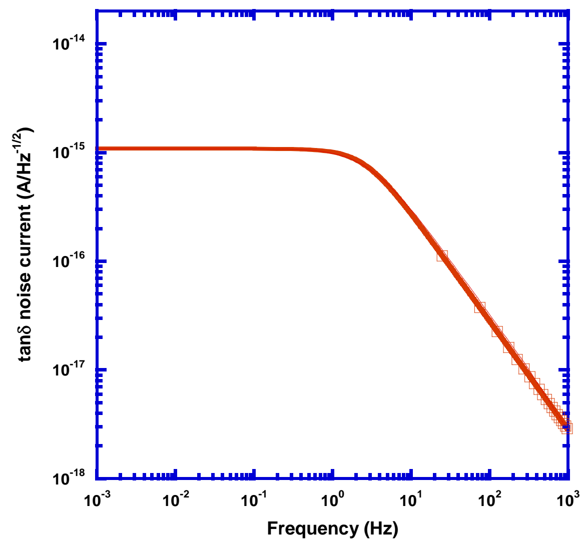

Figure 5.13 tanδ noise current spectra of the accelerometer from calculated data

5.4.4 Total noise current

The total noise current is expressed by the following equation while frequency is assumed to be very in this case (i.e., f≈0),

Total rms noise current (at low frequency) =√(Johnson noise current+ thermo-mechanical noise current+ loss tangent noise current)

Or, $$i_n = \sqrt{({i_{JN}}^2 + {i_{TMN}}^2 + {i_{tan\delta}}^2)} \quad (5.20)$$

Or, $$i_{n=}\sqrt{(3.86 \times 10^{-16})^2 + (1.02 \times 10^{-20})^2 + (1.08 \times 10^{-15})^2} \quad [\frac{A}{\sqrt{Hz}}]$$

$$i_n = 1.47 \times 10^{-15}\ A/\sqrt{Hz}$$

Clearly, the Johnson noise current and tanδ noise current dominate over thermo-mechanical noise current.

Figure 5.14 shows the total noise current and individual noise current in frequency domain.

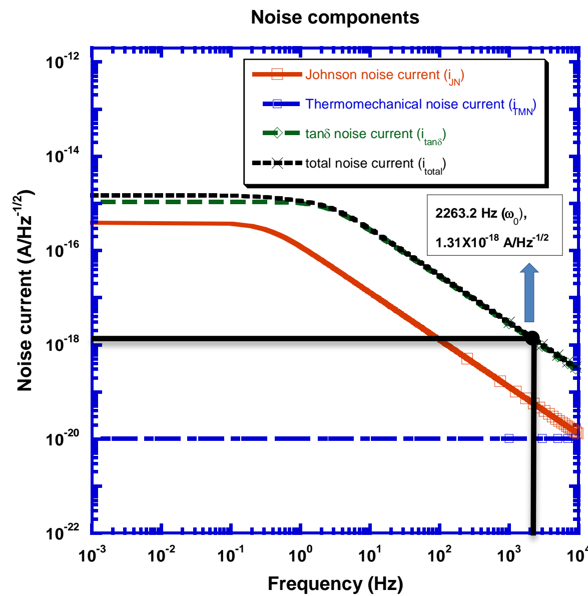

Figure 5.14 Total noise current and individual noise currents from calculated data

The total rms noise current at the resonant frequency is 1.31×10^{-18} A/Hz$^{-1/2}$. The total noise voltage at low frequencies (i.e., $\omega<<\omega_0$) is found to be 2.07×10^{-5} V/√Hz. Therefore, total noise equivalent acceleration (NEA) is,

$$Total\ noise\ equivalent\ acceleration = \frac{total\ noise\ voltage\ (V_{TN})}{Piezoelectric\ response\ (S)}$$

$$NEA\ (\omega_0 \approx 0) = \frac{2.07 \times 10^{-5}}{8.20 \times 10^{-5}} = 0.253\ g/\sqrt{Hz}$$

Here, the discussion was made considering only one spring. However, there are 8 springs as well as 8 sensing elements. If the sensing elements are connected in series, the voltage sensitivity will improve 8 times than for the single sensing element. So, NEA will become 8 times lesser (i.e., 31.6×10^{-3} g/√Hz) than what has been achieved for single sensing element.

However, there are several ways to further optimize the NEA of the accelerometer. They are as follows:

1. By reducing the thickness of the sensing element a little further
2. By increasing the area of the sensing element.
3. By adding more spring thus more sensing element to improve sensitivity thus reducing NEA.
4. The desired operating acceleration for the designed accelerometer is ranged very high (i.e., 10g ~200g), therefore, the NEA effect is very minimum for the designed accelerometer.

5.5 Conclusions

A novel MEMS piezoelectric accelerometer using piezoelectric, CMOS compatible, ultrathin AlN film was designed and modeled using FE analysis software CoventorWare®. 200 nm thick AlN film was used as the piezoelectric layer or sensing

layer and was sandwiched between top and bottom electrodes. Tungsten and Al_2O_3 were used as the proof mass elements; especially, tungsten was used to increase the mass density of the proof mass. Polyimide layer which was later removed was used as the sacrificial layer to release the proof mass structure. Eight springs were used to support the proof mass. Each spring was 1000 μm long and 100 μm wide. The desired resonant frequency of the accelerometer was 2 kHz~3 kHz for specific applications such as automobile and aircrafts. The designed resonant frequency from the modal analysis was found to be 2.26 kHz. The modal harmonic analysis showed that the amplitude of mode 1 is very high compared to the other modal frequencies. However, mesh convergence study was investigated before the mechanical analysis. Stress analysis was also carried out for each material to check if the maximum stress occurred by the material were under the mechanical strength limit i.e., yield/tensile/compressive strength, of the corresponding material. In the mechanical analysis, different acceleration were applied on the accelerometer and corresponding stress contour results were used to calculate the charge density, hence, total charge in a single piezoelectric element. The charge is generated due to piezoelectric nature of the AlN film. The charge from each AlN sensing element is then converted to voltage. There were total eight sensing element or AlN films but for the simplicity of the simulation, the simulation and voltage calculation was done for only one piezoelectric element. Since, all the springs and sensing elements were identical, therefore, they are considered to provide identical voltage response upon acceleration. The metal bond pads for each sensing elements were considered to be in parallel so that total voltage due to acceleration force would remain same but the currents added up and the total current from the accelerometer should be 8 times the current found in a single sensing element. However, the calculated voltage sensitivity was found to be 82.1 μV/g which was relatively higher than the reported sensitivities of the most of

the AlN based piezoelectric accelerometers. Since, the device size and volume also matter for the sensitivity, therefore, sensitivity densities were compared with the reported results instead of sensitivity itself. Finally, different types of noise were investigated at room temperature i.e., T=300 K. Minimum detectable noise level acceleration was calculated and found be to be 1.38×10^{-5} g/√Hz. The Johnson noise current from the calculation was 3.86×10^{-16} A/√Hz whereas tanδ noise current was 1.08×10^{-15} A/√Hz. The total noise current was found to be 1.47×10^{-15} A/√Hz. From the noise versus frequency plot, it is apparent that the tanδ noise dominates over the Johnson noise and thermomechanical noise at low frequencies. With the increase of frequency, both Johnson noise and tanδ falls off. From Figure 5.12, it is observed that thermomechanical noise does not contribute much toward the total noise current. For the calculation of the thermomechanical damping in optimum condition, the system is considered to be under damped where the damping ratio was considered 0.707. The overall total noise current starts to decrease with the increase of frequency. The calculated bandwidth of the accelerometer was considered to be 2.26 kHz. Total noise equivalent acceleration of the accelerometer was found to be 0.253 g/√Hz. The NEA can be improved in several ways which was discussed in the noise analysis section of the chapter.

Chapter 6

Conclusions

Ultrathin (200 nm~300 nm) AlN based flexible MEMS sensors have been investigated. Because of its piezoelectric property, AlN film is an excellent choice as sensing element for MEMS sensors. The advantages and disadvantages of different piezoelectric materials such ZnO, PZT and AlN have been discussed. Though, PZT has higher piezoelectric coefficient than AlN and ZnO, however, for sensor applications AlN is more suitable than PZT and ZnO. For fabrication, it is easy to fabricate AlN thin film than PZT or ZnO. One of the biggest advantages of AlN film is that, it is CMOS compatible which makes it stands out than the other piezoelectric sensing materials. Moreover, other sensing techniques such as capacitive sensing method costs more than AlN based sensing because capacitive technique requires an additional voltage source for biasing.

First, 300 nm thick AlN based cantilever pressure sensors have been designed, fabricated, characterized, and modeled. Flexibility of the cantilever sensors was investigated. The experimental results and numerical modeling results showed that they were in good agreement with each other. DC magnetron sputtering was applied for the deposition of AlN film at 300 ºC. Characterization results of the developed AlN film such as SEM, XRD, and EDX resulted in similar results compared to the reported works by other authors. Calculated radius of curvature of the cantilever showed great promise about flexibility or bendability of AlN thin film. Stress analysis was also done to calculate the voltage response from simulated stress data as well as to observe the mechanical strength of the cantilever sensors. Several cantilevers were characterized for electrical testing. Piezoelectric voltage and power spectral density were measured from dynamic signal analyzer. The experimental output voltage ranged from 4.48×10^{-4} V to 5.66×10^{-6} V whereas the numerically modeled piezoelectric voltage results ranged from 1.16×10^{-4} V

to 4.16×10^{-5} V which are in good agreement with the experimental results. Piezoelectric response was also calculated from the simulated results. Response varied between 66.5 V/N to 41.2 V/N which proves that the ultrathin AlN film can be of great use for flexible MEMS sensor applications.

Second, ultrathin, 200 nm thick AlN film was used as sensing element to design novel piezoelectric MEMS sensors for high resolution fingerprint sensing applications. Three different fingerprint sensors with pixel resolution of 725 dpi and 1016 dpi were designed and their corresponding piezoelectric responses were calculated based on simulation and electrical modeling. The calculated piezoelectric voltage response with applied force for FPS725A, FPS725B, and FPS1016 fingerprint sensors were 225.74 V/N, 115.58 V/N, and 125.52 V/N, respectively. Noise analysis was carried out for FPS725B and FPS1016. Noise equivalent currents and noise equivalent pressures were also calculated for the sensors. The values of rms noise equivalent current (NEC) and noise equivalent pressure (NEP) for FPS725B were found to be 2.16×10^{-16} A/√Hz and 1.82×10^{3} Pa/√Hz, respectively. For FPS1016, the values of NEC and NEP were 1.30×10^{-16} A/√Hz and 5.50×10^{3} Pa/√Hz, respectively. NEP of the sensors can be improved by optimizing the geometry of the sensing elements. Comparing the voltage sensitivities with applied pressure between FPS725B and FPS1016, it is apparent that reduction of pixel size or improvement of pixel resolution reduces the response to some extent with applied pressure. On the other hand, the stress analysis results between them show that FPS1016 produces lesser stress in the sensor than FPS725B while both the sensors seem to be sustainable when operated beyond the maximum range of regular or practical finger pressure (i.e., 0.6 MPa) which guarantees the mechanical stability of the sensors in harsh conditions.

Third, ultrathin AlN film (200 nm) based MEMS accelerometer was designed and modeled. The desired resonant frequency was targeted in the range between 2.0 kHz~3.0 kHz for very low to high frequency based applications of MEMS accelerometers such as for airbag applications in automobiles, aircrafts, and satellites. Mesh convergence was investigated for the design before any mechanical simulation. Modal harmonic analysis was run to observe the first modal resonant frequency of the device and it was found to be 2.26 kHz while other modal frequencies were ignored since they showed less strength in amplitude (i.e., displacement, velocity, and acceleration amplitude). One of the important features of the design was the use of Tungsten (W) as the proof mass material which reduces the device size by a large scale without affecting the performance of operation. W is a material which possess larger volume mass density than most of the materials, therefore, it has the potential to reduce the manufacturing cost. Mechanical analysis showed that the maximum stresses of the accelerometer at various acceleration (i.e., 1g to 10g) were well below the mechanical strength or yield strength of the device which sufficed the purpose of the design. It means the accelerometer can be operated for very high g operation, for example, between 10g to 200g. Using the same piezoelectric theory discussed in chapter 2, the piezoelectric voltages were calculated for various acceleration. Sensitivity or piezoelectric response was also calculated and the value was found to be 82.1 μV/g. Noise analyses was investigated and the total noise current was found to be 1.47×10^{-15} A/√Hz. Total noise equivalent acceleration(NEA) was also calculated and found to be 0.253 g/√Hz. The noise equivalent acceleration can be optimized further which was discussed in noise analysis section of chapter 5.

For future work, the performance of the designed and electrically modeled fingerprint sensors and accelerometer can be understood further and in an extensive

manner once fabrication and experimental characterization are made and compared with the theoretical analysis. The discussion above regarding each project shows that ultrathin AlN film has the tremendous potential to be the future of MEMS based sensor applications that are flexible, CMOS compatible and can be integrated with microelectronics on a single chip. MEMS packaging needs to be carried out for further improvement on the works of the dissertation.

References

[1] T.-R. Hsu, “Overview of MEMS and Microsystems,” in MEMS and Microsystems Design and Manufacture, New York, NY: McGraw-Hill, 2002, pp. 1-33.

[2] P. Muralt, J. Antifacos, M. Cantoni, R. Lanz, and F. Martin, “Is there a better material for thin film BAW applications than AlN ?”, IEEE Ultrasonics Symposium 1, pp. 315-320, 2005.

[3] A. Choujaa, N. Tirole, C. Bonjour, G. Martin, D. Hauden, P. Blint, A. Cachard, and C. Pommier, “AlN/silicon lamb-wave microsensors for pressure and gravimetric measurements”, Sensors and Actuators A 46-47, pp.179-182, 1995.

[4] M. Clement, L. Vergara, J. Sangrador, E. Iborra, and A. Sanz-Hervas, “SAW characteristics of AlN films sputtered on silicon substrate”, Ultrasonics 42, pp. 403–407, 2004.

[5] J. H. Kim, S. H. Lee, J. H. Ahn, and J. K. Lee, “AlN piezoelectric materials for wireless communication thin film components”, *Journal of Ceramic Processing Research* 3 (1), pp. 25–28, 2002.

[6] D. A. Dubois and P. Muralt, “Properties of AlN thin films for piezoelectric transducers and microwave filter applications”, *Applied Physics Letters 74* (20), pp. 3032-3034, 1999.

[7] S. Tadigadapa and K. Mateti, “Piezoelectric MEMS sensors: state-of-the-art and perspectives”, *Meas. Sci. Technol.*,vol. 20, pp. 1-30, 2009.

[8] E. Kalvesten, L. Smith, L. Tenerz, and G. Stemme, "The first surface micromachined pressure sensor for cardiovascular pressure measurements." The Eleventh Annual International Workshop on. Micro Electro Mechanical Systems, IEEE, 1998.

[9] V. Kutiš, J. Dzuba, J. Paulech, J. Murin, and T. Lalinsky, "MEMS piezoelectric pressure sensor-modeling and simulation", *Procedia Engineering*, pp. 338 -345, 2012.

[10] W. Zhou, A. Khaliq, Y. Tang, H. Ji, and R. R. Selmic, "Simulation and design of piezoelectric microcantilever chemical sensors", *Sensors and Actuators A*, pp. 69–75, 2005.

[11] M. Baù, M. Ferrari, E. Tonoli, and V. Ferrari, “Sensors and energy harvesters based on piezoelectric thick films ", Proc. Eurosensors XXV, Athens, Greece, pp. 737-744, 2011.

[12] F. Gerfers, P. M. Kohlstadt, E. Ginsburg, M. Y. He, D. Samara-Rubio, Y. Manoli, and L. Wang, "Sputtered AlN Thin Films for Piezoelectric MEMS Devices - FBAR Resonators and Accelerometers", Solid State Circuits Technologies, INTECH, Croatia, ISBN 978-953-307-045-2, pp. 462, 2010.

[13] K.M. Lakin, K. T. McCarron, and J. F. McDonald, "Temperature Compensated Bulk Acoustic Thin Film Resonators", Proc. IEEE Ultrasonics Symposium, pp. 855–858, 2000.

[14] S. Trolier-Mckinstry and P. Muralt, "Thin Film Piezoelectrics for MEMS", Journal of Electroceramics, vol 12, pp. 7–17, 2004.

[15] F. Gerfers, P. M. Kohlstadt, E. Ginsburg, M.Y. He, D. Samara-Rubio, Y. Manoli, and L. Wang, "Fabrication and Characterization of Bulk-micromachined Accelerometers Based on AlN Piezoelectric Sensing and SOI Wafers", 20th Eurosensors, 2006.

[16] S. E. Boeshore, “Aluminium Nitride Thin Films on Titanium: Piezoelectric Transduction on a Metal Substrate”, Ph.D. thesis, 2006

[17] S. Gonzalez-Castilla, J. Olivares, E. Iborra, M. Clement, J. Sangrador, J. Malo, and I. Izpura, "Piezoelectric microresonators based on aluminum Nitride for mass sensing applications," in Proc. 2008 IEEE Sensors conf., Lecce, Italy, pp. 486-489, Oct. 2008.

[18] A. Bertacchini, S. Scorcioni, D. Dondi, L. Larcher, P. Pavan, M. T. Todaro, A. Campa, G. Caretto, S. Petroni, A. Passaseo, and M. De Vittorio, "AlN-based MEMS devices for vibrational energy harvesting applications," in 2011 Proc. ESSDERC, Helsinki, Finland, pp. 119-122, Sept. 2011.

[19] G. Ionescu, O. Ionescu, S. Popovici, S. Costea, V. Dumitru, M. Brezeanu, G. E. Stan, and I. Pasuk, "Wireless AIN sensor for condition based monitoring of industrial equipment," 2013 International Semiconductor Conference (CAS), Sinaia , Romania, pp. 55-58, Oct. 2013.

[20] F. Guido, V. M. Mastronardi, M. T. Todaro, S. Petroni, and M. De Vittorio, "Piezoelectric soft MEMS for tactile sensing and energy harvesting," in 2014 IEEE International Conference on IC Design & Technology (ICICDT), Austin, TX, USA, pp. 1-4, May 2014.

[21] E. Defaÿ, "Piezoelectric Formalism," in *Integration of Ferroelectric and Piezoelectric Thin Films*, Hoboken, NJ: Wiley, 2011, pp. 119-141.

[22] S. Kon, and R. Horowitz, "A high-Resolution MEMS Piezoelectric Strain Sensor for Structural Vibration Detection", *IEEE Sensors J.*, vol. 8, no. 12, 2008.

[23] H. Shin, and J. Song, "Piezoelectric coefficient measurement of AlN thin films at the nanometer scale by using piezoresponse force microscopy", *J. Kor. Phys. Society*, vol. 56, no. 2, pp. 580-585, Feb. 2010.

[24] A. Andrei, K. Krupa, M. Jozwik, P. Delobelle, L. Hirsinger, C. Gorecki, L. Nieradko, and C. Meunier, “ AlN as an actuation material for MEMS applications The case of AlN driven multilayered cantilevers”, *Sensors and Actuators A*, 141, pp. 565–576, 2008.

[25] L.-P. Wang, E. Ginsburg, F. Gerfers, D. Samara-Rubio, B. Weinfeld, Q. Ma, V. Rao, and M. Y. He, "Sputtered AlN Thin Films for Piezoelectric MEMS Devices," Proc. 5th IEEE Sensors Conf., Daegu, Korea, pp. 10-13, Oct. 2006.

[26] J. G. Gualtieri, J. A. Kosinski, A. Ballato, “Piezoelectric materials for acoustic wave applications”, IEEE Transactions on Ultrasonics, Ferroelectronics, and Frequency Control, vol. 41, no. 1, pp. 53-59, Jan 1994.

[27] C. Giordano, I. Ingrosso, M. T. Todaro, G. Maruccio, S. De Guido, R. Cingolani, A. Passaseo, and M. De Vittorio, “ AlN on polysilicon piezoelectric cantilevers for sensors/actuators”, *Microelectron. Eng.*, vol 86, no. 4-6, pp. 1204-1207, 2009.

[28] H. –P. Lobl, M. Klee, C. Metzmacher, W. Brand, R. Milsom, P. Lok, and R. Van Straten, “Piezoelectric materials for BAW resonators and filters”, IEEE Ultrasonics Symposium, Atlanta, GA, USA, pp. 807-811, 2001.

[29] F. Goericke, K. Mansukhani, K. Yamamoto, and A. Pisano, "Experimentally validated aluminum nitride based pressure, temperature and 3-axis acceleration sensors integrated on a single chip," 2014 IEEE 27th International Conf. on Micro Electro Mechanical Systems (MEMS), San Francisco, CA, USA, pp. 729-732, Jan. 2014.

[30] R. Elfrink, T. M. Kamel, M. Goedbloed, S. Matova, D. Hohlfeld, Y. van Andel, and R. van Schaijk, “Vibration energy harvesting with aluminum nitride-based piezoelectric devices”, *J. Micromech. Microeng.*, vol 19, no. 09, pp. 1-8, 2009.

[31] R. H. Olsson, K. E. Wojciechowski, M. S. Baker, M. R. Tuck, and J. G. Fleming, “Post-CMOS-compatible aluminum nitride resonant MEMS accelerometers”, *J. Microelec. Syst.*, vol. 18, no. 3, June 2009.

[32] T. Someya, T. Sekitani, S. Iba, Y. Kato, and T. Sakurai, “A large-area, flexible pressure sensor matrix with organic field-effect transistors for artificial skin applications”, Proc. Natl. Acad. Sci U.S.A., vol. 101, no. 27, pp. 9966-9970, Jul. 2004.

[33] S. C. B. Mannsfeld, B. C-K. Tee, R. M. Stoltenberg, C. V. H-H. Chen, S. Barman, B. V. O. Muir, A. N. Sokolov, C. Reese, and Z. Bao, “Highly sensitive flexible pressure sensors with microstructured rubber dielectric layers,” Nat. Mater., vol. 9, no 10, pp. 859-864, Jul. 2010.

[34] T. Yamada, Y. Hayamizu, Y. Yamamoto, Y. Yomogida, A. Izadi-Najafabadi, D. Futaba, and K. Hata, “A stretchable carbon nanotube strain sensor for human-motion detection,” Nat. Nanotechnol., vol. 6, no. 5, pp. 296–301, 2011.

[35] C. M. Nguyen, W.-D. Huang, S. Rao, H. Cao, U. Tata, M. Chiao, and J.-C. Chiao, "Sol-Gel Iridium Oxide-Based pH Sensor Array on Flexible Polyimide Substrate," IEEE Sensors J., vol.13, no.10, pp.3857-3864, Oct. 2013.

[36] W. R. Runyan, Silicon semiconductor technology. McGraw-Hill, 1965.

[37] S. B. Brown, W. Van Arsdell, and Ch. L. Muhlstein, “Material Reliability in MEMS Devices”, TRANSDUCERS’97 International Conference on Solid State Sensors and Actuators 1, pp.591-593, Chicago, June 16-19, 1997

[38] J. W. Judy, “Micromechanical Systems (MEMS): Fabrication, Design, and Applications”, Journal of Smart Materials and Structures 10, pp.1115-1134, 2001.

[39] D. Banks, “Micromachining – Introduction”, Part 1 in “Microengineering, MEMS, and Interfacing. A Practical Guide”, Taylor & Francis Group, CRC Press, Boca Raton 2006.

[40] S. L. Miller, M. S. Rodgers, g. La Vigne, J. J. Sniegowski, P. Clews, D. M. Tanner, and K. A. Peterson, “Failure modes in surface micromachined microelectromechanical actuator systems”, Microelectronics Reliability 39 (8), pp.1229-237, 1999.

[41] D. M. Tanner, N. F. Smith. L. W. Irwin, W. P. Eaton, K. S. Helgesen, J. J. Clement, W. M. Miller, J. A. Walraven, K. A. Peterson, P. Tangyunyong, M. T. Dugger, S. L. Miller, “MEMS Reliability: Infrastructure, Test Structures, Experiments, and Failure Modes”, SANDIA REPORT SAND2000-0091, 2000.

[42] I. De Wolf, “MEMS Reliability”, Microelecronics Reliability 43 (7), pp.1047-1048, 2003

[43] T. Yao, S. Hong, "Oxide and Nitride Semiconductors: Processing, Properties, and Applications", Springer Verlag, Berlin, ISBN-13: 9783540888468, pp. 17-18, 2009.

[44] A. Sanz-Hervas, M. Clement, E. Iborra, L. Vergara, J. Olivares, J. Sangrador, “Degradation of the piezoelectric response of sputtered c-axis AlN thin films with traces of non-(0002) x-ray diffraction peaks”, App. Phys. Lett., vol. 88, 161915, 2006.

[45] M. S. Rayhan, D. P. Butler, and Z. Çelik-Butler, “Ultra-thin Film Piezoelectric AlN Cantilevers for Flexible MEMS Sensors,” in Proc. 2015 IEEE Sensors Conf., Busan, Korea, Nov 1-4, 2015

[46] D. G. Zong, C. W. Ong, and M. Aravind, M. P. Tsang, C. L. Choy, D. Lu and D. Ma, “Tensile strength of aluminium nitride films”, Philosophical Magazine, vol. 84, no. 31, pp. 3353-3373, 2004.

[47] J. W. McCauley, “Structure and Properties of Aluminum Nitride and AlON Ceramics”, no. ARL-TR-2740. Army Research Lab, Aberdeen Proving Ground, Md Weapons and Materials Research directorate, 2002.

[48] G. Welsch, R. Boyer, and E. W. Collings,"Commercially Pure and Modified Titanium" in Materials Properties Handbook: Titanium Alloys, 4th ed., Materials Park: ASM International, 1993, pp 165-262.

[49] H. Ogawa, K. Suzuki, S. Kaneko, Y. Nakano, Y. Ishikawa, and T. Kitahara, "Measurements of mechanical properties of microfabricated thin films," in Proc. 1997 IEEE MEMS Conf., Nagoya, Japan, pp. 430-435, 1997.

[50] R. S. Dahiya and S. Gennaro, "Bendable Ultra-Thin Chips on Flexible Foils,", IEEE Sensors J., vol.13, no.10, pp. 4030-4037, Oct. 2013.

[51] H. Dong, Y. Kervran, N. Coulon, O. De Sagazan, E. Jacques, and T. Mohammed-Brahim, "Highly Flexible Microcrystalline Silicon n-Type TFT on PEN Bent to a Curvature Radius of 0.75 mm," in IEEE Trans. Electron Devices, vol. 62, no. 10, pp. 3278-3284, Oct. 2015.

[52] L. Wang, K.M.B Jansen, M. Bartek, A. Polyakov, and L. J. Ernst, "Bending and stretching studies on ultra-thin silicon substrates," in 2005 6th International Conference on Electronic Packaging Technology, Shenzhen, China, pp. 1-5, Sept. 2005.

[53] N. Bu, M. Ichiki, N. Ueno, O. Fukuda, and M. Akiyama, "A Flexible Piezoelectric Film Sensor for Fault Diagnosis of Pipe Systems," in 33rd Annual Conference of the

IEEE Industrial Electronics Society, 2007, Taipei, Taiwan, pp. 2181-2186, Nov. 2007.

[54] C. J. Zhou, Y. Yang, Y. Shu, C. H. Zhang, H. Tian, Z.H. Zhang, D. Xie, T.L. Ren, J. Zhou, B. Feng, H. Jin, and S. R. Dong, "Ultra flexible pseudo-lamb wave RF resonators based on ZnO/PI and AlN/PI structures," in 2012 IEEE International Electron Devices Meeting (IEDM), San Francisco, CA, USA, pp. 541-544, Dec. 2012.

[55] N. Sato et al., "MEMS fingerprint sensor with arrayed cavity structures," Electron Devices Meeting, 2001. Technical Digest. International, IEEE, Washington, DC, USA, 2001, pp. 41.2.1-41.2.4.

[56] Y. H. Liao et al., "Flat panel fingerprint optical sensor using TFT technology," IEEE Sensors Conf. 2015, Busan, Korea, pp. 1-4, 2015.

[57] F. Alonso-Fernandez, F. Roli, G. L. Marcialis, J. Fierrez, and J. Ortega-Garcia, "Comparison of fingerprint quality measures using an optical and a capacitive sensor," First IEEE International Conference on BTAS 2007, Crystal City, VA, 2007, pp. 1-6.

[58] L. Qiu, "Fingerprint sensor technology," 9th IEEE Conf. on Industrial Electronics and Applications, Hangzhou, 2014, pp. 1433-1436.

[59] B. Charlot, F. Parrain, N. Galy, S. Basrour, and B. Courtois, "A sweeping mode integrated fingerprint sensor with 256 tactile microbeams," *Journal of Microelectromechanical Systems*, vol. 13, no. 4, pp. 636-644, 2004.

[60] M. Damghanian, and B. Y. Majlis, "Analysis and design of a wide micro beam as a pressure gauge for high sensitivity MEMS fingerprint sensors." Mi*crosystem technologies*, vol. 15, no. 5, pp. 731-737, 2009.

[61] J. C. Liu, Y. S. Hsiung and M. S. C. Lu, "A CMOS Micromachined Capacitive Sensor Array for Fingerprint Detection," *IEEE Sensors Journal*, vol. 12, no. 5, pp. 1004-1010, 2012.

[62] B. A. Ganji and M. S. Nateri, "A high sensitive MEMS capacitive fingerprint sensor using slotted membrane", *Microsystem Technologies*, vol. 19, no 1, pp 121-129, 2013.

[63] H. Tang et al., "Pulse-echo ultrasonic fingerprint sensor on a chip," 18th International Conf. on Solid-State Sensors, Actuators and Microsystems (TRANSDUCERS), Anchorage, AK, 2015, pp. 674-677.

[64] S. M. Huang, Y. S. Huang, C. N. Yeh, N. Sugiura, J. Y. You, and C. H. Peng, "Design and modeling of 1000ppi fingerprint sensor," 2015 IEEE SENSORS, Busan, Korea, pp. 1-3, 2015.

[65] W. Scott and D. Jones “Piezoelectric identification device and applications thereof” U.S. Patent 09/815,250, May 09, 2002.

[66] H. Y. Tang et al., "11.2 3D ultrasonic fingerprint sensor-on-a-chip," 2016 IEEE International Solid-State Circuits Conference (ISSCC), San Francisco, CA, 2016, pp. 202-203.

[67] M. F. Ashby, “Material Profiles” in Materials and the Environment: Eco-informed Material Choice, 2nd ed. Waltham, MA: Butterworth-Heinemann, 2013, ch. 15, pp. 459-590.

[68] Alexandre da Silva Scari, Bruno Cesar Pockszevnicki, Jánes Landre Junior, and Pedro Americo Almeida Magalhaes Junior, “Stress-Strain Compression of AA6082-T6 Aluminum Alloy at Room Temperature,” *Journal of Structures*, vol. 2014, no. 387680, pp. 1-7, 2014.

[69] D. S. Gardner and P. A. Flinn, “Mechanical Stress as a Function of Temperature in Aluminum Films”, *IEEE Transactions on Electron Devices*, Vol. 35, No. 12. pp. 2160-2169, 1988.

[70] P. R. Scheeper et al. “A New Measurement Microphone Based on MEMS Technology”, *J. Micromech. Syst.*, vol. 12, no. 6, 2003.

[71] "FMM Inc. > products > electronic substrate & thermal sink materials > aluminum Nitride," 2010. [Online]. Available: http://www.fmmceramics.com/aluminum_nitride.html. Accessed: Sep. 1, 2016.

[72] Volker Kempe, “Acclerometers” in *Inertial MEMS: Principles and Practice*, Cambrige, NY: Cambridge University Press, 2011, pp. 283-358.

[73] L. M. Roylance and J. B. Angell, "A batch-fabricated silicon accelerometer," in IEEE Transactions on Electron Devices, vol. 26, no. 12, pp. 1911-1917, Dec 1979.

[74] F. Rudolf et al., “Precision Accelerometer with μg Resolution” Sensors and Actuators, A21-A23, pp. 297-302, 1990.

[75] K. Jono, M. Hashimoto and M. Esashi, "Electrostatic servo system for multi-axis accelerometers," Micro Electro Mechanical Systems, 1994, MEMS '94, Proceedings, IEEE Workshop on, Oiso, 1994, pp. 251-256.

[76] Patrick Scheeper et al. 1996 J. Micromech. Microeng. 6 131

[77] Nemirovsky, Y., et al. "Design of novel thin-film piezoelectric accelerometer." Sensors and Actuators A: Physical, vol. 56, no. 3, pp. 239-249, 1996.

[78] De Reus, Roger, and Patrick R. Scheeper. "Fabrication and characterization of a piezoelectric accelerometer." Journal of Micromechanics and Microengineering 9, no. 2 (1999): 123.

[79] Beeby et al. “Microprocessor implemented self-validation of thick-film PZT/Silicon accelerometer”, 2001.

[80] DeVoe, D.L.; Pisano, A.P., "Surface micromachined piezoelectric accelerometers (PiXLs)," in Microelectromechanical Systems, Journal of, vol.10, no.2, pp.180-186, Jun 2001. doi: 10.1109/84.925733

[81] Li-Peng Wang; Wolf, R.A., Jr.; Yu Wang; Deng, K.K.; Zou, L.; Davis, R.J.; Trolier-McKinstry, Susan, "Design, fabrication, and measurement of high-sensitivity piezoelectric microelectromechanical systems accelerometers," *J. Microelectromechanical Systems*, vol.12, no.4, pp.433-439, Aug. 2003.

[82] Wang, Qing-Ming, Zhaochun Yang, Fang Li, and Patrick Smolinski. "Analysis of thin film piezoelectric microaccelerometer using analytical and finite element modeling." Sensors and Actuators A: Physical, vol. 113, no. 1, pp. 1-11, 2004.

[83] Qiang Zou; Wei Tan; Eun Sok Kim; Loeb, G.E., "Highly symmetric tri-axis piezoelectric bimorph accelerometer," in Micro Electro Mechanical Systems, 2004. 17th IEEE International Conference on. (MEMS) , vol., no., pp.197-200, 2004 doi: 10.1109/MEMS.2004.1290556

[84] F. Gerfers, M. Kohlstadt, H. Bar, M. -Y He, Y. Manoli, L. –P. Wang, "Sub-μg Ultra-Low-Noise MEMS Accelerometers Based on CMOS-Compatible Piezoelectric AlN Thin Films," in Solid-State Sensors, Actuators and Microsystems Conference, 2007. TRANSDUCERS 2007. International , vol., no., pp.1191-1194, 10-14 June 2007

[85] Kobayashi, T.; Okada, H.; Akiyama, M.; Maeda, R.; Itoh, T., "A digital output piezoelectric accelerometer using CMOS-compatible AlN thin film," in Solid-State

Sensors, Actuators and Microsystems Conference, 2009. TRANSDUCERS 2009. International , vol., no., pp.1166-1169, 21-25 June 2009.

[86] Kobayashi, T.; Okada, H.; Masuda, T.; Itoh, T., "A Digital Output Piezoelectric Accelerometer using Pattenrned Pb(Zr, Ti)O3 Thin Films Electrically Connected in Series," in Micro Electro Mechanical Systems, 2009. MEMS 2009. IEEE 22nd International Conference on , vol., no., pp.801-804, 25-29 Jan. 2009.

[87] Hindrichsen, C.C.; Almind, N.S.; Brodersen, S.H.; Hansen, O.; Thomsen, E.V., "Analytical Model of a PZT Thick-Film Triaxial Accelerometer for Optimum Design," in Sensors Journal, IEEE , vol.9, no.4, pp.419-429, April 2009.

[88] Hindrichsen, C.C.; Larsen, J.; Thomsen, E.V.; Hansen, K.; Lou-Moller, R., "Circular piezoelectric accelerometer for high band width application," in Sensors, 2009 IEEE , vol., no., pp.475-478, 25-28 Oct. 2009.

[89] Hrairi, Meftah, and Badrul Hanafi Bin Baharom. "Design and modelling of silicon MEMS accelerometer." International Journal of Engineering Systems Modelling and Simulation 5.4 (2013): 181-187.

[90] Shanmugavel, S.; Kui Yao; Trung Dung Luong; Oh, S.R.; Yifan Chen; Chin Yaw Tan; Gaunekar, A.; Ng, P.H.Y.; Li, M.H.L., "Miniaturized acceleration sensors with in-plane polarized piezoelectric thin films produced by micromachining," IEEE Transactions on Ultrasonics, Ferroelectrics, and Frequency Control, vol.58, no.11, pp.2289-2296, November 2011.

[91] Hewa-Kasakarage, N.N.; Donghwan Kim; Kuntzman, M.L.; Hall, N.A., "Micromachined Piezoelectric Accelerometers via Epitaxial Silicon Cantilevers and Bulk Silicon Proof Masses," J. Microelectromechanical Systems, vol.22, no.6, pp.1438-1446, Dec. 2013

[92] Saayujya, C., Tan, J. S. Q., Yuan, Y., Wong, Y. R., & Du, H. (2014, April). Design, fabrication and characterization of a zinc oxide thin-film piezoelectric accelerometer. 2014 IEEE Ninth International Conference on Intelligent Sensors, Sensor Networks and Information Processing (ISSNIP), pp. 1-6, 2014.

[93] R. D. Conner, R. B. Dandliker, and W. L. Johnson. "Mechanical properties of tungsten and steel fiber reinforced Zr 41.25 Ti 13.75 Cu 12.5 Ni 10 Be 22.5 metallic glass matrix composites." *Acta Materialia*, vol. 46, no. 17, pp. 6089-6102, 1998.

[94] T. B. Gabrielson, "Mechanical-thermal noise in micromachined acoustic and vibration sensors," IEEE Trans. On Electron Devices (40), pp. 903-909, 1993.

[95] I. S. Gönenli, Z. Celik-Butler, and D. P. Butler, "MEMS Accelerometers on Polyimide Substrates," IEEE Sensors Journal, vol. 11, pp. 2318-2326, 2011.

[96] M. Bao, "Analysis and Design Principles of MEMS Devices", 1 st ed.,vol. 2. Elsevier: Clarendon, 2005, pp. 115-174.

[97] M. Bao and H. Yang, "Squeeze Film Air Damping in MEMS", *Sensors and Actuators A*, vol. 136, pp. 3-27, 2007.

Biographical Information

Md Sajeeb Rayhan received his B. Sc. degree in electrical, electronic and communication engineering (EECE) from Military Institute of Science and Technology (MIST), Dhaka, Bangladesh, in 2009. He served as an instructor in Atish Dipankar University of Science and Technology (ADUST), Dhaka, Bangladesh between June 2010 and June 2011. He started his direct BS to Ph. D. degree in electrical engineering (EE) in University of Texas at Arlington, TX, USA, in Fall 2011.

Since Fall 2011, he has been working in Microsensors Laboratory and the Nanotechnology Research Center, UTA. His research interests include design, fabrication and characterization of MEMS sensors using ultrathin and flexible aluminum nitride (AlN) films. He has authored three conference papers so far in this area as a first author. Several conference and journal papers are under preparation. He has been also serving as a teaching assistant in electrical engineering (EE) department in UT Arlington since 2011.

Md Sajeeb Rayhan is a member of IEEE, Tau Beta Pi and Eta Kappa Nu. He was awarded with 'MIST Dean list' and 'MIST Commandant list' awards for his outstanding academic achievements in 2008 and 2009, respectively. He has been awarded 'Enhance Graduate Teaching Assistantship (EGTA)' in Fall 2011-Spring 2016, 'Doctoral Teaching Fellowship' in Fall 2011-Spring 2016, and Doctoral Dissertation Fellowship in Summer 2016 from UT Arlington.